Classical and non-classical nucleation pathways of strontium sulfate : A study in bulk and confined environments

Andrew Robert Lauer

THÈSE

Pour obtenir le grade de

DOCTEUR DE L'UNIVERSITÉ GRENOBLE ALPES

École doctorale : STEP - Sciences de la Terre de l'Environnement et des Planètes
Spécialité : Sciences de la Terre et de l'Environnement
Unité de recherche : Institut des Sciences de la Terre

Voies de nucléation classiques et non-classiques du sulfate de strontium : étude en milieux confinés et non-confinés

Classical and non-classical nucleation pathways of strontium sulfate: A study in bulk and confined environments

Présentée par :

Andrew Robert LAUER

Direction de thèse :

Roland HELLMANN DIRECTEUR DE RECHERCHE, Université Grenoble Alpes	Directeur de thèse
Alejandro FERNANDEZ-MARTINEZ CHARGE DE RECHERCHE, Université Grenoble Alpes	Co-directeur de thèse
Alexander VAN DRIESSCHE CHARGE DE RECHERCHE, CNRS	Co-directeur de thèse

Rapporteurs :

Diane REBISCOUL
DIRECTRICE DE RECHERCHE, CEA centre de Marcoule
Stephane VEESLER
DIRECTEUR DE RECHERCHE, CNRS délégation Provence et Corse

Thèse soutenue publiquement le **19 mars 2024**, devant le jury composé de :

Laurent TRUCHE, PROFESSEUR DES UNIVERSITES, Université Grenoble Alpes	Président
Roland HELLMANN, DIRECTEUR DE RECHERCHE, CNRS délégation Alpes	Directeur de thèse
Diane REBISCOUL, DIRECTRICE DE RECHERCHE, CEA centre de Marcoule	Rapporteure
Stephane VEESLER, DIRECTEUR DE RECHERCHE, CNRS délégation Provence et Corse	Rapporteur
Tomasz STAWSKI, SENIOR SCIENTIST, Bundesanstalt für Materialforschung	Examinateur

Invités :

Alexander E. S. VAN DRIESSCHE
SCIENTIST, Instituto andaluz de Ciencias de la Tierra
Alejandro FERNANDEZ-MARTINEZ
CHARGE DE RECHERCHE, CNRS

Abstract

Classically, solid nucleation is considered to be a stochastic process in which clusters of monomers randomly come together into solid a solid nucleus due to agitation or Brownian motion within a supercritical fluid. However, modern observations shed new light on alternative pathways via which nucleation reactions can occur, specifically via multi-step mechanisms with nano-scale intermediate species. Here, we explore the nucleation of strontium sulfate from aqueous solution within the framework of various nucleation theories. First, we propose the presence of an intermediate participating in the nucleation of celestine, and the concentration-dependent appearance of this non-classical nucleation pathway is discussed in terms of mesoscale nucleation theory. We also examine strontium sulfate hemihydrate, a relatively little-known transient phase that precedes the thermodynamically stable celestine under certain conditions. *In situ* raman and XRD reveal that this phase is an independent mineral phase that, when present, dissolves before the nucleation of the stable celestine. The differences in the observed nucleation pathway of this hydrated phase and that of celestine reveals a possible mechanism for phase and polymorph selection during nucleation reactions. Finally, the influence of nanoconfinement on nucleation reactions in the Sr-SO_4-H_2O system is explored, providing further evidence for the existence of a nucleation intermediate and demonstrating the potential of counterdiffusion in porous media as a method to explore the fundamental nature of nucleation itself.

Résumé

Classiquement, la nucléation solide est considérée comme un processus stochastique dans lequel des groupes de monomères se rassemblent au hasard pour former un noyau solide sous l'effet de l'agitation ou du mouvement brownien au sein d'un fluide supercritique. Cependant, les observations modernes mettent en lumière d'autres voies par lesquelles les réactions de nucléation peuvent se produire, en particulier par le biais de mécanismes à plusieurs étapes avec des espèces intermédiaires à l'échelle nanométrique. Ici, nous explorons la nucléation du sulfate de strontium à partir d'une solution aqueuse dans le cadre de différentes théories de nucléation. Tout d'abord, nous proposons la présence d'un intermédiaire participant à la nucléation de la célestine, et l'apparition en fonction de la concentration de cette voie de nucléation non classique est discutée en termes de théorie de la nucléation à méso-échelle. Nous examinons également le sulfate de strontium hémihydraté, une phase transitoire relativement peu connue qui précède la célestine thermodynamiquement stable dans certaines conditions. Le raman in situ et la XRD révèlent que cette phase est une phase minérale indépendante qui, lorsqu'elle est présente, se dissout avant la nucléation de la célestine stable. Les différences observées entre la voie de nucléation de cette phase hydratée et celle de la célestine révèlent un mécanisme possible de sélection des phases et des polymorphes au cours des réactions de nucléation. Enfin, l'influence du nanoconfinement sur les réactions de nucléation dans le système Sr-SO4-H2O est explorée, fournissant des preuves supplémentaires de l'existence d'un intermédiaire de nucléation et démontrant le potentiel de la contre-diffusion dans les milieux poreux comme méthode d'exploration de la nature fondamentale de la nucléation elle-même.

Table of Contents

Motivation

The flow of water is a major driver of geologic phenomenon on the surface of the earth. However, a nearly equally important part of the equation lies hidden just out of sight below the surface. Within the cracks, fissures, and pores water is flowing, and understanding that flow is critical for developing a full picture of what is happening within the earth's crust[1]. This understanding is made significantly more difficult due to phase changes that are constantly changing the very nature and structure of the pore space.

Phase changes, wherein matter transitions from one state to another, are among the most ubiquitous and fundamental mechanisms for manipulating matter, both in natural occurrences and engineering applications. These changes always represent the transformation of matter from a state of relatively high energy to a lower energetic state. However, they often involve an energetic barrier that must be overcome to attain the low-energy state. The process of traversing this energetic barrier typically occurs via the process of nucleation, a phenomenon in which local fluctuations create microstates that can be pushed over the energy barrier, forming a nucleus (microscopic cluster or particle of the new phase).

Explorations into the nucleation process can be traced back to the 1700's with Farenheit's discovery of the phenomenon of supercooling (which is now understood to be the first observation of the aforementioned energetic barrier)[2]. However, it is more frequently considered to have emerged in the late 1800's with Gibbs' formalization of free energy and the concept that systems are driven towards lower energy states[3]. The theoretical formulations of Volmer and Weber in the early 20th century[4], along with continued refinements of these ideas until the mid-century, led to the development of what is today known as classical nucleation theory (CNT). While the original derivations from Volmer and Weber described the condensation of water from vapor, the theory has since been expanded to cover a multitude of types of phase changes.

For the case of mineral precipitation from solution, CNT describes a single-step process in which small clusters of ions are randomly formed and have energies determined by the balance of interfacial tension between the old and new phase, and the bulk stability of the precipitate. The solid line in the figure below describes this free energy landscape, the maxima of which represents the critical size at which a cluster

of ions becomes a nucleus, and can begin to grow into a bulk crystal (strictly speaking a cluster at the top of the energy barrier has the same probability to grow or dissolve).

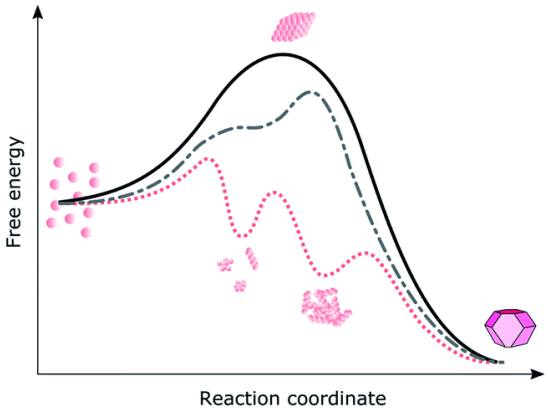

The kinetic equations derived from CNT formulations have proven useful for describing the rate behavior of a wide variety of nucleation phenomena. However, mechanistically, it is severely limited by the requirement that the first nucleus should have the same microstructural form as the final bulk crystal and the same thermodynamic properties (the capillary assumption), it's single-parameter (particle size) nature, and that it fails to describe the existence of intermediate species that have been observed in modern nucleation research. To address these limitations and rationalize observed intermediates within a CNT-like framework, the concept of local thermodynamic minima which can act as 'stopping points' along the nucleation pathway was proposed (pink dotted line). Each transformation step is then subject to a new energy barrier that is overcome via a stochastic fluctuation. This so-called non-classical nucleation model is the subject of intensive work defining the precise nature of the intermediates, when they appear, how they transform, and whether any of these details can be generalized into a universal description of 'non-classical' nucleation.

Against this backdrop, an emerging idea challenges the notion that the existence of a thermodynamic minimum is a necessary condition for the observation of nucleation intermediates. The Mesoscopic Nucleation Theory (MeNT) expands the parameter space through which nucleation can be analyzed. Increasing the parameters available for describing the system before nucleation results in a complex free-energy landscape (grey dashed-and-dotted line). MeNT allows for the observation of 'particles' that are not thermodynamically stable, but instead can be observed by their relatively low rate of transformation.

The core of this work explores these theories of nucleation through the observation of strontium sulfate nucleation. Along the way, the physicochemical parameters that control $SrSO_4$ precipitation are examined, with a particular focus on how confinement (restricting the reaction to nano-scale spaces) changes the nucleation process. The effects of confinement have been explored under the umbrella of CNT through the description of pore-controlled solubility (PCS) kinetics, and observations of biomineralization have revealed that porosity can influence phase selection during the nucleation process, making confinement a potential driver of the nucleation pathway shape. These effects, as well as the potential of confinement as a vehicle for the study of nucleation itself, are investigated in this work.

This dissertation is divided into three chapters, which describe the experimental work, analysis and discussion of the obtained results. A detailed review of the state-of-the-art is provided with each chapter. At the end of this dissertation, a general summary and outlook is provided.

References

1. B. W. D. Yardley and K. I. Shmulovich, in *Fluids in the Crust*, Springer Netherlands, 1994, pp. 1–12.
2. D. G. Fahrenheit, *Philos. Trans. R. Soc. London*, 1724, **33**, 1–3.
3. *The Collected Works of J. Willard Gibbs. Vol. 1: Thermodynamics. Pp. xxviii + 434*
4. M. Volmer and A. Weber, *Zeitschrift für Phys. Chemie*.

Chapter 1

Multistep nucleation compatible with a single energy barrier: catching the non-classical culprit

A. R. Lauer[1], M. A. Durán-Olivencia[2,3,4], A. Fernandez-Martinez[1] and A. E. S. Van Driessche[1,5]

[1] Université Grenoble Alpes, Université Savoie Mont Blanc, CNRS, IRD, IFSTTAR, ISTerre, 38000 Grenoble, France
[2] Department of Computer Science, Universidad Pontificia Comillas, C/Alberto Aguilera 25, Madrid, 28015,
[3] Institute for Research in Technology (IIT), ICAI School of Engineering, Universidad Pontificia Comillas, C/Santa Cruz de Marcenado 26, Madrid, 28015, Spain
[4]Department of Chemical Engineering, Imperial College London, London, UK
[5] Instituto Andaluz de Ciencias de la Tierra, IACT, CSIC – University of Granada, Granada, Spain.

Abstract

In this chapter we link experimental results of SrSO4 precipitation with a nucleation model based on mesoscopic nucleation theory (MeNT) to stride towards a cohesive view of the nucleation process that integrates both classical and non-classical views. When SrCl2 and Na2SO4 are co-titrated at slow dosing rates, time-resolved turbidity, conductivity and ion-specific data reveal that the initial stage of the nucleation process is driven by neutral species, i.e. ion-pairs or larger, akin to the prenucleation cluster model. However, when co-titrations are conducted at higher rates, the onset of nucleation is dominated by the consumption of free ions, akin to the explanation provided by classical nucleation theory (CNT). The occurrence of both mechanisms for the same system is explained by a toy model that includes both the thermodynamics (consisting of a single energy barrier) and kinetics of cluster formation formally obtained from MeNT. This gives rise to an effective energy barrier exhibiting a local intermediate minimum, which does not originate from a minimum in the thermodynamic free energy. Rather, it is associated with an increased probability of observing a specific class (in terms of size/density) of precursor clusters due to their slower kinetics. At high supersaturations this minimum in the kinetics of cluster formation becomes less pronounced and the effective barrier is also significantly lowered. Consequently, the probability of observing an intermediate state is blurred and we recover a nucleation pathway more closely following the one envisaged by the classical model. Thus, our model is capable of capturing both single and multistep nucleation mechanisms observed experimentally considering only a single energy barrier.

1. Introduction

Nucleation is an activated process in which a system overcomes a free energy barrier during the first-order phase transition from a metastable to a stable phase. In the particular case of crystallization from solution, it is commonly accepted that the nucleation process starts by random aggregation of ions/species in solution, which form clusters that eventually may evolve into a crystal. When accounting for the contributions of bulk (favorable) and surface (unfavorable) interactions as the randomly formed aggregates grow in size, the overall free energy of a nucleating system first increases, thus posing a barrier. Consequently, many of the initially formed clusters will quickly re-dissolve and only a few, as a result of statistical fluctuations, reach a certain critical size (where they become an actual nucleus), at which the gain in volume free energy equals the costs of surface free energy (maximum in DG). Any further addition of ions/species will lead to a decrease in overall energy of the nucleus, which will continue to grow to a mature crystal. According to classical nucleation theory (CNT)[1], the formation of a nucleus is a one-step process that produces a microscopic particle with the same characteristics (e.g. order, density, composition, etc.) as a fully-grown macroscopic crystal. In CNT, this transition from dissolved ions/species to crystalline entities is associated with a single energy barrier (black curve, Figure 1).

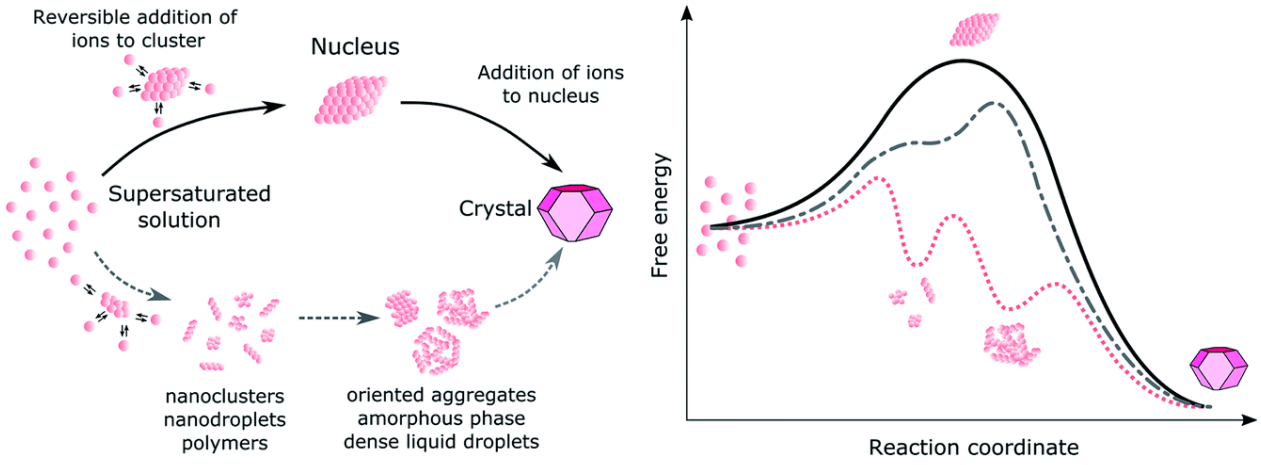

Figure 1: *Schematic representation of one- and multi-step mechanisms for the formation of crystals from supersaturated solutions and their associated energy barriers: a single barrier representative of classical nucleation (black curve), a multi-step barrier model proposed for non-classical nucleation (dotted pink curve) and a multislope single barrier considered by MeNT (grey curve).*

However, experimental results gathered during the last decades have challenged this classical picture by revealing that the route from a supersaturated solution to a solid (crystalline) material can involve multiple steps in which distinct

precursors and/or intermediate phases occur and interconvert across different length and time scales[2,3]. It is generally assumed that such a multi-step (or so-called non-classical) pathway also implies a multi-barrier energetic landscape for nucleation[4–6] (pink curve, Fig. 1). For example, some of the precursors/intermediates correspond to local free energy minima separated by individual barriers that need to be overcome for the system to transform (note that each transformation step can involve a new nucleation event, either in the condensed phase – structural reorganization – or in solution after re-dissolution). Nonetheless, recent theoretical considerations within the context of the Mesoscopic Nucleation Theory (MeNT)[7] postulate that energy minima are not a prerequisite for multi-step nucleation to occur, since precursor species could potentially emerge due to the competition between thermodynamics and kinetics during cluster formation on a continuous uphill energy profile[8,9] (grey curve, Figure 1).

In this work we attempt to link experimental results of $SrSO_4$ precipitation with MeNT modeling to stride towards a cohesive view of the nucleation process. When $SrCl_2$ and Na_2SO_4 are co-titrated at slow dosing rates, nucleation occurs at relatively low supersaturations and time-resolved turbidity, conductivity and ion-specific data reveal that the initial phase separation is controlled by neutral species, i.e. ion-pairs or larger, akin to the pre-nucleation pathway[10]. When co-titrations are conducted at higher rates, nucleation occurs at considerably higher supersaturations and the data obtained from the different probes show that the initially nucleating phase is formed mainly through the consumption of free ions, akin to the CNT model. The occurrence of both nucleation mechanisms for the same system is also observed when using a toy model to describe the nucleation pathway, consisting of a single energy barrier and kinetics of cluster formation inspired by the ones formally obtained from MeNT. The potential implications of these preliminary findings and future endeavors are discussed.

2. The MeNT-based toy model

The classical nucleation theory (CNT) presents a series of inherent problems, such as the lack of consistency when expressing measurable quantities, such as the nucleation rate, as a function of one order parameter, e.g. the cluster molecular size N or the cluster radius R[1,11,12]. In addition, CNT entails other constraints that further limit its range of applicability. It assumes a spherically symmetric nucleation cluster, with an associated work of formation determined by the equilibrium thermodynamic potential

(free energy in the case of closed systems, or Landau's potential in the case of open systems). Also, it imposes a very naive nucleation pathway that fixes the structural properties of the clusters to be the same as the ones of the final stable bulk phase. This nucleation pathway can be represented as a straight line in the parameter space, connecting two points: zero and infinity. Nevertheless, it is reasonable to expect that clusters are not only characterized by their size, but by several other features (e.g. density/order). Thus, the assumption of clusters growing or shrinking along the cluster-size (R or N) axis with all their other properties being exactly the same as the macroscopic phase is in many cases an oversimplification of reality.

Indeed, the constraints of the CNT model come at a great cost. For example, it cannot account for the rich family of clusters that have been observed experimentally during the nucleation process of a variety of systems[2,3,10]. Of the main CNT constraints we have just pinpointed, the spherical symmetry and the local-equilibrium approximation do not affect the internal properties of nucleation clusters. These two assumptions are usually invoked to facilitate the mathematical expressions involved, and allow the formulation of an analytical theory in terms of manageable equations. As for the remaining constraint, the imposed nucleation pathway cancels out all clusters that are not perfect microscopic replicas of the final phase. For instance, according to CNT, if the final stable phase is a crystal then clusters must have the very same structure as the equilibrium configuration.

To overcome these inherent limitations of CNT, the description of the nucleation process used in this work relies upon a fluctuating-hydrodynamical picture of out-of-equilibrium systems, also known as MeNT[7]. MeNT starts from an atomistic description of out-of-equilibrium fluids, and finally recovers CNT-like expressions[11,13,14]. To reduce the number of independent variables of the MeNT theory and obtain an explicit solution of fundamental quantities, such as the nucleation rate or the cluster distribution function, a general framework for nucleation (GFN)[8] has been derived within the context of MeNT establishing the nucleation pathway as the core of the process. This led to a single-variable theory to describe nucleation. Thus, if we have a model for the nucleation pathway GFN will provide us with an exact expression of the cluster distribution, which can then be contrasted against experimental observations.

The key components of the nucleation model used in this work are the following:

(I) A parametric description of the density fluctuations (clusters), $\rho(\boldsymbol{r};t)$, in terms of measurable properties, such as cluster radius, inner density, order, etc. In order to get tractable analytical equations, clusters are assumed to be spherically symmetric, so that $\rho(\boldsymbol{r};t)=\rho(r;t)$. The parametric description of clusters is then accomplished by introducing a parameterisation in terms of those variables:

$$\rho(r;t)=\rho(r;x_1(t),x_2(t),\dots,x_N(t))$$

Where $x_1(t),x_2(t),\dots,x_N(t)$ are the so-called order parameters (or reaction coordinates). CNT is recovered by setting $x_1(t)=R(t)$, with *R* being the cluster radius and maintaining all other properties constant and equal to the values of the final equilibrium phase. A more general CNT is reached by setting: $\rho(r;t)=\rho\big(x_1=R(t),x_2=\rho_0(t)\big)$, with ρ_0 being the average inner density of the cluster, assumed constant inside the cluster, now free to change unlike CNT. For the sake of brevity, we will drop the time-dependency of the order parameters, by simply referring to them as $x_1,x_2,\dots,x_N$, bearing in mind the underlying dependency. In this study we will consider a two-variable description of clusters, although more order parameters could be added if needed. However, it has been shown that a two-variable description is good enough to capture the most important aspects of nonclassical nucleation pathways whilst keeping in the theory analytically tractable[8,13].

(II) A model of the free energy functional $\Omega[\rho]=\Omega(x_1,x_2,\dots,x_N)$, which determines the equilibrium states of the system. For this we will use a standard fluid equation of state, based on thermodynamic perturbation theory[15,16]. Once we have a model for the free energy of the system we will be able to build the nucleation barrier by differentiating the energy in the presence of a cluster, $\Omega[\rho]$, and the energy of the system in the absence of any cluster, $\Omega[\rho_\infty]$, where $\rho_\infty=\lim_{r\to\infty}\rho(r;t)$, which refers to the average density of the metastable phase. This has been shown to yield a prototypical volume-*vs.*-surface barrier[13].

(III) A nucleation pathway, Γ, which represents a trajectory in the parameter space (i.e., the space where the coordinate axes are the order-parameter variables mentioned above). As any trajectory in a geometric space, the pathway can be rewritten in terms of the natural arc-length parameter, *s*, or by any other variable

which is one-to-one related to s. The average inner density of the cluster, ρ_0, is in a one-to-one relationship with *s*, as was shown elsewhere[7,8]. This is quite convenient given that ρ_0 is experimentally accessible, unlike the arc-length of the nucleation pathway. Hence, from here on we will not differentiate between *s* and ρ_0.

Now, based on the nucleation trajectory Γ where the clusters will be fluctuating over, and the cluster-density parameterization, steady-state and equilibrium cluster distributions (i.e. the probability density functions to find a cluster at any point of the nucleation pathway, with the properties determined by the value of s) can be derived[8]:

$$P_{st}(s) = A_{st}\sqrt{g(s)}e^{-\beta\Omega(s)}\int_{s}^{s_+} dz\sqrt{g(z)}e^{-\beta\Omega(z)}$$

$$P_{eq(s)} = A_{eq}g^{\frac{1}{2}}(s)e^{-\beta\Omega(s)} = A_{eq}\exp\left(-\beta\Omega(s) + \frac{1}{2}\log g(s)\right)$$

Where A_{st} and A_{eq} are normalisation constants, g(s) is the so-called metric function which recovers the monomer attachment rate in the case of a single parameter $x_1 = R, \beta = 1/k_BT$ is the reciprocal temperature, and $s_+ = (1+\varepsilon)s^*$ is a boundary point in the vicinity of the critical cluster s* separating the nucleation and growth stages, with $\varepsilon < 1$. The steady-state and equilibrium distributions of the clusters are nearly identical within the pre-critical region of the parameter space, as was shown recently[8]. For this reason, we focus our attention on the equilibrium distribution, as it is more straightforward and contains all the elements necessary to study a nucleation process.

The metric function g(s) represents the kinetics of cluster formation, given that it recovers the monomer attachment rate from CNT when a single order-parameter description of the cluster is adopted[11]. This is worth mentioning because, if we have a careful look at the equilibrium cluster distribution (Equation 3), the kinetics can be embedded in an effective energy barrier that allows us to rewrite P_{eq} as a standard Arrhenius-like equation.

$$P_{eq}(s) = A_{eq}\exp\left(-\beta\Omega_{eff}(s)\right)$$

With

$$\beta\Omega_{eff}(s) = \beta\Omega(s) - \frac{1}{2}\log g(s)$$

This is the essential part of the model, because it allows studying the properties of the cluster distribution by merely observing the behavior of the effective energy barrier $\beta\Omega_{eff}(s)$. The outcome of this approach is described in detail in the Results section.

3. Materials and Methods

3.1 cotitration experiments

Stock solutions of $SrCl_2$ and Na_2SO_4 were prepared by dissolving $SrCl_2 \cdot 6H_2O$ (Acros organics, 99% extra pure) and Na_2SO_4 (Carl Roth, ≥99% pure) in deionized water. Using both stock solutions, equimolar potentiometric co-titrations were conducted using a Metrohm 905 Titrando equipped with two 800 Dosino devices both controlling a 20 mL dosing unit which has a minimum dosing speed of 0.015 mL min^{-1}. The titrants were added to 50 mL of deionized water in a 20–90 mL Titration Vessel purchased from Metrohm. A 20 × 6 mm Teflon-coated stir bar at 500 rpm agitated the reaction. The reaction was monitored simultaneously for transmittance (Metrohm optrode – part 6.115.000), conductivity (Metrohm 5-ring conductivity measuring cell c = 0.7 cm^{-1} with Pt1000 – part 6.0915.100), and cation concentration (Ion Selective Electrode (ISE) that consisted of two half-cells: a Mettler-Toledo DX337-Ba membrane with a Metrohm LL ISE reference electrode – part 6.0750.100).

ISE calibration was conducted to convert voltage readouts to actual free ion concentrations. These calibrations were carried out in two steps by titrating $SrCl_2$ (100 mM at 0.5 mL min^{-1}) and NaCl (200 mM at 0.5 mL min^{-1}) into deionized water. This allowed for the accounting of the effect of both cations on the measured potential. From each calibration curve, the Nernstian equation was fitted for the parameters U_0 and p (the sign of p has been changed from standard representation for clarity):

$$U = U_0 + p \log(c + c_0)$$

With c_0 assumed to be negligible. The fitting procedure first found the slope ofo $\log(c_{dosed})$ vs. U to fit for the parameter p. then the equation can be rearranged to find:

$$e^{U/p} = c e^{U_0/p}$$

And treating $e^{U_0/p}$ as a constant K, we obtain an easy expression for treating the data where:

$$c_{measured} = e^{U/p} / K$$

K was determined by plotting the concentration of dosed ions against the function $e^{U/p}$ using the *p* parameter defined in the first step. For each titration, this calibration procedure was conducted two times with strontium chloride and one time with sodium chloride. With a new ISE, the *s* parameter was found to be quite consistent (standard

deviation below 3%), so to determine the 1/*K* parameter for sodium, the average *p* for the strontium calibrations was used. Then the two 1/*K* parameters were summed, and applied to the experimental data alongside the s parameter obtained from the strontium calibration.

Table 1: *Dosing rates and the critical supersaturation index, SI_{crit}, at which nucleation is first detected. The error represents the standard deviation from three replicate experiments*

Dosing rate (mol min^{-1})	SI_{crit}	Error
0.002	1.15	0.08
0.010	1.33	0.04
0.100	1.63	0.01
0.500	1.91	0.01
1.000	2.02	0.02

Different dosing rates were used to vary the saturation rate across several orders of magnitude (Table 1). At the point of nucleation, we know the concentration of ions that has been dosed into the solution and from this the critical saturation index, SI_{crit}, relative to the solid phase (*i.e.* celestite) was calculated using Phreeqc[17] and the BRGM Thermoddem geochemical database[18]. As expected, SI_{crit} increased with increasing dosing rates (Table 1).

3.2 Nucleation point determination

During co-titration experiments, three probes, i.e. optrode, ion selective probe and conductivity probe, were used to monitor in situ the nucleation process. From these time-resolved data the onset of phase transition was determined by an automated analysis routine based on the changes in the behavior of the first derivative, i.e. the time point of nucleation was defined when the first derivative reached 5% of its minimum value. For optical transmittance, this was the point at which the derivative became non-zero. Both the conductivity and free cation concentration curves had a downward concavity that required a more complex algorithm to precisely define the time of nucleation observed by those probes. To this end, the curves were smoothed, derived, smoothed again, and then the slope before the nucleation point was fit with a line. Nucleation was defined as the point at which the first derivative deviated significantly (5%) from that fit line.

4. Results and Discussion

4.1 Co-titration experiments

In order to study the evolution of the ionic environment during the precipitation of strontium sulfate, equimolar co-titrations were conducted in which equal amounts of Sr^{2+} and SO_4^{2-} were added at a steady rate into a reaction vessel containing 50 mL of deionized water and continuously stirred to assure a homogeneous mixing. These titrations were monitored for cation activity, transmittance and conductivity (Fig. 2a). The first stage of these titrations is characterized by a monotone increase of cation activity and conductivity with a steady state transmittance signal. Upon nucleation, a second stage is reached in which transmittance drops sharply, while the conductivity signal starts to flatten out and the free ion curve experiences a drop. The point at which these changes occur is defined as the onset of nucleation and was determined by an automated analysis routine based on the behavior of the first derivative.

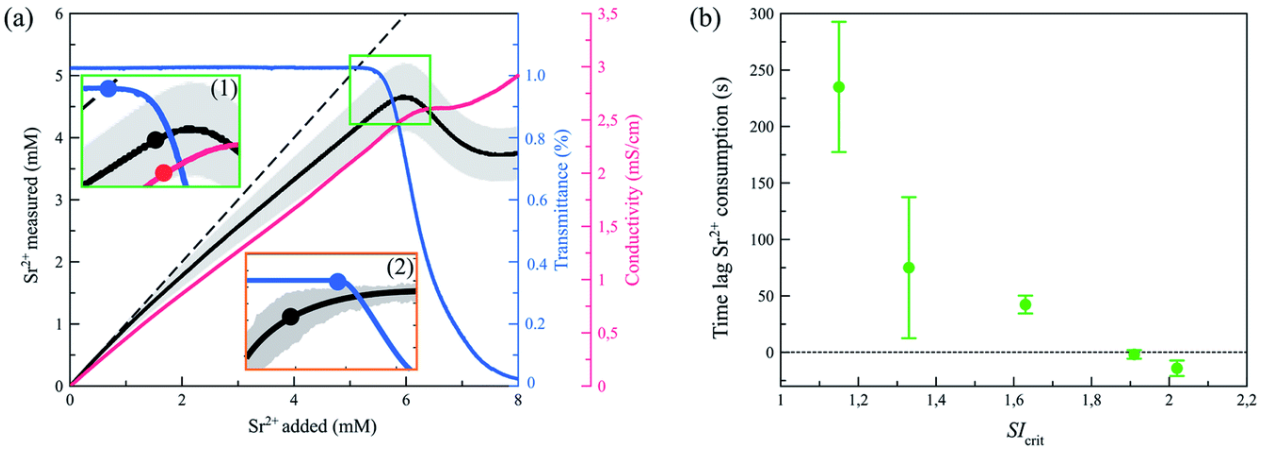

Figure 2: *$SrSO_4$ nucleation times monitored using co-titration experiments. (a) Example of an equimolar co-titration experiment at low dosing rate showing the time evolution of Sr^{2+} concentration (black), optical transmittance of the solution (blue), and the conductivity (red). For reference, the total added strontium concentration is shown (dashed line). Inset 1 (green square) shows an enlarged view of the nucleation event, which is defined as the point where transmittance begins to decrease or when the increases in Sr^{2+} concentration and conductivity slow. The nucleation points are indicated by large dots added to each curve. Inset 2 (orange square) shows a zoom in of the relevant area for the highest $SrSO_4$ dosing rate indicating that nucleation is detected first by the ISE. (b) Difference in measured nucleation time between the transmittance probe and the ISE as a function of the critical SI at which nucleation occurred. A positive difference means the optrode detected the phase transition before the ISE. Error bars represent the standard deviation of three replicate experiments.*

A close examination of Fig. 2a (see insets) shows that there is an apparent difference between the nucleation times measured by the transmittance probe and those measured by the ISE and conductivity. Using the previously described method to determine the nucleation time from the different data sets it is possible to compare

between the probes for experiments run with different dosing rates, from 0.002 to 1 mol min^{-1}. From these dosing rates and the known volume of the reaction solution volume the critical saturation index, SI_{crit}, at the nucleation time point can be calculated (Table 1).

At the three lowest dosing rates, and thus lowest SI_{crit}, the transmittance probe detected the formation of a new phase significantly before the ISE and conductivity probe registered the consumption of free ions (Fig. 2b). Importantly, this effect is most pronounced at the lowest dosing rate – where relatively low saturations would result in the lowest possible probe lags. This observation can be explained if we consider that the first step in strontium sulfate nucleation occurs via the consumption of neutral – *i.e.* bound – species that are not detected by the ISE. Indeed, Fig. 2a shows that the detected free Sr^{2+} is lower than the total added strontium, confirming the presence of bound ions that can be consumed to create this effect. Consequently, the particles detected by the optrode are formed through the aggregation of neutral particles, the smallest of which could be ion pairs. It is important to note here the error margin in the calibration of the ISE, which is represented by the grey shaded area surrounding the free ion curve in the main plot of Fig. 2a. This error represents the absolute maximum and minimum that the true reading for Sr^{2+} concentration could be considering 4 calibrations and two experiments, all conducted with a new ISE membrane on the same day (the error in the inset (2) comes from a different source – the standard deviation of three replicate experiments). While a significant portion of the shaded region coincides with the unity line (where free Sr^{2+} = dosed Sr), it is important to note that above the low concentration regime (<~2 mM Sr), the rate of change is less than one. In the low concentration regime, the results from this ISE are highly irreproducible and should not be considered as meaningful, and thus it is significant that the slope of the curve outside this regime indicates ion pairing or complexation even when considering the measurements least favorable to this hypothesis. Unfortunately, the inconsistency in the low concentration regime means we are unable to comment about the pairing and complexation of Sr^{2+} in this system below its saturation concentration (~0.7 mM under experimental conditions).

Now, we focus on the two highest dosing rates used for the co-titrations of $SrSO_4$. In these experiments, the early detection of nucleation by the transmittance probe vanishes and at the highest dosing rate (1.0 mol min^{-1}), the detection of

nucleation by transmittance even lags behind the potentiometric detection of nucleation (Fig. 2a, inset 2). An example of typical data from an experiment at this dosing rate is shown in Fig. 2a. Hence, at high dosing rates, i.e. high supersaturations, the first stage of nucleation is mainly driven by ion consumption and not by bound species. The fact that at the highest supersaturation the transmittance probe lags behind is probably due to the very small size of the initial nuclei, which go undetected at the used wavelength (660 nm). In short, the above-discussed experimental observations reveal that as the supersaturation rate, and thus also the critical supersaturation, increases during $SrSO_4$ co-titrations, the preferred nucleation mechanism changes.

4.2 The effective nucleation barrier: Thermodynamics meets kinetics

In this section we present the outcome of our theoretical modelling based on the equations of GFN[8] for the cluster distribution after adopting a model nucleation pathway inspired by the one obtained from a two-variable MeNT[13]. As we mentioned in Section 2, to obtain a nucleation barrier a model for the free-energy functional of the system is required. For this, we used a fluid equation of state (EOS) to build an energy barrier, $\Delta\Omega[r]$, based on the Barker–Henderson perturbation theory with the reference system given by the Carnahan–Starling EOS, which has been shown to be well-suited for the description of transitions from low-density to high-density states[7,8,11,13,14]. We used this model EOS to initially obtain the bulk densities at coexistence for a given temperature, i.e. $\rho_\infty^{(c)}$ for the low-density phase and $\rho_0^{(c)}$ for the high-density state at a given β. Once these values have been determined, we place our simulated system into a supersaturated initial metastable state by imposing a density of $\rho_\infty = s \times \rho_\infty^{(c)}$, with $S = \rho_\infty / \rho_\infty^{(c)}$. Regarding the model of the nucleation barrier, $\beta\Omega$, we consider the surface-*vs.*-volume barrier[1,7,11,13]:

$$\Delta\Omega(R, \rho_0) = V(R, \rho_0)\Delta\omega + S\big(R, \rho_0 - \rho_{infty}\big)^2\sigma$$

With $\Delta\omega = \omega(\rho_0) - \omega(\rho_\infty)$ being the negative increment in the system's pressure in the presence of a cluster of volume and surface, $V = \frac{4\pi}{3}R^3$ and $S = 4\pi R^2$ respectively; and σ a constant which defines bulk planar surface tension.

Now that we have established the bulk system at a given temperature and a given initial density, ρ_∞, we need to introduce a nucleation pathway so that we can

compute $\beta\Omega_{eff}(s)$ along such a trajectory. As mentioned above, our pathway is inspired by the one obtained from MeNT[13], which selects the most probable pathway by following the steepest-descent path over the energy landscape. The resulting pathway has a characteristic U-shape (Fig. 3) and can be divided into three stages[11]: (i) the first part consists of large-size-low-density fluctuations (bottom branch in Fig. 3), followed (ii) by a densification at an almost constant size (between R ¼ 1 and R ¼ 2) and finally, (iii) the growth stage of the clusters (top branch in Fig. 3). Here, we assume a similar U-shaped nucleation pathway.

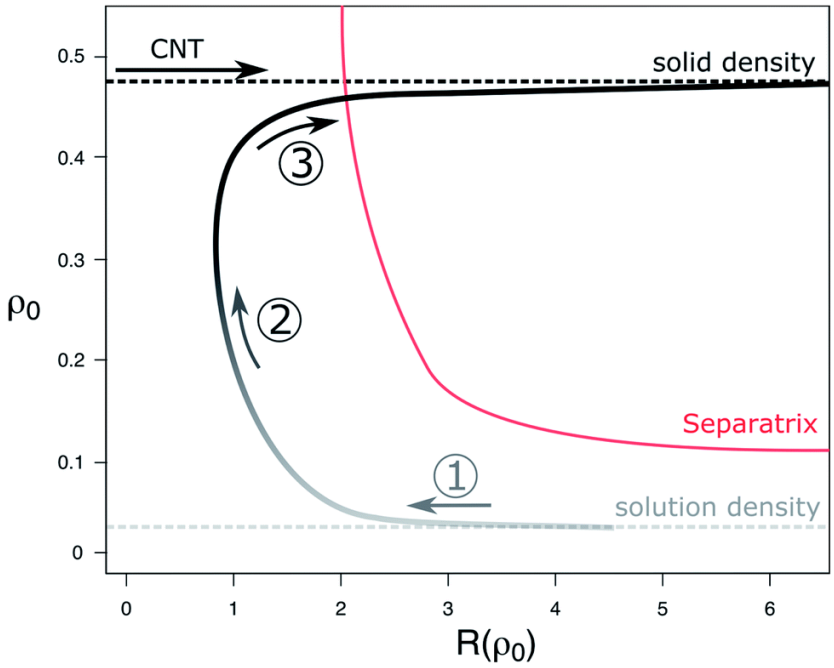

Figure 3: *Model nucleation pathways predicted by two-variable MeNT and CNT. Bottom and top dashed lines represent the initial and final stable-state densities, calculated using the EOS. To achieve nucleation, the separatrix must be crossed. The critical cluster for each pathway is the intersection between the pathway and the separatrix. The MeNT pathway shows three main stages:[13] (1) contraction of the large-size-low-density fluctuations (bottom branch); (2) densification at an almost constant size (between R = 1 and R = 2, left branch); and, finally, (3) the growth stage of the clusters (top branch). During this final stage, the MeNT is similar to the CNT pathway, where the interior density is comparable to that of the bulk solid phase and only the size, i.e. R, changes.*

Having established the nucleation pathway (Fig. 3), we now apply the equations previously discussed (Section 2), and study the effects of kinetics on the precritical cluster distribution. Fig. 4a shows the outcome of a computation of the thermodynamic energy barrier along the natural parameter $s{\sim}\rho_\infty$ for a set of ten supersaturation values, $S \in [1.75, 3.25]$, which results in a nucleation barrier of approximately 80 k_BT at 1.75 and that decreases with increasing supersaturation (red arrow Fig. 4a). In Fig. 4b the computed effective energy barriers for the same set of supersaturation values, $S \in [1.75, 3.25]$, are shown. Simultaneously, Fig. 5a shows how this translates into the

probabilities of observing a cluster of any given density between the values of the initial metastable and the final stable state.

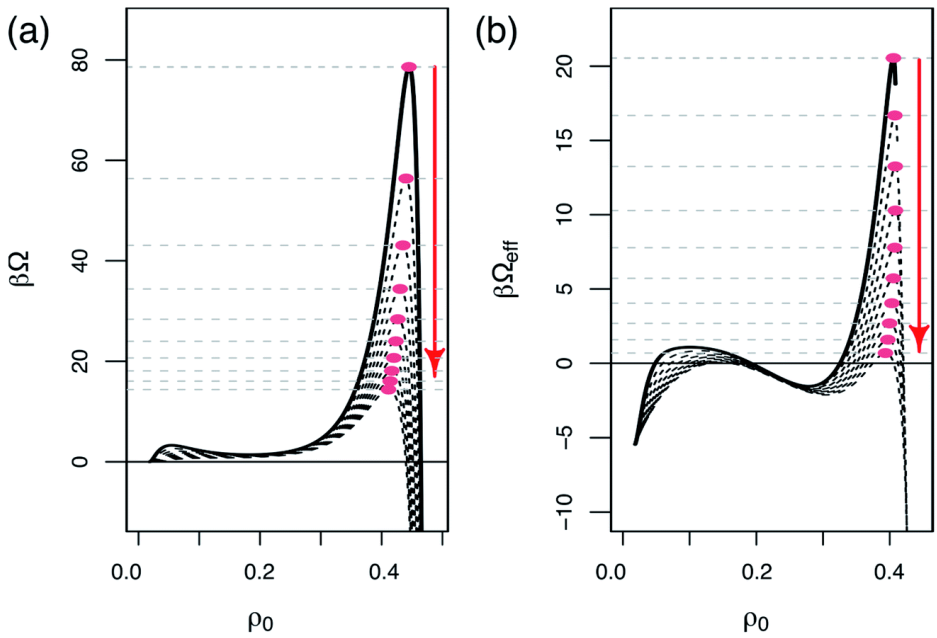

Figure 4: *Energy barrier (a) and effective energy barrier (b) for a range of supersaturation values S ∈ [1.75, 3.25]. Solid black line corresponds to S = 1.75, while all the other supersaturation values are represented as black-dashed lines. Red circles represent the critical clusters, and grey-dashed lines are drawn as a guide to the eye to highlight the nucleation barrier for each S value. Red arrows shows the direction of increasing S values.*

Remarkably, the effective energy barrier displays a minimum at an intermediate density between the mother phase and the critical-cluster density values. This has a direct impact on the cluster probability distribution (Fig. 5a), which, as we can observe, shows an intermediate local maximum of probability in pre-critical densities. Hence, the kinetic term does not affect all pre-critical clusters in the same way, since it induces a local minimum of the effective potential at an intermediate density, ρ_m, which is related to a maximum of probability. This tells us that such intermediate clusters will be observable before nucleation happens, therefore behaving as nucleation precursors.

Importantly, the local intermediate minimum observed in Fig. 4b does not come from a minimum of the thermodynamic free energy but emerges after taking into account the kinetics of cluster formation. This indicates that apparent multi-step energy barriers can be the result of the kinetics of cluster formation, while actually involving just a single energy barrier. But, Fig. 5a shows that with increasing supersaturation the likelihood of observing pre-critical clusters over a broad range of intermediate densities grows. This gradually decreases the importance of any specific region along the

density axis (say the vicinity of an intermediate density, ρ_m), since any pre-critical density becomes more and more accessible as the supersaturation increases. Consequently, a separation between a specific class of pre-nucleation clusters and the eventual nucleation event becomes less and less evident as the supersaturation value increases. Eventually, the effective energy barrier becomes of the order of thermal fluctuations so that all possible pre-critical densities, i.e. from monomers and onward, are all likely to be observed, making it harder to differentiate any specific class of precursor clusters.

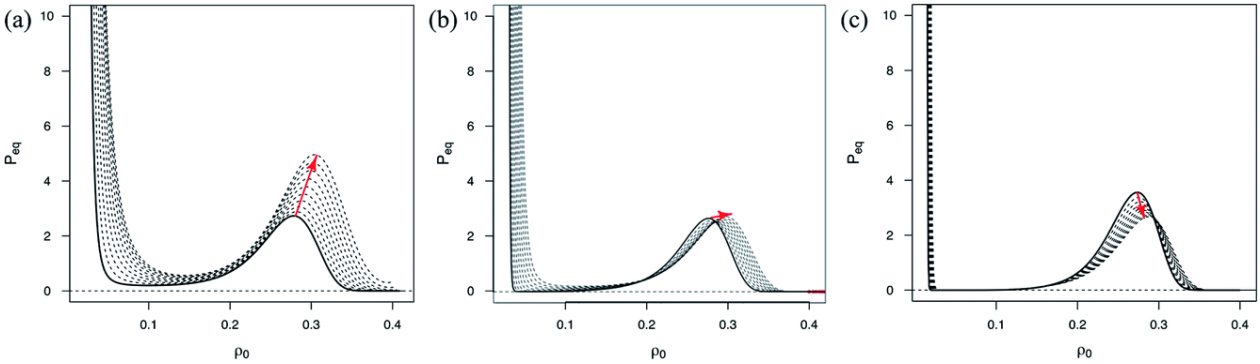

Figure 5: *Equilibrium probability distributions* $\left(P_{eq} \sim e^{-\beta \Omega_{eff}}\right)$ *of clusters associated with the supersaturation values S ∈ [1.75, 3.25] (a), S ∈ [1.01, 1.75] (b) and S ∈ [0.75, 1.0] (c). Solid black line corresponds to S = 1.75, S = 1.01 and S = 0.75, respectively. All the other supersaturation values are represented as black-dashed lines and the red arrow indicates increasing S values.*

Since a well-defined population of precursor clusters appears to be more evident as the supersaturation decreases we also studied a lower interval of supersaturation values $S \in [1.01, 1.75]$, which is shown in Fig. 5b. As can be observed, the results show that the emergence of precursor clusters is consistent even for very low supersaturations. Provided that the cluster-formation pathway remains unaltered for undersaturated conditions, we could in principle also study whether these intermediate densities would still be there. The results for undersaturated conditions, i.e. $S < 1$, are shown in Fig. 5c. The results of our analysis for the supersaturation range $S \in [0.7, 1.0]$ are rather remarkable: (i) precursor clusters are also present for undersaturated conditions and (ii) gain importance (in terms of likelihood to be observed) as the density of the motherphase is reduced, i.e. as the system gets farther from the coexistence line.

It is worth noting that the precursor clusters described in the present model will appear in the mother phase almost instantaneously, and will persist throughout the whole nucleation process. This is because they appear as a bump of probability in the

stationary cluster distribution. If anything, the time for them to be observed would be approximately the relaxation time of the cluster distribution, which is typically on the order of the diffusion time (which is negligible in most nucleation experiments). Regarding the characteristic size and density of such clusters, they are associated with the left branch (densification stage) of the nucleation pathway depicted in Fig. 3. Hence, their inner density is approximately the same as the critical cluster of the final equilibrium phase. Taking their associated range of densities, and checking the nucleation pathway, this means that these will be considerably smaller than the critical cluster, approximately on the order of one or two molecular radii.

Thus, on a qualitative level the characteristics of the precursor clusters observed in the model are comparable to the neutral species, i.e. ion pairs or larger, detected in the $SrSO_4$ co-titration experiments. Moreover, the observed evolution of the system with increasing supersaturation in the model and experimental results follow the same trend, i.e. with increasing supersaturation the role of a specific (in terms of size/density) class of precursor clusters in the nucleation process becomes less pronounced. The observed trend in the model at undersaturated conditions, i.e. increasing probability distribution of precursor clusters, could not be confirmed experimentally due to the large errors associated with the ISE measurements in the low concentration (undersaturation) regime of the $SrSO_4$ system. Notwithstanding, prenucleation clusters at undersaturated conditions have been observed experimentally for the $CaCO_3$ system[10].

5. Implications

Up to now, classical nucleation has been associated with a single energy barrier (black curve, Fig. 1), while non-classical (multi-step) nucleation pathways are usually linked to an energy landscape including multiple individual barriers and/or local minima (pink profile, Fig. 1). Nonetheless, the preliminary experimental and model results presented in this study point towards the fact that such a complex energy landscape is not a prerequisite to warrant multi-stage crystallization, since precursor species can also emerge due to the competition between thermodynamics and kinetics during cluster formation on a continuous uphill energy profile. Interestingly, the resulting effective energy landscape significantly changes as a function of supersaturation and reveals that more than one nucleation mechanism is attainable for one system without

changing the thermodynamic barrier of the system. It is important to note that the precursor particles observed in the model do not represent a thermodynamic phase, but rather transient particles that in a specific region of the U-shaped nucleation pathway have slower kinetics which renders them “observable”. Stated differently, this specific low kinetic region of the effective barrier corresponds with a certain size/density of precursor clusters, which disguises them as a microscopic phase with a local energy minima. It is not inconceivable to consider that such kinetically induced precursor clusters have been frequently observed in recent times due to the advent of imaging, scattering and spectroscopy tools with high spatial and time resolutions[3].

As in CNT, in our model nucleation also occurs through inherent thermal fluctuations that take the system over a nucleation barrier, which is largely defined by the chemical potential and mass-transport kinetics (opposed to the surface energy of the nucleus in CNT). The effective energy landscape that arises offers a plausible explanation for our data, as well as other *in situ* and *in silico* observations of systems where precursor clusters appear to play a decisive role, including $CaCO_3$[10], $CaSO_4$[19], NaCl[20], proteins[21], pharmaceutical compounds[22], quantum dots[23] or metals[24]. Future challenges to support our model concern the U-shaped nucleation pathway derived by MeNT. In particular, the initial long-wavelength low-density fluctuations, which have been observed in Monte Carlo simulations using forward-flux sampling[25], but still await experimental confirmation. Also, the current mono-component system should be extended to a multicomponent system, which will be a more realistic representation of e.g. salt nucleation. Additionally, the influence of the shape of the pathway on the probability distribution of precursor clusters needs to be addressed in detail.

6. Concluding Remarks

This work represents a frst attempt to merge experimental evidence of nonclassical mechanisms for nucleation and state-of-the-art theoretical advances that have been put forward in recent years. The application of such recent theories to experimental evidence has been severely hampered by the complexity of theoretical formalisms (for practitioners) and by the non-ideal experimental environment (for theoreticians). This has led to a parallel, yet largely disconnected, evolution of both theory and experiments. This needs to be resolved in order for the field to keep advancing. This work argues in favour of MeNT as a holistic nucleation theory capable of inherently capturing recent nonclassical observations without relying upon ad-hoc “designed” energy landscapes. Nonetheless, MeNT needs to further evolve in order to attain the capacity of fully describing multi-component systems. This is paramount to provide nucleation practitioners with a theoretical tool capable of predicting the outcome of a nucleation process.

Author Contributions:

A.R. Lauer contributed all experimental work as well as writing and figures pertaining to such as well as written responses to the Q&A.

M.A. Durán-Olivencia contributed the formulation of the MeNT model and the writing of the sections about the model and the model figures.

A.E.S. Van Driessche merged the contributions of A.R. Lauer and M. A. Durán-Olivencia and provided indroductory materials helping to link the experimental and theoretical studies of nucleation. Also provided supervision during the experimental stages of the work.

A. Fernandez-Martinez provided supervision for A.R. Lauer as well as discussion and editing during the manuscript preparation.

References

1. D. Kashchiev, *Nucleation: Basic Theory with Applications*, Butterworth-Heinemann, Oxford, 2000.
2. J. J. De Yoreo, P. U. P. A. Gilbert, N. A. J. M. Sommerdijk, R. L. Penn, S. Whitelam, D. Joester, H. Zhang, J. D. Rimer, A. Navrotsky, J. F. Banfield, *et al., Science*, 2015, **349**, aaa6760.
3. *New Perspectives on Mineral Nucleation and Growth: from Solution Precursors to Solid Materials*, ed. A. E. S. Van Driessche, M. Kellermeier, L. G. Benning and D. Gebauer, Springer International Publishing, Cham, 2017.
4. P. G. Vekilov, *Cryst. Growth Des*., 2010, 10, 5007–5019.
5. D. Gebauer, P. Raiteri, J. D. Gale and H. Colfen, *Am. J. Sci.*, 2018, **318**, 969–988.
6. J. De Yoreo, in *ACS Symposium Series*, ed. X. Zhang, American Chemical Society, Washington, DC, 2020, vol. 1358, pp. 1–17.
7. J. F. Lutsko, *J. Chem. Phys.,* 2012, **136**, 034509.
8. M. A. Durán-Olivencia, P. Yatsyshin, S. Kalliadasis and J. F. Lutsko, *New J. Phys.*, 2018, **20**, 083019.
9. J. F. Lutsko, *Sci. Adv.,* 2019, **5**, eaav7399.
10. D. Gebauer, A. Volkel and H. Colfen, *Science*, 2008, **322**, 1819–1822.
11. J. F. Lutsko and M. A. Durán-Olivencia, *J. Chem. Phys*., 2013, **138**, 244908.
12. K. Kelton and A. L. Greer, *Nucleation in Condensed Matter: Applications in Materials and Biology, Pergamon Materials Series*, 2009.
13. J. F. Lutsko and M. A. Durán-Olivencia, *J. Phys.: Condens. Matter*, 2015, **27**, 235101.
14. M. A. Durán-Olivencia and J. F. Lutsko, *Phys. Rev. E: Stat., Nonlinear, Soft Matter Phys.,* 2015, **91**, 022402.
15. J. Hansen and I. McDonald, *Theory of Simple Liquids*, Academic, San Diego, CA, 1986.
16. N. F. Carnahan and K. E. Starling, *J. Chem. Phys.*, 1969, **51**, 635–636.
17. D. L. Parkhurst and C. A. J. Appelo, User's guide to PHREEQC - a computer program for speciation, reaction-path, 1D-transport, and inverse geochemical calculations, *U.S. Geol. Survey Water Res. Invest. Rep.*, 1999, 99, 4259.

18. P. Blanc, A. Lassin, P. Piantone, M. Azaroual, N. Jacquemet, A. Fabbri and E. C. Gaucher, *Appl. Geochem.*, 2012, **27**, 2107–2116.
19. T. M. Stawski, A. E. S. Van Driessche, M. Ossorio, J. D. Rodriguez-Blanco, R. Besselink and L. G. Benning, *Nat. Commun*., 2016, **7**, 11177.
20. H. Hwang, Y. C. Cho, S. Lee, Y.-H. Lee, S. Kim, Y. Kim, W. Jo, P. Duchstein, D. Zahn and G. W. Lee*, Chem. Sci.*, 2021, **12**, 179–187.
21. A. E. S. Van Driessche, P. H. H. Bomans, R. R. M. Joosten, D. Gil-Carton, N. A. J. M. Sommerdijk and M. Sleutel, *Nature*, 2018, **556**, 89–94.
22. Y. Tsarfati, I. Biran, E. Wiedenbeck, L. Houben, H. Colfen and B. Rybtchinski, *ACS Cent. Sci.,* 2021, **7**, 900–908.
23. D. C. Gary, M. W. Terban, S. J. L. Billinge and B. M. Cossairt, *Chem. Mater.*, 2015, **27**, 1432–1441.
24. J. B. K. Cao, C. T. Stoppiello, R. L. McSweeney, T. W. Chamberlain, Z. Liu, K. Suenaga, E. Besley, S. T. Skowron, A. N. Khlobystov and U. Kaiser, *Nat. Chem.*, 2020, **12**, 921–928.
25. J. F. Lutsko and J. Lam, *Phys. Rev. E*, 2020, **101**, 052122.

Question and Response

This chapter was originally published in “Faraday Discussions”, a journal that hybridizes the publication and conference presentation of research. Part of the publication process involves a written Q&A with other conference participants. This Q&A is presented here (with minor modifications to make the discussion coherent with the chapter structure of this thesis). It represents an excerpt from the discussion published as “Understanding crystal nucleation mechanisms: Where do we stand?” that can be found in the same volume (235) of the journal in which this chapter was originally published. All responses were primarily written by A.R. Lauer and A.E.S. Van Driessche, then edited by M. A. Durán-Olivencia and approved by the entire author team before submission to the journal by A.E.S. Van Driessche.

Ruel Cedeno opened discussion of the paper by Alexander Van Driessche: Sulfate ions have been shown to form large solvation shells in water[1]. To some extent, this also occurs with strontium ions[2]. These shells may cause charge shielding which could reduce the sensitivity of the probes. This effect might be more pronounced at lower dosing rate since such solvation shells are more well defined in dilute solutions. Conversely, the hydration numbers decrease in concentrated solution[3]. Could this phenomenon play a role in the apparent consumption of neutral species (prenucleation clusters) during nucleation at low dosing rate which is not detected by the ion selective electrode (ISE)?

1. J. T. O’Brien, J. S. Prell, M. F. Bush and E. R. Williams, *J. Am. Chem. Soc.*, 2010, **132**, 8248–8249, DOI: 10.1021/ja1024113.
2. P. D’Angelo, V. Migliorati, F. Sessa, G. Mancini and I. Persson, *J. Phys. Chem. B*, 2016, **120**, 4114–4124, DOI: 10.1021/acs.jpcb.6b01054.
3. A. V. Dighe and M. R. Singh, *Proc. Natl. Acad. Sci. U. S. A.*, 2019, **116**, 23954–23959, DOI: 10.1073/pnas.1910691116.

Alexander Van Driessche (on behalf of all authors) replied: It is unlikely that the solvation shells described in the above works play a significant role in our measurements. The solvation shell for Sr^{2+} ions described in the source provided[1] was derived from a XANES measurement taken of a bulk liquid (volume unspecified) which would have averaged the absorption spectra across all Sr atoms present in the solution. Thus, the absorption spectrum must be primarily providing information on what we, in our work, considered “free” Sr^{2+} ions as they are the majority species – in

other words, we are measuring the hydrated Sr^{2+} ions with the ISE. It is also important to note that the particularly stable hydration shells of $n \sim 40$ for SO_4^{2-} ions found in ref. 2 may change with supersaturation in a manner not dissimilarly to the $41<n<47$ solvation shells simulated for glutamic acid.[3] It is a much larger leap in logic to presume that the measured and simulated hydration shell of $n = 8$ described in the Sr XANES study would necessarily be subject to the same effects. It is not theoretically impossible that there are some strongly hydrated Sr ions that are shielded from the ISE and participate in the early stages of nucleation. However, there is no data in our experiment, or any that we know of in literature, that would support this assertion.

1. P. D'Angelo, V. Migliorati, F. Sessa, G. Mancini and I. Persson, *J. Phys. Chem. B*, 2016, **120**, 4114–4124, DOI: 10.1021/acs.jpcb.6b01054.
2. J. T. O'Brien, J. S. Prell, M. F. Bush and E. R. Williams, *J. Am. Chem. Soc.*, 2010, **132**, 8248–8249, DOI: 10.1021/ja1024113
3. V. Dighe and M. R. Singh, *PNAS*, 2019, **116**, 23954, DOI: 10.1073/pnas.1910691116.

Aaron R. Finney questioned: In the chapter, you indicate that at the lowest dosing rates, the transmittance probe detected the formation of a *new phase* before the consumption of dispersed ions indicated by the change in the ISE signal (*i.e.*, the inflection point in the LaMer diagram). You suggest that this phase emerges *via* consumption of neutral species *e.g.* ion pairs. What is the nature of this phase and can you comment on the possible comparison between the bound species (prenucleation clusters) in $SrSO_4$(aq) *cf.* $CaCO_3$(aq)? Furthermore, how does your model differentiate between the nanoclusters and dense liquids/amorphous phases (see Figure 1 in this chapter) that could be involved in the nucleation pathway?

Alexander Van Driessche (on behalf of all authors) responded: Neither the probes used in the titration experiments, nor the model used in this work have the implicit capacity to precisely determine the nature of the (pre)nucleation species present during the nucleation process. In fact, the model is completely independent of any chemical information about what is nucleating. It provides only information about the relative density of nucleating phase as it traverses a free energy landscape from a perfectly mixed fluid state to a thermodynamically stable solid phase. Similarly, the potentiometric and optic techniques used in the titrations serve primarily to characterize the solution, *i.e.* the fluid that is not nucleating. For example, the ion selective electrode characterizes the quantity of unbound Sr^{2+} ions in the solution, but

does not provide a direct counting or characterization of the ions consumed in the reaction – any measures of those atoms are derived through subtraction from measurements carried out in the absence of any nucleation reaction (or pre-nucleation events). The most information gleaned about the nature of the phases formed during the titrations comes from the photometric sensor, and that is limited to a few minor details. We know that the phase is different enough from the solution surrounding it to form a light-scattering interface, and we can recover a limited qualitative measure of the concentration of those interfaces (higher turbidity = more interfaces). From the ISE data, and the information gleaned about bound species concentration, we could also attempt to extract some binding constants for the bound species and their dependence on time and supersaturation, but this analysis would create estimations blind to the actual structure and number of atoms contained in the bound species. Thus, we do not wish to speculate too extensively on the nature of the first formed phases. To obtain more insight on the nature of the transitory precursor cluster species other tools are necessary. For example, the structural properties of $CaSO_4$ precursor clusters have been derived by combining *in situ* high-energy X-ray diffraction experiments and molecular dynamics (MD) simulations[1].

The pathway monitored by ISE and the photometric sensor is comparable to the pathway observed for $CaCO_3$ (ref. 2) using an identical setup and similar to the pathway revealed for $CaSO_4$ using *in situ* X-ray scattering techniques[3,4]. The only aspect that awaits experimental confirmation is the existence of $SrSO_4$ and $CaSO_4$ prenucleation clusters in the undersaturated regime, as has been shown for $CaCO_3$ prenucleation clusters. In any case, our model does predict the existence of a prenucleation population for undersaturated solution conditions. The model used in this work (initially introduced in ref. 5) reveals that before crossing the nucleation barrier a kinetically induced cluster population appears; yet this does not represent a true thermodynamic phase. Eventually, the system will cross the barrier and a new phase will nucleate with a density close the final one. Noteworthy, after crossing the nucleation barrier the system will continue to (slowly) evolve approaching the ideal density of the crystalline phase. Taking into account this pathway, the population of kinetically induced clusters would correspond to nanoclusters/PNCs shown in Figure 1 in this chapter, and are clearly differentiated in our model because these occur on the pathway before crossing the nucleation barrier. The first nucleated phase could

potentially correspond to an amorphous phase because the density of this phase has not yet reached unity. Of course, this is one interpretation of the results and cannot be unequivocally confirmed from the current model. To do so, the simulations need to be run considering crystallinity as the variable, and not density as was done in the current work. In any case, the behavior observed in our model has been observed experimentally using *in situ* scattering during $CaSO_4$ precipitation at room and high temperature[3,4]. In these experiments, nanosized clusters formed first and subsequently aggregated into an amorphous phase (which is the first phase detected by an optical sensor). Eventually, a crystal structure develops through the reorganization of the nanosized clusters inside the disordered phase. Noteworthy, this reorganization continues long after the apparent precipitation reaction has finished. This is akin to what we observed in our model, where once the new phase has nucleated it will continue to evolve approaching the final density.

1. T. M. Stawski, A. E. S. Van Driessche, R. Besselink, E. H. Byrne, P. Raiteri, J. D. Gale and L. G. Benning, *J. Phys. Chem. C*, 2019, **123**, 23151–23158, DOI: 10.1021/acs.jpcc.9b04268.
2. P. I. Schodder, M. B. Gindele, A. Ott, M. Rückel, R. Ettl, V. Boyko and M. Kellermeier, *Phys. Chem. Chem. Phys.*, 2022, **24**, 9978–9989, DOI: 10.1039/D1CP05606A.
3. T. M. Stawski, A. E. S. Van Driessche, M. Ossorio, J. D. Rodriguez-Blanco, R. Besselink and L. G. Benning, *Nat. Commun.*, 2016, **7**, 11177, DOI: 10.1038/ncomms11177.
4. T. M. Stawski, R. Besselink, K. Chatzipanagis, J. Hövelmann, L. G. Benning and A. E. S. Van Driessche, *J. Phys. Chem. C*, 2020, **124**, 8411–8422, DOI: 10.1021/acs.jpcc.0c01041.
5. M. A. Durán-Olivencia, P. Yatsyshin, S. Kalliadasis and J. F. Lutsko, *New J. Phys.*, 2018, **20**, 083019, DOI: 10.1088/1367-2630/aad170.

Alan Hare enquired: Given that in Fig. 3 in the paper (https://doi-org.gaelnomade-1.grenet.fr/10.1039/d1fd00092f) the U-shaped curve ρ_0 tends towards a CNT limit, are you now able to draw any inference concerning the cluster shape? (I realise that this question could have a binary answer.)

Alexander Van Driessche (on behalf of all authors) answered: Clusters (or density fluctuations) are assumed to be spherically symmetric in mesoscopic nucleation theory (MeNT), consequently we only observe a spherical shape. Recently, a further generalization of MeNT has been put forward by Lutsko[1] allowing also for

non-spherically symmetric shapes to be considered. However, the resultant formalism equations are considerably more complicated than the ones involved in the spherically-symmetric MeNT.

1. J. F. Lutsko, *New J. Phys.*, 2018, **20**, 103015, DOI: 10.1088/1367-2630/aae174.

Stéphane Veesler queried: Nucleation is a localized phenomena there is a resolution issue by using a global measure such as a conductimetric one to detect it. You do not know where nucleation will occur. Cannot we say that the Δ*t* you observed is (by analogy) the growth time to a detectable size, this growth time being classically used in the interpretation of induction time measurement experiments?

Alexander Van Driessche (on behalf of all authors) responded: Indeed, it is important to consider growth when describing the nucleation events in the titration experiments. We do consider that the photometric sensor detects nucleation not at the formation of the first light scattering interface, but at the moment when the concentration/size of particles (and thus total amount of interfaces) present is significant to overcome the resolution limits of our sensor. Similarly, the ion selective electrode only detects nucleation when the change in free ion counts is significant enough to generate measurable change in the potential on the probe membrane – this would theoretically happen after the concentration of bound ions is greater than the detection limit for Sr^{2+} ions in solution. If we consider that the sensitivity threshold of both probes are comparable, then even if we do not detect only nucleation, but a combination of nucleation and growth, our main observation is still valid because when the photometric sensor is detecting the formation of a new phase, the ion selective electrode does not detect any change. Hence, the nucleation (and growth) of this new phase is mainly consuming bound species. We can also conduct a thought experiment where there is a distinct difference in detection limits for the probes. In this thought experiment, the nucleation process is assumed to be identical (classical) across all concentration ranges. We imagine classical nuclei that grow in size and number until the amount of interface present is enough to be detected by the photometric sensor. Sometime later the concentration of nuclei increases until enough ions have been removed from the solution to be measure potentiometrically. This is a perfectly reasonable explanation for the results of a single titration with one supersaturation rate. However, if this were the complete picture for how nucleation happens in this system, we would expect the sequence of particle detection to remain unchanged regardless

of the rate of ion addition. We would anticipate the same probes to have the highest sensitivity regardless of nucleation and growth rates. This is not what we see in the experiments.

Joonsoo Kim requested: Intuitively, larger nanoclusters should be more present at higher supersaturation but based on the observation in this work, larger nanoclusters are involved in the nucleation process when the concentration is low. May I ask your perspective?

Alexander Van Driessche (on behalf of all authors) replied: The involvement of large clusters in the nucleation pathway mentioned in this chapter (step 1, Figure 3) requires us to first reconsider the definition of “cluster”. Within the classical realm, namely Classical Nucleation Theory (CNT), clusters are thought to be small replicas of the final stable phase. This definition (also referred to as “capillary approximation”) leads to one of the main sources of problems for CNT, since it imposes the simplest possible nucleation pathway. Within the Mesoscopic Nucleation Theory (MeNT) framework, the concept of cluster is defined as the excess density with respect to the mother phase. This general definition, which lies at the core of MeNT, allows for the construction of a much more detailed theory of nucleation with enough flexibility to consider a much richer family of cluster and nonclassical nucleation pathways, and not just the classical kind. Within this context, the larger clusters (*i.e.* large-size–low-density fluctuations) that appear at the onset of the nucleation pathway obtained from MeNT, and are discussed in this work, are much larger in size than one molecular radius, but have an inner density that is much lower than the final phase and close to the mother phase. In this sense, the large clusters reported in this work are not replicas of the final phase. Instead, they are density fluctuations which extend several molecular radii in size, but whose intensity (or simply termed, average inner density) is very low. These initial large “clusters” are present in the nucleation pathway predicted by MeNT irrespective of the supersaturation.

Matteo Salvalaglio asked: The MeNT allows to describe nucleation using a multidimensional reaction coordinate space function of density and radius of the nucleus. Would it be possible to extend this approach to introduce additional parameters, such as measure of the order in the clusters/nuclei? Do you think there is a practical limit in the number of descriptors considered in this framework?

Alexander Van Driessche (on behalf of all authors) responded: Indeed, MeNT allows including as many order parameters as one might consider relevant to model nucleation. Some examples of other reaction coordinates considered under MeNT can be found, *e.g.*, in a previous work by Durán-Olivencia and Lutsko.[1] Additionally, a further extension of MeNT to consider other order parameters was carried out by Lutsko[2] in recent years. This new extension provides a roadmap to systematically develop nucleation theories considering all types of cluster geometries and reaction coordinates. Although there is no easy rule of thumb, or practical limit, to decide the optimal number of descriptors, we have observed that the complexities of the resultant equations grow exponentially with the number of order parameters.

1. M. A. Durán-Olivencia and J. F. Lutsko, *Phys. Rev. E*, 2015, **91**, 022402, DOI: 10.1103/PhysRevE.91.022402.
2. J. F. Lutsko, *New J. Phys.*, 2018, **20**, 103015, DOI: 10.1088/1367-2630/aae174.

Chapter 2

Deciphering strontium sulfate precipitation via Ostwald's rule of stages: From prenucleation clusters to solution-mediated phase transformation

A.R. Lauer[1], R. Hellmann[1], G. Montes-Hernandez[1],

N. Findling[1], W.L. Ling[2], T. Epicier[3], A. Fernandez-Martinez[1], A.E.S. Van Driessche[1,4]

[1] Université Grenoble Alpes, Université Savoie Mont Blanc, CNRS, IRD, IFSTTAR, ISTerre, 38000 Grenoble, France.
[2] Université Grenoble Alpes, CEA, CNRS, IBS, F-38000 Grenoble, France
[3] Université de Lyon, Université Claude Bernard Lyon1, IRCELYON, umr CNRS 5256, 69626 Villeurbanne Cedex, France
[4] Instituto Andaluz de Ciencias de la Tierra (IACT), CSIC – University of Granada, Armilla, Granada E-18100, Spain

Abstract

Multiple-step nucleation pathways have been observed during mineral formation in both inorganic and biomineral systems. These pathways can involve precursor aqueous species, amorphous intermediates, or metastable phases. Despite the widespread occurrence of these processes, elucidating the precise nucleation steps and the transformation mechanisms between each step remains a challenging task. Using a suite of potentiometric, microscopic, and spectroscopic tools, we studied the nucleation pathway of $SrSO_4$ as a function of the physicochemical solution parameters. Our observations reveal that below a threshold supersaturation, nucleation is driven by bound species, akin to the prenucleation cluster model, which directly leads to the formation of the stable phase celestine, $SrSO_4$. At higher supersaturations, this situation is altered, with nucleation dominated by the consumption of free ions. Importantly, this change in nucleation mechanism is coupled to the formation of a hemihydrate metastable phase, $SrSO_4 \cdot 1/2H_2O$, which eventually transforms into celestine, adhering to Ostwald's rule of stages. This transformation is a solution-mediated process, also occurring in the presence of a fluid film and is controlled by the physico-chemical parameters of the surrounding environment. It proceeds through the dissolution of the metastable phase and the *de novo* crystallization of the final phase. Overall, our results reveal that ion association taking place during the prenucleation stage dictates whether the nucleation pathway goes through an intermediate phase or not. This also underlines that although Ostwald's rule of stages is a common process, it is not a prerequisite for mineral formation—even in systems where it can occur.

1. Introduction

Recent experimental studies have highlighted the importance of complex, and in particular multiple-step, nucleation pathways to mineral formation in both natural and engineered environments[1]. Such nucleation schemes have been suggested as a means for the concentration, transportation, and/or temporary storage of ions during biomineralization[2,3]. They have also been used to describe the behavior of inorganic solutions with high supersaturation[e.g.4]. A wide variety of distinct nucleation pathways have been described thus far, ranging from nano-crystal aggregation[e.g.5] to amorphous particle integration[e.g.6] and ion-complex agglomeration[e.g.7]. Many of these precursor phases, or intermediates, are aqueous species that are not taken into account by current thermodynamic speciation models, simply due to the lack of thermochemical data about them, which can be difficult to obtain due to the short-lived character of the species (e.g., transient polynuclear clusters[8-10]). However, some studies have shown that the stoichiometry of these amorphous precipitates can vary during the precipitation process, making them questionable thermodynamic phases[11,12]. Often, the precipitation pathway goes through the formation of one (or multiple) discrete metastable phase(s), a concept introduced proposed by Ostwald in 1897[13], and commonly referred to as 'Ostwald's rule of stages'. Intermediate phases, either amorphous or crystalline, can be sufficiently long-lived, thus allowing their physico-chemical characterization. Nonetheless, even in such cases, elucidating the transformation reaction to the more stable phase, e.g., through a solid-state or fluid-mediated reaction, remains a challenging task[e.g.1].

Despite the widespread interest and relevance of (re-)examining nucleation pathways in natural and engineered environments, the formation mechanisms of sulfate minerals (which comprise ~7% of known minerals in the earth's crust[14]) have received surprisingly little attention, with the only exception being calcium sulfate[8,15,16]. Strontium sulfate is abundant in various earth surface environments, with concentrations reaching saturation in marine sediment porewaters in varied geological settings[17]. Additionally, the precipitation of $SrSO_4$ solid phases is important factor in the design of offshore oil wells in order to avoid scaling and clogging[18,19]. The anhydrous mineral form, celestine ($SrSO_4$), is the principal ore of strontium and is the starting material for producing strontium metal and virtually all strontium salts. The sulfate also is used in pyrotechnics and in ceramics[20]. In addition, strontium sulfate is

also found as biominerals, forming the shells of several acantharian protozoa[21]. At the present, relatively little is known about the formation mechanisms of celestite. Some studies reported on the precipitation within the scope of classical nucleation theory,[eg. 22-24] ^{5–7}^{5–7}while others merely focused on quantifying the nucleation kinetics of celestine[25-31]. The effect of additives[32-35] on the nucleation and growth of celestine has also been examined. It is interesting to note that a transient strontium sulfate phase was described as early as 1926[36]⁸⁸. Until now, this intermediate has only been isolated and characterized as a partially hydrated phase, $SrSO_4 \cdot 1/2H_2O$[37] (for simplicity, it will be referred to as 'hemihydrate' for the remainder of this chapter). It has been shown that the formation of this phase is controlled by the degree of supersaturation, as well as the presence of silicon in solution[38]. Despite these studies centered on the metastable phase, virtually no attention has been directed to the role the hemihydrate plays in the formation of celestine.

In this work, we deciphered the different steps of the precipitation process of strontium sulfate from aqueous solutions, including the precursor and intermediate phases, and established the nucleation pathways as functions of the physico-chemical parameters. In addition, we performed a detailed characterization of strontium sulfate hemihydrate, unveil conditions that lead to an elevated kinetic persistence of the phase, and demonstrated that dissolution-reprecipitation is the most likely mechanism controlling the transformation of the hydrated metastable phase to anhydrous celestine, the final stable phase. Here, we make progress towards a cohesive understanding of nucleation processes obeying Ostwald's rule of stages, and in particular, the (trans)formation of hydrated to anhydrous sulfate minerals in particular, through a careful investigation of fluid-mediated reactions taking place in the $SrSO_4$-H_2O system.

2. Materials and Methods

2.1. Precipitation of SrSO4 phases and their isolation

All solutions used for the precipitation experiments were created by mixing equal volumes of equimolar (100 mM) solutions of $SrCl_2$ (99% extra pure $SrCl_2.6H_2O$, Acros Organics) and Na_2SO_4 (≥99%, Roth) dissolved in deionized water. The saturation index with respect to pure celestine – $\Omega = \log[a(Sr^{2+}) \cdot a(SO_4^{2-})/k_{sp,celestine}]$, where $a(Sr^{2+})$ and $a(SO_4^{2-})$ are the activities of Sr^{2+} and SO_4^{2-} ions in solution and $k_{sp,celestine}$ is the solubility product of celestine ($10^{-6.62}$) – was calculated for all solutions using Phreeqc and the BRGM Thermoddem geochemical database.

The optical characterization of the nucleation reaction was conducted in a UV-VIS Cary 3500 (Agilent) instrument. Strontium sulfate precipitation experiments were carried out by mixing equal volume of $SrCl_2$ and Na_2SO_4 stock solutions into a 100mM NaCl solution (to maintain a constant background ionic strength). In all cases, the final solution had a volume of 2 mL, and the $SrSO_4$ concentration varied from 3.5 to 15 mM. The solutions were mixed in a standard 12.5x12.5 mm^2 poly(methylmethacrylate) (PMMA) cuvette (BRAND gmbh) and agitated with a magnetic stirrer at 800 rpm. Time resolved absorbance curves were collected at a wavelength length of 500 nm.

The evolution of the ionic environment during the early stage of strontium sulfate nucleation was probed via potentiometric cotitration experiments. For these experiments, equimolar concentrations of the previously described $SrCl_2$ and Na_2SO_4 solutions were dosed at controlled rates into 50 mL of deionized water in a reactor vessel that was continuously mixed with a magnetic stirrer bar at 500 rpm. Dosing rates were controlled by a Metrohm 905 Titrando equipped with two 800 Dosino devices, each utilizing a 20 mL dosing unit. The evolution the precipitation reaction was continuously monitored based on turbidity (Metrohm optrode), conductivity (Metrohm 5-ring conductivity measuring cell) and cation concentration (Ion Selective Electrode that consisted of two half-cells: a Metter-Toledo DX337 membrane and a Metrohm LL ISE reference electrode).

The solid phases (hemihydrate and celestine) obtained after mixing the equimolar solutions were isolated at different time points of the precipitation reaction by a fast vacuum filtering process employing filtration membranes (0.5 µm). To obtain nearly pure hemihydrate, equal volumes of equimolar solutions of 100 mM $SrCl_2$ and

100 mM Na_2SO_4 (i.e., 50mM $SrSO_4$ with 100 mM NaCl and Ω=2.6) were added directly to the filtering apparatus and gently stirred by hand for ~5 s until the hemihydrate resembled a gel and appeared relatively stable. At this point, water was then rapidly removed via a vacuum system. Once there was no visible presence of water, EtOH (95% v/v, Fisher) was added to remove background salts and halt any further reactions. A total of 3 EtOH rinses were completed for each sample. After the third rinse and a vacuum assisted drying process, the obtained solid phase cake was ground for further analyses. Importantly, the filtration and cleaning steps did not significantly alter the phase(s) being isolated (see results for details).

2.2. Characterization of the solid samples

2.2.1. Powder X-ray analysis

The composition of the solid samples was first evaluated with powder X-ray diffraction (PXRD). PXRD patterns were recorded with a Bruker D8 powder diffractometer equipped with a SolXE Si(Li) solid state detector from Baltic Scientific Instruments using $CuK\alpha_{1+2}$ radiation. Intensities were recorded at 0.026° 2-theta step intervals from 5 º to 90º with 6 s counting time per step. Data were evaluated using the code DIFFRAC.EVA for comparison to previously published structures (ICDD PDF 00-005-0593 for celestine and ICSD 167 054 for the hemihydrate). Approximately 1 g of powder was analyzed for each sample. The analyzed celestine powder had a granulometry <50 µm. The hemihydrate was broken up as much as possible inside a plastic beaker using a spatula to produce a fine-grain powder (hemihydrate rapidly transformed to celestine when using a sieve or mortar and pestle). For other *ex situ* characterizations of the hemihydrate, such as infrared spectroscopy and electron microscopy, the purity of each sample was confirmed by PXRD to be >95%. For the celestine samples, only those where no hemihydrate was identified (purity >99%) were used for further characterization.

2.2.2. Fourier-transform Infrared spectroscopy (FTIR)

Fourier-transform infrared spectroscopy was performed to obtain spectral information that was used to confirm the presence of hemihydrate in mixed systems. FTIR analysis was performed in ATR mode (Thermo Scientific Nicolet iS50). Dry and wet powder samples were placed onto the diamond window. Dry powders were gently compressed to achieve maximum surface contact with the diamond window, while

suspended powders were allowed to remain dispersed. The spectra were normalized to the highest absorbing peak (neglecting noise due high water absorbance in wet samples at wavenumbers 400-800 cm^{-1}). The spectra were evaluated for peak shifts, shape changes, and peak ratio inversions that allowed for the differentiation of hemihydrate from celestine.

2.2.3. Electron microscopy

A variety of electron microscopy techniques were used to characterize the hemihydrate and celestine. Hemihydrate and celestine powders were dispersed directly onto metal stubs with an affixed conductive carbon tape; no coatings were applied. Samples were observed with scanning electron microscopy (SEM) and field emission gun SEM (FEG-SEM). Low resolution SEM was carried out using a Vega 3 Tescan instrument at 16.0 kV, while FEG-SEM was conducted on a Zeiss Ultra 55 FEG-SEM at 3 kV.

Cryogenic Transmission Electron Microscopy images were acquired with a Ceta CMOS camera under low-dose conditions on a Tecnai F20 microscope operating at 200 keV. Samples were prepared by placing 4 µl aliquots of the reaction solution on glow discharged Quantifoil or lacey carbon film grids and vitrified using a Thermofisher Vitrobot. Blotting times were adjusted to obtain adequate ice thickness.

High-resolution transmission electron microscopy (HRTEM) observations were made with a Cs-corrected FEI Titan ETEM G2 80-300kV (for this work, images were acquired under vacuum conditions typical of non-environmental TEM). Samples were prepared by dispersing a small amount of hemihydrate in alcohol, placing a droplet of suspension on a TEM grid, and evaporating the excess EtOH in a bell jar pumped down using a low vacuum primary pump. Imaging was carried out at 80 and 300 kV. According to specific irradiation tests, it was concluded that the hemihydrate material could bear electron doses up to 10^4 e^- $Å^{-2}$ with a typical low electron flux of about 50 e^- $Å^{-2}$ s^{-1} at 300 kV without significant observable damage. This corresponds to a maximum of about 3 minutes of continuous illumination without any detectable morphological changes. 4 x 4 k^2 images were recorded with an advanced CMOS Oneview camera (Gatan) after a few seconds of exposure to the electron beam, with cumulative acquisitions of about 1s based on an average of 40-120 ms elementary frames. Thus, images were collected over much shorter time periods that the aforementioned limits associated with observable damage occurring.

We performed crystallographic identification of selected TEM micrographs using FFT of high-resolution micrographs instead of selected area electron diffraction (SAED) patterns. One of the advantages of using a Cs-corrected TEM is its superior spatial resolution, which facilitates lattice plane imaging, even along more or less exotic azimuths. Numeric Fourier transforms can then be used to provide diffraction spots, allowing classical indexing. This methodology allowed us to directly select single fibers or particles for analysis, including even very local, nanometer-sized areas within such objects—doing the same with SAED would require a highly focalized beam that could result in beam damage. With this technique, we were, therefore, able to remain in imaging mode (rather than switching between imaging and diffraction modes) and avoid significant irradiation effects under the illumination conditions used here.

2.3. In situ analysis of solid phase transformation

2.3.1. FTIR and Raman

In situ observations were conducted both with FTIR and Raman spectroscopy. For the FTIR-based experiments, 2 mL of the previously described 50 mM $SrSO_4$ solution was prepared. After the precursor gel formed, excess water was removed with a pipette to halt the reaction, and a small quantity of gel was transferred, using a spatula (without compression), onto a diamond crystal for ATR mode analysis. To restart the reaction, a droplet of deionized water was added to replicate solution conditions of the reaction beaker where the gel phase initially formed. Each presented spectrum represents the average 15 individual scans conducted in 20 s intervals using a Nicolet iS50 FTIR Spectrometer (Termo Scientific) configured with a DLaTGS detector (KBr window).

In situ Raman was conducted on a solution made by combining 100 mL of each of the two 100 mM stock solutions (Na_2SO_4 and $SrCl_2$) and mixing the resulting (200mL) solution. The *in situ* Raman measurements of the solution were carried out in a custom-built 600mL Hastelloy C22 reactor with an integrated raman probe (Optical Systems Raman RXN1; for a detailed description of the setup see Montez-Hernanez and Renard[39]). Spectra were collected from 100 to 3425 cm^{-1}, averaging three scans over 15 seconds with a time interval of 1 minute between scans. Under these conditions, only one sulfate peak was readily observable, so evaluation was focused on the wavenumber band from 965-1025 cm^{-1}. To initiate the precipitation reaction the suspensions were mixed for ~1 s at 300 rpm using a twin bladed mixer, followed by

mixing at 50 rpm – this served to slow down the transformation reaction while providing sufficient agitation to homogenize the solution and minimize the risk of measuring local anomalies. The shown spectra represent the average of three measurements over ~5 s, and unless otherwise specified, untreated data are presented here.

2.3.2. Electrochemical probes

An additional *in situ* direct mixing experiment was conducted using electrochemical probes. 150mL of the 50mM $SrSO_4$ solution was prepared in a 250 mL beaker (75 ml of 100 mM Na_2SO_4 added to 75 ml of 100mM $SrCl_2$) and mixed with a 2 cm PTFE coated stirrer bar (50 rpm). The reaction was monitored with a Metrohm 5-ring conductivity measuring cell (c = 0.7 cm^{-1} with Pt1000; part no. 6.0915.100), a Metrohm optrode (part no. 6.115.000), and an ion selective electrode (ISE) that consisted of two half-cells: a polymer membrane cation ISE with a silver/silver chloride reference electrode. Probes were connected to a Metrohm 905 titration unit and controlled by Tiamo 2.5 software.

2.3.3. Powder X-ray diffraction (PXRD)

In situ PXRD was conducted in a TTK Anton Paar chamber with a ProUmid humidity controller. Samples were kept at 23 °C during data collection, whereas the desired relative humidity value (RH) was maintained (±2% RH) by using a constant flow of mixed dry/saturated air. RH was continuously monitored with a hygrometer located next to the sample. Samples were equilibrated at the desired humidity (ranging from 70 to 90%) for a minimum of ten minutes before starting data collection.

To increase time resolution, counting time was reduced to 3 s, and scanning was limited to the 2θ ranges from 12° to 16° and 30° to 34° in order to focus on one unique peak for hemihydrate (14.28°) and one unique peak for celestine (32.79°). Mass fractions of the phases were estimated using a semi-quantitative reference intensity ratio (RIR) technique[40,41], based on the relation that the intensity (peak height) of an XRD peak is defined by:

$$I_a = \frac{K_a x_a}{\mu_s \rho_a}$$

where K_a is a material parameter for phase *a*, ρ_a is the density of the phase, μ_s is the permittivity of the entire sample, and x_a is the mass fraction of phase *a*. Taking the ratio

of the intensity of each respective peak of interest for the two different phases, and grouping the material constants (including density) into a single term, *K*, the mass fraction of a phase can be determined solely from the ratio of the two peak heights.

$$\frac{I_a}{I_b} = \frac{K_a x_a \rho_b}{K_b x_b \rho_a} = K\frac{x_a}{x_b}$$

In the absence of additional phases $x_a + x_b = 1$, and assuming that $\frac{I_a}{I_b} = R$, then

$$x_a = \frac{R}{K+R} \; and \; x_b = \frac{K}{K+R}$$

The intensities of the peaks I_a and I_b that were tracked in this experiment are located at 2θ = 14.26 for hemihydrate and 32.79 for celestine. At the end of the experiment, a full spectrum was taken and Rietveld integration was used to estimate the final concentrations x_a and x_b. These concentrations and the intensities I_a and I_b from the last *in situ* time point were used to determine *K* for each experiment.

For experiments at 70 and 80% relative humidity, it was found that I_a/I_b in the full spectrum at the end of the experiment matched the I_a/I_b ratio after ~9h. The calculations were repeated using that time point as a reference, and the difference between the two estimations of concentration was subsequently used as an estimate of the error. For the experiment at 90% humidity, no such "ratio matching" point existed, so the error was assumed to be the maximum found at any point during the two lower humidity experiments.

2.3.4. Optical microscopy

An optical microscopic visualization of the transformation from the hemihydrate to celestine was conducted using a Leica M125 equipped with a ring light and backlight illumination. The reaction was conducted in a silica glass capillary (graciously supplied by Vitrex Medical) with the following dimensions: inner diameter = 1.42 mm, outer diameter = 1.80 mm, length = 75 mm. One end of the capillary was briefly dipped into molten paraffin wax to form a seal, followed by the introduction of 100 mM Na_2SO_4 into half of the capillary, then 100 mM $SrCl_2$ to fill the remaining half of the capillary, leaving a diffusion front at the center, and finally, the other end of the capillary was sealed. A simple schematic of this experimental setup can be found alongside the results of the experiment (Fig. 7). The formation of the hemihydrate occurred within the first seconds

after the introduction of the $SrCl_2$ to the point that crystals could be seen by eye by the time that the capillary was sealed (5-10 s after injection). The sealed capillary was subsequently placed under the microscope with an alignment and focusing procedure that took ~2 minutes. Images monitoring the transformation from hemihydrate to celestine were acquired approximately every 20 s for a duration of 6 h.

3. Results and discussion

3.1. Nucleation pathways in the SrSO4-H2O system

We studied the nucleation pathway of $SrSO_4$ at different degrees of supersaturation. This was accomplished through direct mixing experiments (Fig. 1a) and potentiometric co-titrations (Fig. 2). Powder x-ray diffraction of the precipitates (Fig. 1b) indicated that the first solid phase to appear depends on the initial supersaturation of the reaction. At the lowest supersaturations tested, a direct nucleation pathway was followed, resulting in the precipitation of celestine without observable intermediates. At the highest supersaturations, a two-step pathway occurred where a metastable hemihydrate formed first, followed by the thermodynamically more favorable anhydrous phase (a detailed characterization of both solid phases is provided in section 3.2). The lower limit for the formation of the hemihydrate was determined to be ~9-10 mM (corresponding to a saturation index of Ω=1.55 with respect to celestine). This limit was determined through the direct mixing experiments that took place in a UV-Vis cuvette with agitation at 800 rpm. As seen in Fig. 1a, the shape of the absorbance vs. time curves changes at the 9-10 mM limit. At higher concentrations, there is a peak and an inflection point in the absorbance curve after the initial nucleation. This coincides with a maximum concentration of the high surface area needles that characterize hemihydrate, which then subsequently dissolved and formed celestine (this transformation process is discussed in detail in section 3.3.). Below the 9-10 mM limit, there is just an increase in the turbidity, which can be attributed to the direct nucleation and growth of celestine. This limit is corroborated by monitoring the sulfate concentrations using *in situ* Raman (see section 3.3). From these induction time measurements, an effective interfacial energy for celestine of 35 mJ m^{-2} was obtained (Fig. S1), which compares well with previously reported values (Table S1). We also estimated the interfacial energy for hemihydrate (Fig. S1): ~3 mJ m^{-2}, which is considerably lower than that of celestine.

In order to probe the evolution of the ionic environment during the early stage of strontium sulfate nucleation, equimolar concentrations of $SrCl_2$ and Na_2SO_4 were co-titrated at a steady rate into a reaction vessel containing 50 mL of deionized water, and the resulting electrolyte solution was continuously monitored for cation concentration, turbidity, and conductivity. The first stage of these co-titrations is characterized by a monotonic increase of Sr^{2+} activity and conductivity, and a

maximum steady state transmittance signal (Fig. 2a). During this first stage, the detected amount of detected free Sr^{2+} is lower than the total added strontium, indicating the presence of bound ions[42]. Note also that these two curves increasingly diverge with time. A second stage is reached when transmittance abruptly decreases, followed by a change in the shape of the free ions (Fig. 2a) and conductivity curves (data not shown). These changes correspond to the onset of nucleation and the critical supersaturation (Ω_{crit}) at which it occurred. This critical supersaturation was controlled by varying the ion addition rate (i.e., at higher addition rates, higher critical supersaturations are reached, and vice versa, Fig. 2b).

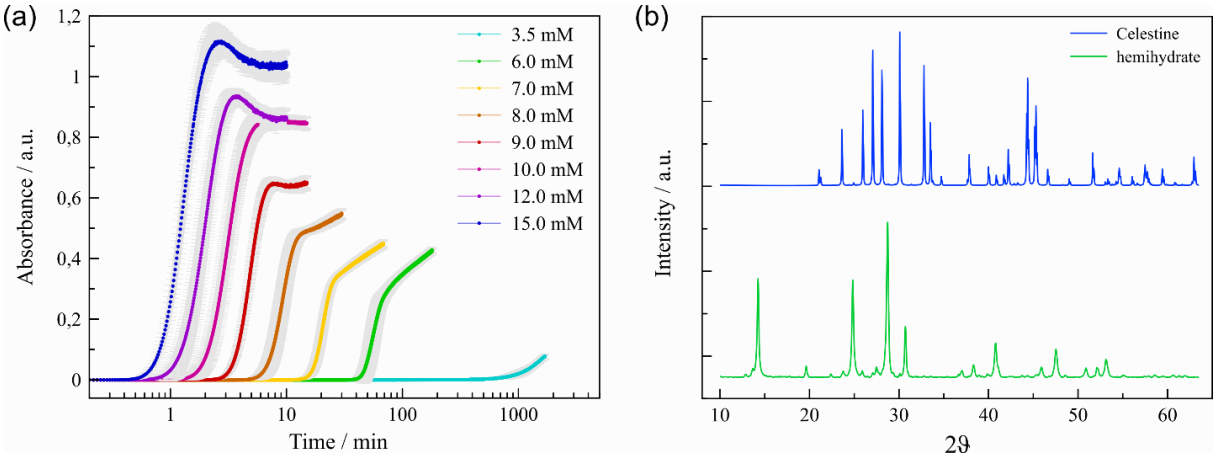

Figure 1: *Precipitation of solid phases in the $SrSO_4$-H_2O system. (a) UV-Vis absorbance curves measure induction times as a function of the initial $SrSO_4$ concentration. (b) PXRD spectra of the celestine ($SrSO_4$) and hemihydrate ($SrSO_4$·1/2H2O).*

The data shown in Fig. 2 reveal some important mechanistic information. There is a significant difference between the nucleation times measured by the transmittance probe and those measured by the ISE and conductivity probes (inset Fig. 2a). At the lowest Ω_{crit} the transmittance probe detected the formation of a new phase significantly before the ISE and conductivity probe registered the consumption of free ions (Fig. 2b). This observation indicates that the onset of strontium sulfate nucleation occurs via the consumption of bound, i.e. neutral, species ($SrSO_4^0$ or larger) that go undetected by the ISE and conductivity probe. Consequently, the particles detected by the transmittance probe are formed through the aggregation of neutral particles, the smallest of which could be ion pairs. At the two highest Ω_{crit}, the early detection of nucleation by the transmittance probe vanishes (Fig. 2c) and the first stage of nucleation is mainly driven by ion consumption and not by neutral bound species. In the previous chapter[42] we provided a tentative explanation of the change in dominant species controlling the early stages of nucleation: according to MeNT modeling, the

presence of some prenucleation species can be described by a kinetic “slow step” that results in relatively long-lived species that does not require a thermodynamic minimum. Thus as the reaction accelerates, the importance of the kinetically apparent species diminishes.

Thus, these co-titration experiments, conducted at different addition rates, reveal that below a threshold supersaturation the onset of nucleation is dominated by the consumption of bond species (ion pairs or larger), akin to the prenucleation clusters observed for $CaSO_4$[8,9], $CaCO_3$[43], $CaPO_4$[44] or $Mg(OH)_2$[45], among others. Above this threshold supersaturation, the onset of nucleation is characterized by the consumption of both bound and unbound species. Of significant note here, the threshold supersaturation at which this change in nucleation pathway occurs corresponds to the critical supersaturation ($\Omega \approx 1.55$) when the hemihydrate starts to form. This suggests that the reaction step related to the consumption of bound species diminishes in importance as the rate of the reaction increases, similar to the MeNT prediction for the behavior of prenucleation species. Overall, these results suggest that changes in the system during the prenucleaiton phase are coupled to a pathway that forms via a metastable intermediate phase or not. It could be argued that it is energetically more favorable to form a hydrated phase from fully solvated charged ions than from ion pairs/PNC’s that have already removed part of their hydration shell (compared to ions), which would explain why celestine nucleation is driven by bound species and the hemihydrate is dominated by charged ions[46]. In summary, the experimental observations discussed above reveal that as the supersaturation rate, and thus also the critical supersaturation, increases during $SrSO_4$ co-titrations, the preferred nucleation mechanism changes.

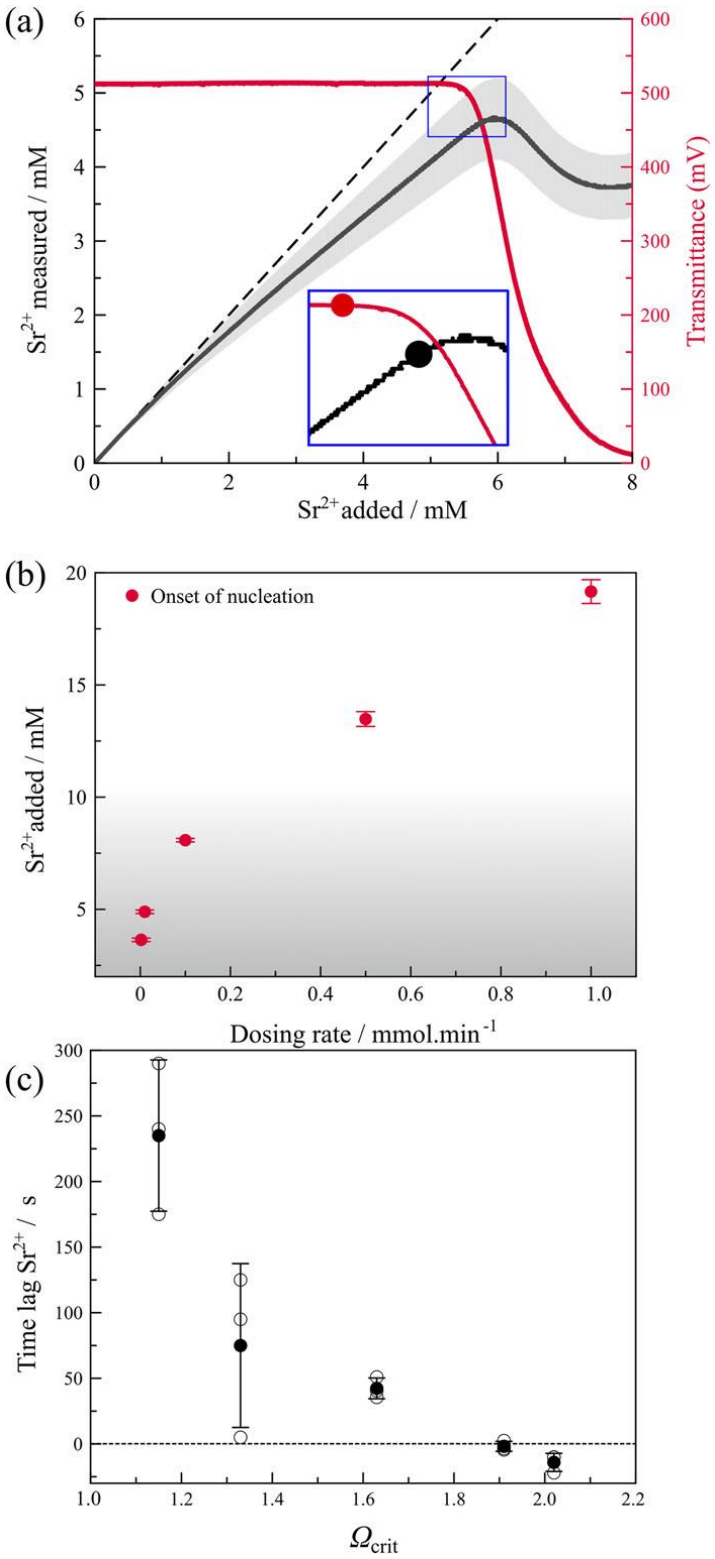

Figure 2: *Evolution of the ionic environment during the early stage of strontium sulfate nucleation. (a) Cation Sr^{2+} concentration as measured by an ion selective electrode (black), optical transmittance of the solution (blue), and the conductivity (red) measured in situ during an equimolar co-titration experiment. (b) Concentration at the onset of nucleation determined by the transmittance probe for each dosing rate of $SrSO_4$ in co-titrations tested in this study (c) Difference in measured nucleation induction time determined by a transmittance and a ISE probe as a function of S_{crit}. A positive difference means the transmittance probe detected the phase transition first (i.e. before the ISE probe). The gray dotted line corresponds to equal induction times. Error bars represent the standard deviation of three replicate experiments.*

3.2. Characterization of the solid phases forming in the $SrSO_4$-H_2O system

As discussed above, during the precipitation of $SrSO_4$ from highly supersaturated solutions (Ω > 1.55) an intermediate phase is formed first, which subsequently transforms into the stable anhydrous phase. In order to characterize the two solid phases and track their temporal evolution, we selected a specific reaction condition (50 mM $SrSO_4$, Ω = 2.60) where the solution turbidity rapidly increases within 1–2 s upon mixing of both reactants ($SrCl_2$ and Na_2SO_4), due to the formation of precipitates that aggregate into white, cloud-like emulsions. These aggregates increase in concentration until a gel-like concentrate is formed. This gel concentrate is composed of the intermediate hemihydrate, and over time (~100 min), it is fully replaced with particles that settle to the bottom of the reactor vessel. Below, we describe the different strontium sulfate phases, followed by details on the transformation of the intermediate hydrous phase to the final celestine phase (Section 2.3).

Using our isolation protocol (see “Materials and methods”), we were able to obtain (>99%) pure samples of both phases. Powder x-ray diffraction and Rietveld refinement were used to identify and quantify both phases (Figure 1b). The hemihydrate phase crystallizes in the hexagonal system, with unit cell dimensions of *a* = 7.178 and *c* = 6.589 Å, confirming previously reported data[38]. The *c* axis lies parallel to the axial direction of the needle-like fibers. In contrast, anhydrous celestine crystallizes in the orthorhombic system and has the following cell parameters: *a* = 8.360 Å, *b* = 5.352 Å, *c* = 6.858 Å (PNMA)[47]. Detailed structural analyses (see Table S2) revealed that the crystalline intermediate phase, hydrated strontium sulfate, contains half a molecule of water per molecule of strontium sulfate ($SrSO_4 \cdot 1/2H_2O$). This is analogous to the hemihydrate of calcium sulfate (bassanite; $CaSO_4 \cdot 1/2H_2O$), which is a common intermediate phase during gypsum ($CaSO_4 \cdot 2H_2O$) or anhydrite ($CaSO_4$) formation[5,48,49].

SEM imaging (Figures 3a and 3b) of the hemihydrate and celestine phases reveals a distinct morphological difference between the two, the former being fibrous with a very high aspect ratio (L/W > 100) and the latter being prismatic. The high density of these fibrous aggregates is most likely responsible for the gel-like phase observed in solution. Importantly, cryo-TEM (Figure 3c) imaging of aliquots retrieved from the early stages of the reaction further reveals the extreme elongated morphology

of the hydrate phase, which, quite surprisingly, shows evidence for non-brittle behavior by bending of the thinnest crystals (see inset Figure 3c). This property may contribute to the entanglement of these fibers and the formation of the observed gel-like nature of the initial precipitate. Cryo-TEM images of aliquots collected at the end of the reaction showed prismatic celestine crystals (Figure 3d). HRTEM imaging and fast Fourier transforms (Figures 3e and 3f) confirm the respective microstructural equivalence of the hemihydrate and celestine observed in both TEM experiments with that measured by x-ray diffraction. Importantly, the cryo-TEM and *ex situ* SEM and TEM images all reveal the same morphologies for the hemihydrate and the celestine, demonstrating that the filtration and cleaning steps do not significantly alter the phase being probed. Furthermore, no obvious structural/epitaxial relationship was observed between the two phases.

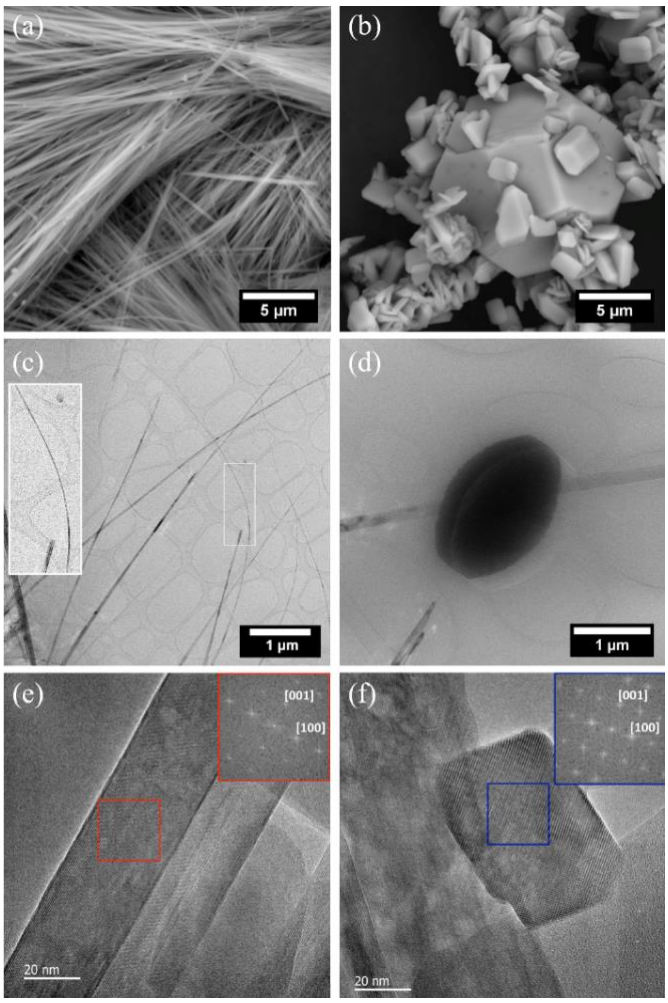

Figure 3: *Characterization of the solid phases forming during $SrSO_4$ precipitation from solutions using electron microscopy. SEM image of bundled fibrous hemihydrate phase (a) and celestine crystals (b) in a variety of morphologies and sizes. Cryo-TEM images of hemihydrate fibers (c) and a celestine crystal (d). HRTEM images of a hemihydrate fiber (e) and a celestine crystal adjacent to a hemihydrate fiber (f). The corresponding FFT of selected areas (red, blue boxes) of the respective crystals is shown in insets, and the spots on the FFT patterns indicate the crystallographic planes.*

Ex situ FTIR (Figure 4a) analyses of both phases shows two characteristic SO_4 vibrations, at ~600 and ~1100 cm^{-1}. These represent the symmetric bend (v_4) and asymmetric stretch (v_3) of the O–S–O (or resonant O=S=O) bonds[50], respectively. A smaller peak around 992 cm^{-1} can be attributed to the v_1 asymmetric bend vibration mode[50]. Additionally, the hemihydrate phase has two peaks due to structural water at 1637 and 3523 cm^{-1}. Figure 4b shows the evolution of the two principal sulfate peaks between 500 and 1300 cm^{-1} during the different stages of the nucleation pathway from solution to the intermediate phase and to early nucleated nanometer-sized celestine (~100 nm range) and celestine particles that have had time to grow into considerably larger crystals (1 μm). Infrared spectra were recorded both in solution (wet) and after filtering and drying of the solid phases. This did not significantly influence the position of the main peak locations. However, a red shift in the v_4 vibration peak can be observed, from 1084 to 1072 cm^{-1}, for celestine as it grows from nanometer-sized (brown, Figure 4b) particles to large bulk crystals (blue, Figure 4b)[51]. The v_1 vibration peak at 992 cm^{-1} appears to be largely absent in the hemihydrate, and increases in importance going from nano-celestine to celestine. In addition, the water peaks in the hemihydrate are also not visible in solution, and the v_4 vibration peaks are of limited use due to the bulk water masking their signal and causing a low signal-to-noise ratio, even after subtracting the water background (Fig. S2). Consequently, we selected the v_3 vibration to track the *in situ* evolution of the $SrSO_4$–H_2O system.

Raman spectra were also collected *in situ* during $SrSO_4$ precipitation (Figure S3). These experiments focused on the v_1 vibration (S=O symmetric stretch), as it gives the strongest Raman signal of the sulfate vibrations (Figure 4c). We observed an absorbance maximum at 1002 cm^{-1} for celestine and 1006 cm^{-1} for hemihydrate, while dissolved SO_4^{2-} in solution has a maximum at 982 cm^{-1}. This difference in maximum absorption energy was used to track the evolution of hemihydrate in the system.

The analytical spectroscopic and electron microscopy tools described above allow for the temporal evolution of the solid phases forming in the SrSO4–H2O system to be followed, but each technique comes with its own set of limitations. Specifically, electron microscopy (SEM and TEM) reveals the morphology, composition, and structure of the two crystalline phases but has not yet provided information on how these characteristics change with time. We are, however, currently undertaking studies

that are based on in situ environmental TEM (eTEM) to provide real-time data on the transformation mechanism at sub-nanometer resolution. PXRD provides a substantial amount of structural information, but at the cost of extremely limited time resolution. Raman allows tracking of free sulfate, hemihydrate, and celestine, but the small difference between absorption peaks in the hemihydrate and celestine phases would require complex peak deconvolution algorithms and very well-refined data, thus limiting its application in mixed systems. In comparison, FTIR can better differentiate the phases but loses the ability to track sulfate ions. Consequently, no single technique can reveal the full precipitation pathway. For this reason, the second part of this study details the use of a combination of the aforementioned methods to elucidate the transient nucleation process occurring in the strontium sulfate system.

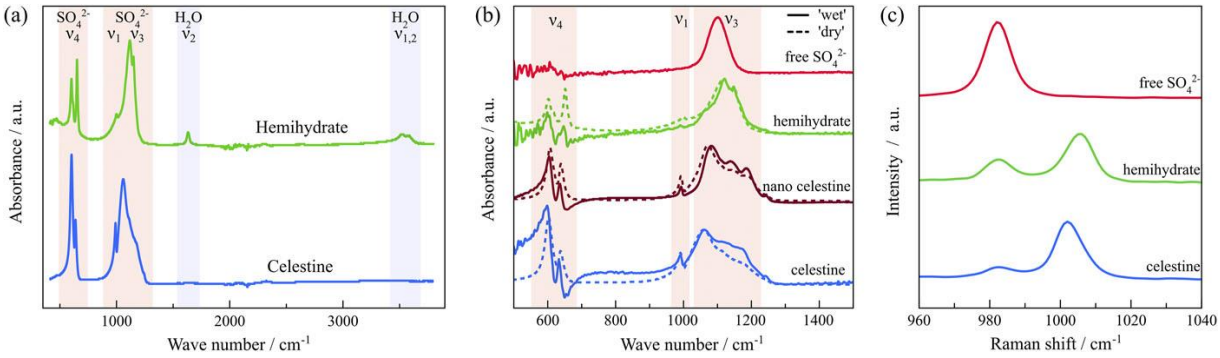

Figure 4: *FTIR-ATR and Raman spectra of strontium sulfate solutions, hemihydrate, and celestine. (a) FTIR spectrum of SO_4^{2-} in celestine and the hemihydrate, including the v_3 (asymmetric stretch, around 1100 cm^{-1}) and v_4 (asymmetric bend, ~600 cm^{-1}) vibrational modes. Note the vibrational water peaks: the v_2 (bend) peak at 1632 $cm^{-1}$and the v_1 and v_3 stretching peaks between 3500 and 3600 cm^{-1} in the hemihydrate. (b) A detailed view of v_3 and v_4 vibrations of SO_4^{2-} in solution and for "wet" (solid line) and "dry" (dotted line) solid phases. There is a distinct difference in v_3 peak location for hemihydrate and celestine in both cases, as well as a significant increase in the secondary peak at 992 cm^{-1} going from hemihydrate to nano-celestine to celestine. Additionally, there is a red shift in the peak for celestine as the particles grow from nanosized (light blue solid line) to bulk crystals (dark blue solid line). (c)* In situ *Raman spectra of the S=O stretch peak of free sulfate ions in solution, hemihydrate, and celestine, which was used as a probe for the transformation process.*

3.3. Transformation mechanism of the precursor phase to the final phase

When precipitation occurs at high supersaturations from an aqueous $SrSO_4$ solution in a well-mixed, large-volume (>1 ml) recipient, the hemihydrate will start to transform into celestine almost within ~5 s of observed nucleation. *In situ* FTIR of hemihydrate in the presence of an excess of deionized water was conducted to follow this transformation (Figure 5a, the graphic at the top shows the spectra collected at the start and the end of the reaction). In this type of experiment, the entire hemihydrate signal disappears within the first 2.5 min, which is accompanied by a corresponding increase in the celestine signal. Subsequently, over a period of ~30 min, a red shift of

one of the prominent celestine peaks occurs. As shown in Figure 4b, this decrease in vibrational energy occurs when celestine particles grow in size, indicating that a growth mechanism dominates after the first few minutes of celestine nucleation.

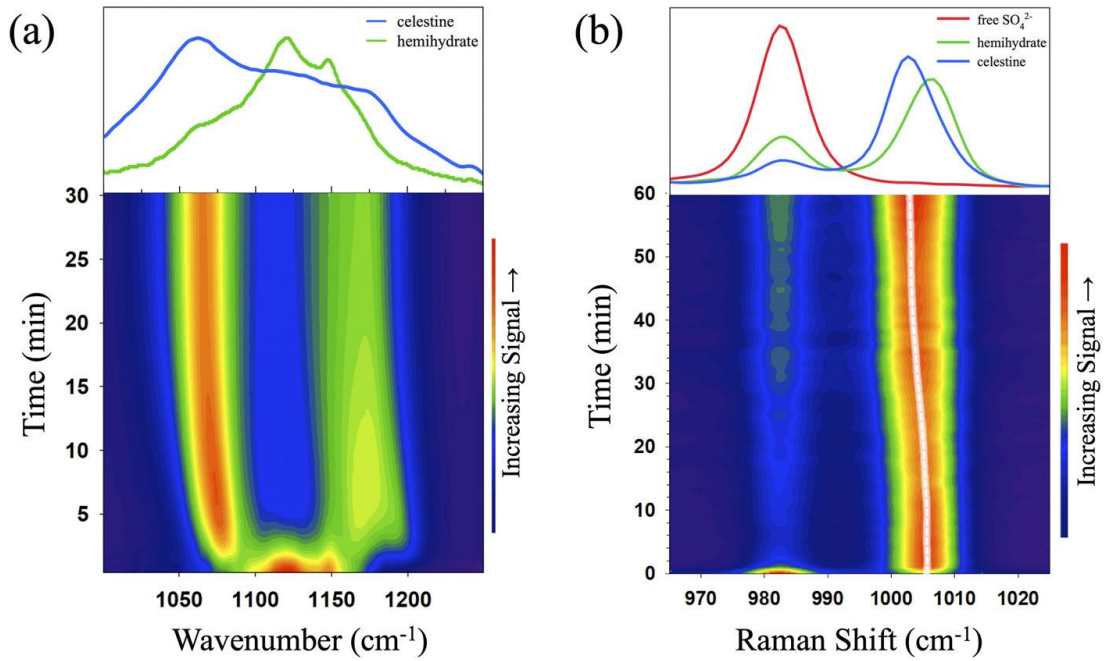

Figure 5: In situ *monitoring of the hemihydrate to celestine transformation. (a)* In situ *FTIR shows that the entire signal from the hemihydrate disappears after 5 min in the presence of excess water, and after 30 min a red shift in the strongest peak for celestine is noticeable, corresponding to the effect of particle growth on the IR signal. The top graphic displays spectra collected at the start and end of the reaction. (b) The top of the figure shows the characteristic Raman absorbance of the S=O symmetric stretch (v_1) in the $SrSO_4$–H_2O system as taken from an* in situ *experiment. Free ions in solution have a peak at 982 cm^{-1}, hemihydrate at 1006 cm^{-1} and celestine at 1002 cm^{-1}. All curves were normalized to the total peak area, including both solid and free ion peaks. The lower part of the figures reveals the temporal evolution of the system, including the formation and decomposition of the hemihydrate phase. The S=O stretch of the hemihydrate appears first at 1006 cm^{-1} (green curve top graphic). As the transformation (dashed white dotted line) to celestine progresses, the peak shifts toward 1002 cm^{-1}, which is accompanied by an increase in the free sulfate signal at 982 cm^{-1}. This is an indication that the transformation is accompanied by the dissolution of the hemihydrate. The curve for celestine (blue curve, top graphic) was taken several hours after the experiment to allow for crystal growth.*

The hemihydrate Raman spectrum shown at the top of Figure 5b (red curve) corresponds to the maximum concentration of hemihydrate measured at any point during the experiment. The corresponding free sulfate peak is substantially larger than the free sulfate peak for celestine after five hours (blue curve), indicating a higher solubility for hemihydrate than celestine. Based on the area under the peak corresponding to free sulfate, we find that the lowest sulfate concentration reached in the presence of hemihydrate is ~10.3 ± 0.6 mM—this concentration represents an upper bound on the hemihydrate solubility in a 100 mM NaCl background solution and a lower bound on the concentration of $SrSO_4$ at which hemihydrate can precipitate. This corresponds well with the ~9–10 mM limit estimated from the induction time

measurements (Figure 1a). In addition, the progress of the transformation is further characterized by a peak shift from 1004 cm^{-1} (hemihydrate) to 1002 cm^{-1} (celestine) during *in situ* Raman measurements (Figure 5b).

Measurement of free Sr^{2+} ions, using an ISE probe, during direct mixing reactions (i.e., adding $SrCl_2$ to Na_2SO_4 or vice versa), revealed that after the initial consumption of Sr^2 (due to the formation of the intermediate phase), a significant increase in the concentration of Sr^{2+} indicates the onset of the phase transformation process (Figure 6, blue curve). In conjunction with the ISE probe, an optical probe monitored the presence of suspended particles as a function of the solution transmittance (Figure 6, red curve). When adding $SrCl_2$ to Na_2SO_4 within one minute of mixing, the transmittance signal drops to zero due to the formation of a gel-like phase. The early stage (<20 min) is marked by an increase in the Sr^{2+} signal (when Na_2SO_4 is added to $SrCl_2$, the Sr^{2+} signal initially decreases, inset Figure 6), followed by the attainment of a plateau that remains stable for ~30 min. This behavior is interpreted to correspond to the removal of Sr due to the formation of the hemihydrate phase. After ~15 min, strontium ions are released back into solution (shown by the increased signal of the ISE probe, blue curve), indicating dissolution of the metastable hemihydrate. Almost simultaneously, the transmittance signal sharply increases, corresponding to the removal of the hemihydrate gel. Finally, the free Sr^{2+} ion concentration starts to decrease again due to the bulk formation of celestine, which concomitantly results in a rapid decrease in transmittance (red curve in Figure 6). The lower plateau in the Sr^{2+} signal at the end of the experiment points again to a lower solubility of celestine with respect to the hemihydrate. *In situ* Raman corroborates these findings, as it shows a similar increase in free SO_4^{2-} ions during the initial stages of the transformation reaction and a final decrease in free SO_4^{2-} ions at the end of the reaction (Figure 4b).

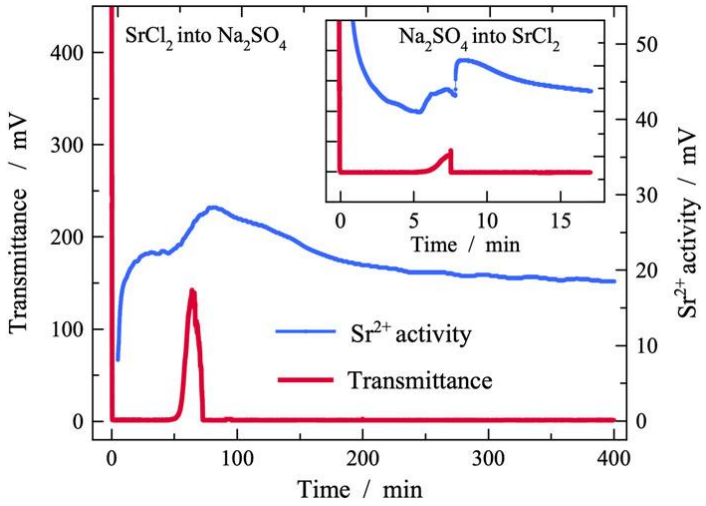

Figure 6: *The formation of $SrSO_4 \cdot 1/2H_2O$ and its subsequent transformation into celestine as monitored by a transmittance probe (red curve) and an ion selective electrode (blue curve). When a stock solution of $SrCl_2$ is titrated rapidly into a gently stirred (200 rpm) stock solution of Na_2SO_4, the capacity of the optical probe to observe changes in the solution is exceeded after the first 30 s of the precipitation reaction. The ISE indicates a plateau in the free ion concentration after the first ~25 min of reaction (indicating hemihydrate stabilization), followed by a subsequent increase in the Sr^{2+} concentration (showing dissolution of this phase). The rapid increase/decrease in the transmittance signal, coincident with the increase in ISE signal, indicates that the dissolution of the hemihydrate and nearly concomitant reprecipitation of celestine. The inset shows the results of a similar experiment conducted at a higher stirring rate (500 rpm); moreover, in this case, Na_2SO_4 was added to a $SrCl_2$ solution. The ISE signal drops until reaching a plateau (~5 min), corresponding to hemihydrate stabilization. The increased hydrodynamics speeds up the transformation process, with the increase in the ISE signal and transmittance occurring after ~7.5 min. Due to the very dense solution in these experiments, the ISE signal displays a significant amount of noise, but the overall trends are reproducible.*

In situ optical microscopy monitoring of an equimolar counterdiffusion experiment of $SrCl_2$ and Na_2SO_4 solutions in a glass capillary (Figure 7) further corroborates the idea of a dissolution-reprecipitation reaction as the main mechanism driving the transformation of the intermediate hemihydrate phase to the final celestine phase. A precipitation front formed rapidly (<30 s) at the interface between the diffusing solutions. Needle-like crystals, similar to those imaged by electron microscopy (Figure 3), are the first macroscopic solid phases to be observed after the onset of nucleation during counterdiffusion. After several minutes, the first formed needles of presumably hemihydrate commence to dissolve and concomitantly particles with a morphology resembling that of celestine start to appear randomly in the central section of the capillary (i.e., at the scale of this experiment, it appears that nucleation of celestine particles is not spatially coupled to hemihydrate needles). These macroscopic results thus also support the idea that the Sr^{2+} ions released by the dissolution of the hemihydrate phase participate in the precipitation of the final phase, celestine. This corroborates the Raman and potentiometric data obtained during direct mixing

experiments. It is noteworthy that the dissolution of the hemihydrate phase is first observed within the solution environment rich in Sr^{2+} and Cl^- ions—it is possible that this spatial heterogeneity is due to a stabilizing effect of Na^+ or SO_4^{2-} ions on the hemihydrate[52]. It is also important to note that under these diffusive conditions, the full transformation of hemihydrate to celestine took ~5 h. This is in stark contrast to the much shorter transformation times noted in the other experiments (see Table 1).

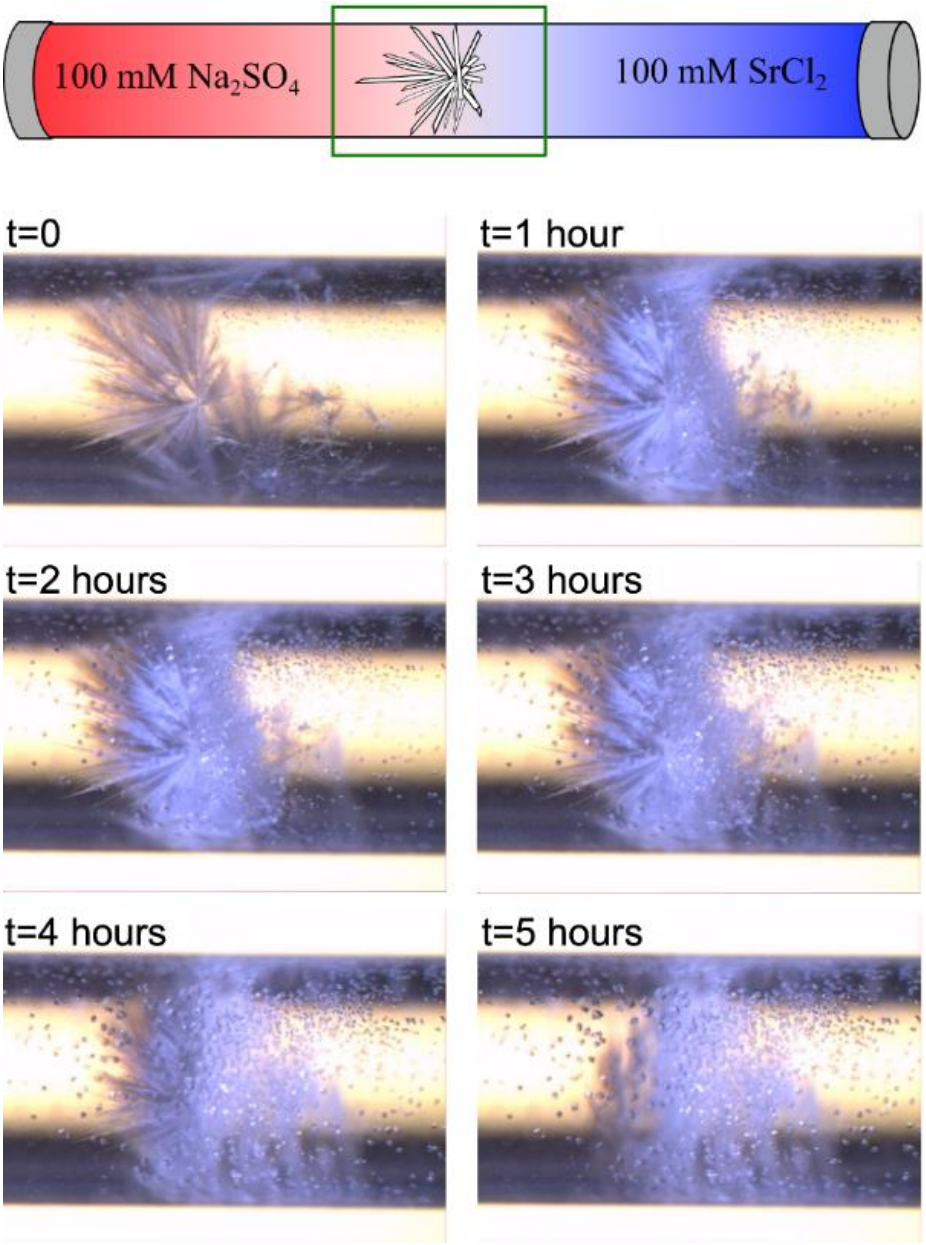

Figure 7: *Counter-diffusion induced $SrSO_4$ precipitation. The uppermost schematic shows the experimental setup, including the micrograph field of view indicated by the green square. In the panels below, optical micrographs show the temporal evolution of the hemihydrate–celestine transition in a glass capillary. The first observation was achieved ~2 min after solution injection due to experimental setup time. Initially, the hemihydrate fibers appear to grow radially from nucleation points, after which the fibers exposed to $SrCl_2$ (right side of the capillary) dissolve within the first hour. As the experiment proceeds, the fibers start to preferentially dissolve within the capillary region enriched in $SrCl_2$ solution.*

The fibers progressively dissolve via a reaction front that progresses from right to left, and concomitantly, the celestine crystals located on the surface of the glass grow in size.

The above-described experiments highlight the importance of the local physicochemical environment, which appears to control the kinetics of the transformation of hemihydrate to celestine. The counterdiffusion experiment indicates that the nature of the ions surrounding the hemihydrate affects the dissolution rate of the metastable phase (i.e., faster transformation on the $SrCl_2$ side). Moreover, in experiments in an ion-free environment (i.e., hemihydrate in excess deionized water, FTIR), the transformation occurs more rapidly than in a solution with a moderate ionic strength (100 mM NaCl). These observations are consistent with a previous study, which reported that the growth and dissolution rates of $BaSO_4$ and $SrSO_4$ can be highly dependent on the ionic strength and composition of the background electrolyte solution, an effect beyond that expected from the change in the activity coefficient of the constituent ions[53]. Finally, when comparing two of the direct mixing experiments (*in situ* Raman and potentiometric ISE measurements), there appears to be a difference in the kinetics, despite the fact that the only difference in reaction conditions being the method of agitation. In the Raman experiment, a double propeller mixer was used, while for the ISE experiment, a magnetic stir bar at the bottom of a beaker served to agitate the solution. This indicates that hydrodynamic considerations, and specifically the fluid dynamic shear rate, are another physicochemical factor influencing the reaction rate.

Table 1: *Summary of transformation times from various experiments showing that the kinetics of the reaction depend heavily on physicochemical conditions present during the experiment.*

Experiment	Transformation time	Unique Conditions
FTIR	3 minutes	No background ions
Raman	60 minutes	Double blade mixing (50 rpm)
Direct mixing	100 minutes	Stir bar mixing (50 rpm)
Diffusive mixing	5 hours	Diffusion conditions
benchtop	< 1 week	No bulk solution

A remaining question regarding the dissolution-reprecipitation transformation mechanism stems from the observation that the hemihydrate phase also transformed

under “dry” (i.e., when separated from the bulk liquid phase) benchtop conditions. Samples that were initially >95% pure hemihydrate were found to have transformed to celestine after as little as a week (and a maximum of two weeks) when stored in closed 50 ml plastic tubes at ambient conditions. The ambient relative humidity was estimated to have varied between 40% and 60% (~10.9 ± 2.2 g H_2O/m^3), based on bench top hygrometric measurements. In order to quantify the hemihydrate stability, time-resolved, semi-quantitative *in situ* PXRD (Figure 8) in controlled relative humidity environments (70%, 80%, and 90%) was used to track the kinetics of the transformation. The results show that the rate of the hemihydrate-to-celestine reaction increases as a function of the RH. It was determined that at 90% RH, the hemihydrate has fully transformed to celestine in ~1d, while at 70%, approximately half of the hemihydrate has been transformed in 2.5 days. Hence, the RH-transformation experiments further support the notion that the transformation reaction is solution-mediated and, in this particular case, driven by dissolution within a surface-adsorbed water film. The presence of adsorbed water on “dry” hemihydrate samples was confirmed by TGA measurements (Figure S4).

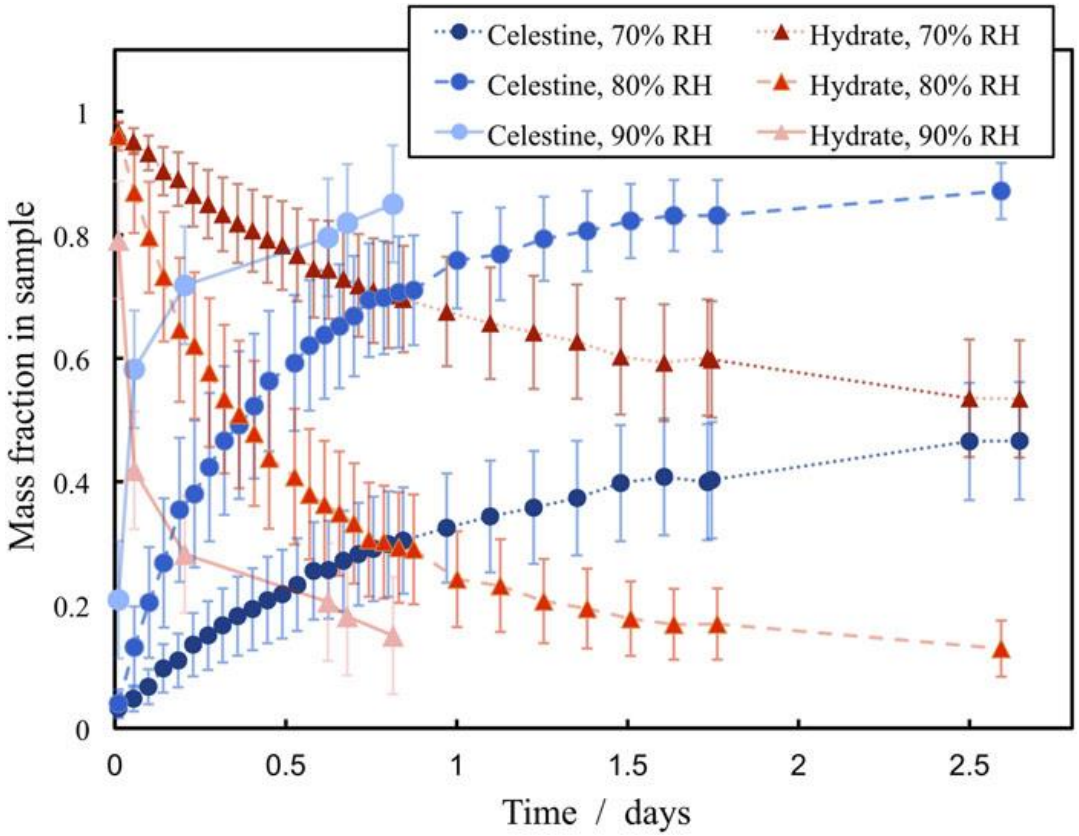

Figure 8: *Transformation kinetics as measured by PXRD under controlled relative humidities at 24 °C (100% RH = 21.8 g H_2O/m^3). Note that transformation rates increase with increasing humidity. Phase purity estimated by the RIR method using a Rietveld refinement of the system taken at the end of each experiment and considered a reference state.*

4. Concluding remarks

We used a suite of experimental and analytical techniques, including Raman, FTIR, and PXRD, SEM and TEM electron microscopies, and potentiometric probes, to measure the transition from dissolved ions to the final solid phase in the $SrSO_4$–H_2O system at ambient conditions. Our observations revealed that in solutions with a saturation index below ~1.5, the early stages of nucleation are driven by bound species, akin to the prenucleation cluster model, resulting in the direct formation of celestine ($SrSO_4$). At higher supersaturations, the onset of nucleation is dominated by the consumption of free ions instead of bound species. This change in nucleation mechanism is also coupled to the formation of an intermediate phase, hemihydrate ($SrSO_4 \cdot 1/2H_2O$), which eventually transforms into celestine, adhering to Ostwald's rule of stages. Importantly, the presence of a fluid appears to be crucial for this transformation process, even when present only as a fluid film due to ambient water vapor. This fluid-assisted transformation proceeds most likely via the dissolution of the metastable phase and the *de novo* crystallization of the final phase.

Multiple pathways likely exist for the dissolution-reprecipitation-mediated transformation process. Increased free-ion concentrations found during *in situ* Raman and potentiometry experiments suggest a process where the precursor hemihydrate is dissolved into a solution, creating a solution supersaturated with respect to celestine, allowing for a completely independent second nucleation event to occur. Hence, this mechanism can be viewed in terms of a classical thermodynamic-controlled process driven by chemical supersaturation in a bulk fluid. However, the phase transformation of solid hemihydrate under atmospheric conditions (benchtop and XRD) suggests a solid–fluid interfacial process may have been operative, such as coupled interfacial dissolution–reprecipitation (CIDR), as has been postulated to occur at a variety of physico-chemical conditions for minerals[54–57] and glasses[58–60]. We also observed that the kinetics of these dissolution–reprecipitation processes strongly depend on the local physicochemical and hydrodynamic environment—in particular, the ions present, the ionic strength, and the shear rate of agitated solutions. All of these factors will influence the microchemical environment(s) associated with each fiber of the metastable phase, in particular the nature of the very thin fluid film that is known to be present at fluid–solid interfaces. This has the potential to result in very different hemihydrate behaviors in real-world environments, such as those of porous media.

Finally, the intermediate hemihydrate phase observed during the precipitation of celestine is similar in structure and metastable nature to bassanite ($CaSO_4 \cdot 1/2H_2O$), a possible precursor of gypsum ($CaSO_4 \cdot 2H_2O$)—despite the calcium sulfate system being different in that the final phase gains water rather than losing it. However, not all alkaline earth metal sulfate systems exhibit a known hydrated intermediate phase; for example, only an anhydrous crystalline structure has been reported for $BaSO_4$. Thus, the nature and properties of the sulfate cation (e.g., Ca^{2+}, Sr^{2+}, Ba^{2+}, etc.) drive the stability/persistence of a (hydrated) intermediate phase and significantly influence the nucleation pathway. This underlines that although Ostwald's rule of stages is a common process, it is not a prerequisite for solid mineral formation—even in systems where it can occur. Therefore, the continuous development of our understanding of the role of the cation and its interplay with other physicochemical parameters could provide further insight on key aspects controlling the formation pathway of minerals. Overall, our results shed renewed light on the Ostwald rule of stages, and the data in these experiments suggests that the question of whether a metastable intermediate phase is formed is controlled in the prenucleation stage. Moreover, the transformation of the metastable into the final phase can follow different pathways depending on the local physico-chemical environment.

Author Contributions:

A.R. Lauer contributed all experimental work, writing, and figures except as noted for other authors.

R. Hellmann provided supervision and funding for the HRTEM experiments, revisions of sections regarding TEM, and context for conclusions drawn from those experiments.

G. Montes-Hernandez provided the custom *in situ* raman apparatus as well as counsels during the raman experiments and analysis of raman data.

N. Findling operated the XRD experiments and developed the protocol for atmospheric vapor pressure control needed for the *in situ* XRD.

W.L. Ling provided cryo-TEM images of samples provided by A.E.S. Van Driessche

T. Epicier operated the HRTEM with A.R. Lauer and R. Hellmann using samples provided by A.R. Lauer and helped revise the experimental protocol for that section.

A. Fernandez-Martinez provided supervision for A.R. Lauer as well as discussion and editing during the manuscript preparation.

A.E.S. Van Driessche contributed supervision of experiments (except as mentioned for other authors) as well as being the main contributor to revisions of the manuscript and discussion of results.

References

1. A. E. S. Van Driessche, M. Kellermeier, L. G. Benning, and D. Gebauer, New Perspectives on Mineral Nucleation and Growth: From Solution Precursors to Solid Materials (Springer International Publishing, Cham, 2017).
2. E. Beniash, J. Aizenberg, L. Addadi, and S. Weiner, “Amorphous calcium carbonate transforms into calcite during sea urchin larval spicule growth,” Proc. R. Soc. London, Ser. B 264(1380), 461–465 (1997).
3. L. Addadi, S. Raz, and S. Weiner, “Taking advantage of disorder: Amorphous calcium carbonate and its roles in biomineralization,” Adv. Mater. 15, 959–970 (2003).
4. W. Sun and G. Ceder, “Induction time of a polymorphic transformation,” CrystEngComm 19(31), 4576–4585 (2017).
5. A. E. S. Van Driessche, L. G. Benning, J. D. Rodriguez-Blanco, M. Ossorio, P. Bots, and J. M. García-Ruiz, “The role and implications of bassanite as a stable precursor phase to gypsum precipitation,” Science 336(6077), 69–72 (2012).
6. S. Weiner, I. Sagi, and L. Addadi, “Structural biology. Choosing the crystallization path less traveled,” Science 309(5737), 1027–1028 (2005).
7. D. Gebauer, A. Völkel, and H. Cölfen, “Stable prenucleation calcium carbonate clusters,” Science 322, 1819–1822 (2008).
8. T. M. Stawski, A. E. S. Van Driessche, M. Ossorio, J. Diego Rodriguez-Blanco, R. Besselink, and L. G. Benning, “Formation of calcium sulfate through the aggregation of sub-3 nanometre primary species,” Nat. Commun. 7(1), 11177 (2016).
9. T. M. Stawski, R. Besselink, K. Chatzipanagis, J. Hövelmann, L. G. Benning, and A. E. S. Van Driessche, “Nucleation pathway of calcium sulfate hemihydrate (bassanite) from solution: Implications for calcium sulfates on mars,” J. Phys. Chem. C 124(15), 8411–8422 (2020).
10. D. C. Gary, M. W. Terban, S. J. L. Billinge, and B. M. Cossairt, “Two-step nucleation and growth of InP quantum dots via magic-sized cluster intermediates,” Chem. Mater. 27(4), 1432–1441 (2015).
11. A. V. Radha, T. Z. Forbes, C. E. Killian, P. U. P. A. Gilbert, and A. Navrotsky, “Transformation and crystallization energetics of synthetic and biogenic

amorphous calcium carbonate," Proc. Natl. Acad. Sci. U. S. A. 107(38), 16438–16443 (2010).

12. N. Krautwurst, L. Nicoleau, M. Dietzsch, I. Lieberwirth, C. Labbez, Fernandez-Martinez, A. E. S. Van Driessche, B. Barton, S. Leukel, and W. Tremel, "Two-step nucleation process of calcium silicate hydrate, the nanobrick of cement," Chem. Mater. 30(9), 2895–2904 (2018).
13. W. Ostwald, "Studien über die Bildung und Umwandlung fester Körper: Abhandlung: Übersättigung und Überkaltung," Int. J. Chem. Phys. 22U(1), 289–330 (2017).
14. A. G. Christy, "Sulfate minerals," in Encyclopedia of Earth Sciences Series (Springer, Netherlands, 2018), pp. 1392–1394.
15. A. E. S. Van Driessche, T. M. Stawski, and M. Kellermeier, "Calcium sulfate precipitation pathways in natural and engineered environments," in Chemical Geology (Elsevier B.V., 2019), p. 119274.
16. T. M. Stawski, A. E. S. Van Driessche, R. Besselink, E. H. Byrne, P. Raiteri, J. D. Gale, and L. G. Benning, "The structure of CaSO4 nanorods: The precursor of gypsum," J. Phys. Chem. C 123(37), 23151–23158 (2019).
17. G. Hoareau, C. Monnin, and F. Odonne, "A study of celestine equilibrium in marine sediments using the entire ODP/IODP porewater data base," Geochim. Cosmochim. Acta 74(14), 3925 (2010).
18. H. M. Ezuber, "Prediction of strontium sulfate scale formation in oilfield environment," J. ASTM Int. 4(6), 1–11 (2007).
19. K. D. Carrell, "The occurrence, prevention and treatment of sulphate scale in shell expro," paper presented at the SPE Offshore Europe, Aberdeen, United Kingdom, September 1987.
20. J. Ober, Minerals Yearbook (U.S. Geological Survey, 2020).
21. R. E. Bernstein, R. H. Byrne, P. R. Betzer, and A. M. Greco, "Morphologies and transformations of celestine in seawater: The role of acantharians in strontium and barium Geochemistry," Geochim. Cosmochim. Acta 56(8), 3273 (1992).
22. A. G. Walton, "Nucleation and the interfacial tension of sparingly soluble salts," Microchim. Acta 51(3), 422 (1963).
23. B. V. Enüstün and J. Turkevich, "Solubility of fine particles of strontium sulfate," J. Am. Chem. Soc. 82(17), 4502 (1960).

24. D. H. Klein and J. A. Driy, “Heterogeneous and homogeneous nucleation of strontium sulphate,” Talanta 13(2), 289 (1966).
25. J. R. Campbell and G. H. Nancollas, “The crystallization and dissolution of strontium sulfate in aqueous solution,” J. Phys. Chem. 73(6), 1735 (1969).
26. J. N. Bracco, Y. Gooijer, and S. R. Higgins, “Growth kinetics of step edges on celestine (001) surfaces as a function of temperature, saturation state, ionic strength, and aqueous strontium: Sulfate ratio: An in-situ atomic force microscopy study,” Geochim. Cosmochim. Acta 175, 222 (2016).
27. S. He, J. E. Oddo, and M. B. Tomson, “The nucleation kinetics of strontium sulfate in NaCl solutions up to 6 m and 90°C with or without inhibitors,” J. Colloid Interface Sci. 174(2), 327 (1995).
28. I. X. Malollari, P. G. Klepetsanis, and P. G. Koutsoukos, “Precipitation of strontium sulfate in aqueous solutions at 25 ○C,” J. Cryst. Growth 155(3–4), 240 (1995).
29. A. E. Nielsen, “Nucleation and growth of crystals at high supersaturation,” Krist. Tech. 4(1), 17 (1969).
30. A. Packter, “The precipitation of sparingly soluble alkaline-earth metal and lead salts: Nucleation and growth orders during the induction period,” J. Chem. Soc. A 1968, 859.
31. M. Slovenc and B. Težak, “Kinetics and precipitation mechanism of sparingly soluble alkaline earth sulfates,” Colloid Polym. Sci. 254(10), 900 (1976).
32. M. Miura, H. Naono, and M. Hara, “The effect of the pH value on the crystallization of strontium sulfate in the presence of triphosphate,” Bull. Chem. Soc. Jpn. 39(2), 1104 (1966).
33. T. Mikami, T. Sakuma, and I. Hirasawa, “CSD-controlled reactive crystallization of SrSO4 in the presence of polyethylenimine,” Chem. Eng. Res. Des. 88(9), 1200 (2010).
34. H. Naono, “The effect of triphosphate on the crystallization of strontium sulfate,” Bull. Chem. Soc. Jpn. 40(5), 1104 (1967).
35. S. Sarig and F. Tartakovsky, “Inhibition of strontium sulfate precipitation by soluble polymers,” Isr. J. Chem. 12(5), 905 (1974).
36. B. Lambert and W. Hume-Rothery, “CCCXLVII.—Studies of precipitated solids. Part I. Strontium sulphate,” J. Chem. Soc. 129, 2637–2648 (1926).

37. S. Takahashi, M. Seki, and K. Setoyama, “Formation of SrSO4·1/2H2O in an SrSO4–HO system and its solid solution in a CaSO4–SrSO4–H2O system,” Bull. Chem. Soc. Jpn. 66(8), 2219–2224 (1993).
38. C. M. Pina and Á. Tamayo, “Crystallisation of strontium sulphates from Si-bearing aqueous solutions,” Geochim. Cosmochim. Acta 92, 220 (2012).
39. G. Montes-Hernandez and F. Renard, “Time-resolved in situ Raman spectroscopy of the nucleation and growth of siderite, magnesite, and calcite and their precursors,” Cryst. Growth Des. 16(12), 7218–7230 (2016).
40. J. Leroux, D. H. Lennox, and K. Kay, “Direct quantitative x-ray analysis: By diffraction-absorption technique,” Anal. Chem. 25(5), 740–743 (1953).
41. X. Zhou, D. Liu, H. Bu, L. Deng, H. Liu, P. Yuan, P. Du, and H. Song, “XRD-based quantitative analysis of clay minerals using reference intensity ratios, mineral intensity factors, Rietveld, and full pattern summation methods: A critical review,” Solid Earth Sci. 3, 16 (2018).
42. A. R. Lauer, M. A. Durán-Olivencia, A. Fernandez-Martinez, and A. E. S. Van Driessche, “Multistep nucleation compatible with a single energy barrier: Catching the non-classical culprit,” Faraday Discuss. 235, 95–108 (2022).
43. W. J. E. M. Habraken, J. Tao, L. J. Brylka, H. Friedrich, L. Bertinetti, A. S. Schenk, Verch, V. Dmitrovic, P. H. Bomans, P. M. Frederik, J. Laven, P. Van Der Schoot, Aichmayer, G. De With, J. J. DeYoreo, and N. A. J. M. Sommerdijk, “Ion-association complexes unite classical and non-classical theories for the biomimetic nucleation of calcium phosphate,” Nat. Commun. 4, 1507 (2013).
44. N. A. Garcia, R. I. Malini, C. L. Freeman, R. Demichelis, P. Raiteri, N. A. J. M. Sommerdijk, J. H. Harding, and J. D. Gale, “Simulation of calcium phosphate prenucleation clusters in aqueous solution: Association beyond ion pairing,” Cryst. Growth Des. 19(11), 6422–6430 (2019).
45. J. Scheck, J. K. Berg, M. Drechsler, A. Kempter, A. Van Driessche, H. Cölfen, D. Gebauer, and M. Kellermeier, “New insights into the nucleation of magnesium hydroxide and the influence of poly(acrylic acid) during the early stages of Mg(OH)2 crystallisation,” CrystEngComm 24, 7718 (2022).
46. A. Navrotsky, “Energetic clues to pathways to biomineralization: Precursors, clusters, and nanoparticles,” Proc. Natl. Acad. Sci. U. S. A. 101, 12096–12101 (2004).

47. F. C. Hawthorne and R. B. Ferguson, “Anhydrous sulphates I: Refinement of the crystal structure of celestine with and appendix on the structure of thenardite,” Can. Mineral. 13, 181–187 (1975).
48. M. Ossorio, A. E. S. Van Driessche, P. Pérez, and J. M. García-Ruiz, “The gypsum–anhydrite paradox revisited,” Chem. Geol. 386, 16–21 (2014).
49. U. Tritschler, A. E. S. Van Driessche, A. Kempter, M. Kellermeier, and H. Cölfen, “Controlling the selective formation of calcium sulfate polymorphs at room temperature,” Angew. Chem., Int. Ed. Engl. 54(13), 4083–4086 (2015).
50. M. D. Lane, “Mid-infrared emission spectroscopy of sulfate and sulfate-bearing minerals,” Am. Mineral. 92(1), 1–18 (2007).
51. B. Udvardi, I. J. Kovács, T. Fancsik, P. Kónya, M. Bátori, F. Stercel, G. Falus, and Z. Szalai, “Effects of particle size on the attenuated total reflection spectrum of minerals,” Appl. Spectrosc. 71(6), 1157–1168 (2017).
52. S. Reigl, A. E. S. Van Driessche, J. Mehringer, S. Koltzenburg, W. Kunz, and M. Kellermeier, “Revisiting the roles of salinity, temperature and water activity in phase selection during calcium sulfate precipitation,” CrystEngComm 24, 1529–1536 (2022).
53. P. Risthaus, D. Bosbach, U. Becker, and A. Putnis, “Barite scale formation and dissolution at high ionic strength studied with atomic force microscopy,” Colloids Surf., A 191, 201–214 (2001).
54. R. Hellmann, J.-M. Penisson, R. L. Hervig, J.-H. Thomassin, and M.-F. Abrioux, “An EFTEM/HRTEM high resolution study of the near surface of labradorite feldspar altered at acid pH: Evidence for interfacial dissolution-reprecipitation,” Phys. Chem. Miner. 30, 192–197 (2003).
55. A. Putnis and C. V. Putnis, “The mechanism of reequilibration of solids in the presence of a fluid phase,” J. Solid State Chem. 180, 1783–1786 (2007).
56. R. Hellmann, R. Wirth, D. Daval, J.-P. Barnes, J.-M. Penisson, D. Tisserand, T. Epicier, B. Florin, and R. L. Hervig, “Unifying natural and laboratory chemical weathering with interfacial dissolution-reprecipitation: A study based on the nanometer-scale chemistry of fluid-silicate interfaces,” Chem. Geol. 294–295, 203–216 (2012).
57. A. Zandanel, R. Hellmann, L. Truche, V. Roddatis, M. Mermoux, G. Choblet, and G. Tobie, “Geologically rapid aqueous mineral alteration at subfreezing temperatures in icy worlds,” Nat. Astron. 6, 554–559 (2022).

58. T. Geisler, A. Janssen, D. Scheiter et al., “Aqueous corrosion of borosilicate glass under acidic conditions: A new corrosion mechanism,” J. Non-Cryst. Solids 356, 1458–1465 (2010).
59. R. Hellmann, S. Cotte, E. Cadel, S. Malladi, L. S. Karlsson, S. Lozano-Perez, M. Cabié, and A. Seyeux, “Nanometre-scale evidence for interfacial dissolution-reprecipitation control of silicate glass dissolution,” Nat. Mater. 14, 307–311 (2015).
60. R. Hellmann, “Mechanisms of glass corrosion by aqueous solutions,” in Encyclopedia of Glass Science, Technology, History, and Culture, 1st ed., edited by P. Richet (The American Ceramic Society, John Wiley & Sons, Inc., Hoboken, NJ, 2021), Vol. I, pp. 647–662 (invited article that reviews glass dissolution mechanisms)

Supplementary Information

1. Interfacial Energies

The obtained induction time values were plotted as a function of supersaturation and fitted using the general nucleation rate equation provided by CNT[1]:

$$t_{ind} = \frac{1}{JV} = \frac{1}{Aexp\left(-\frac{B}{\ln^2 S}\right)}$$

Where *J* is the nucleation rate, *V* is the solution volume, *S* is the saturation rate, *W** the work to form a critical cluster, and *A* and *B* contain information about the kinetic properties of the forming solid phase. For the purpouse of fitting the experimental induction times as a function of supersaturation, Eq. 1 can be rewritten as follows:

$$\ln(t_{ind}) = \ln(A) + \frac{B}{\ln^2(S)}$$

The interfacial energy can then be obtained from the slope *B* when considering a spherical shape factor:

$$B = \frac{16\pi V_m^2 \gamma^3}{3k_b^3 T^3}$$

Where γ is the interfacial energy, V_m is the molecular volume, k_b is the Boltzmann constant and *T* the absolute temperature. Fig. S1 shows the data induction time, $\ln^{-2}(t_{ind})$, plotted as a function of the solution saturation state, $\ln^{-2} S$. In Table S1, the obtained effective interfacial energy for celestine in this study is compared to previously reported values. In the case of the hemihydrate phase, no solubility product, K_{sp}, has been reported to date, therefore we used an approximate value of ~$10^{-3.6}$ (which corresponds to a molecular solubility of 9mM in the presence of 100 mM NaCl) based on our UV-Vis and Raman measurements.

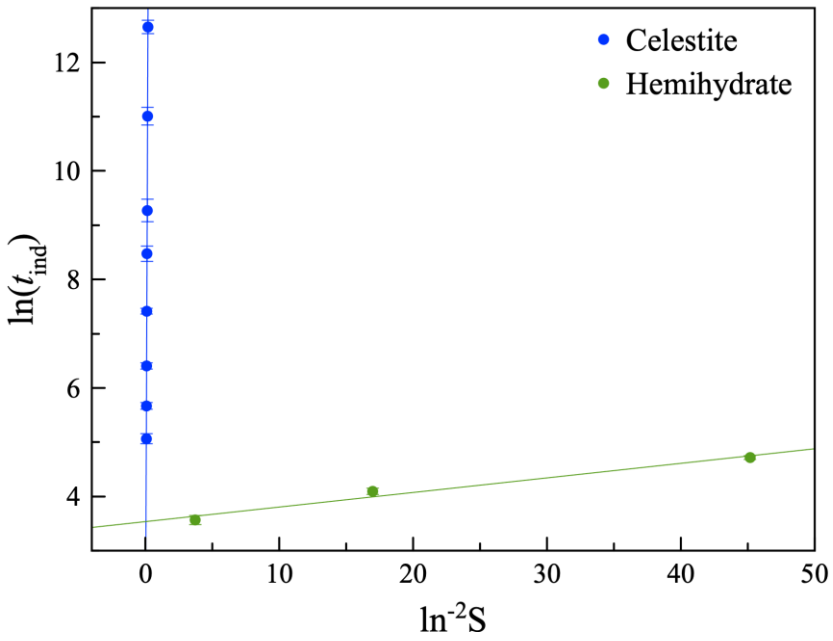

Figure S1: *Induction times of celestine and hemihydrate as a function of supersaturation. Data fitted using Eq. 2.*

Table S1: *Value of the effective interfacial energy, γ, of celestine and hemihydrate determined in this work compared to values reported for celestine in the literature obtained for homogeneous nucleation at ~25 ºC and background electrolyte concentrations <0.15 M.*

	γ (mJ.m^{-2})	Reference
$SrSO_4 \cdot 1/2H_2O$	~3	This work
$SrSO_4$	35	This work
$SrSO_4$	85	Nielsen[2]
$SrSO_4$	72	Garten and Head[3]
$SrSO_4$	87	Bennema and Sohnel[4]
$SrSO_4$	76	He et al.[5]
$SrSO_4$	50	Pina and Tamayo[6]
$SrSO_4$	23	Temgoua[7]

2. Hemihydrate Structure

Rietveld refinement of the hemihydrate structure to determine unit cell parameters was done using the Profex modeling software. The data, shown in Table S2, is in good agreement with previously published work[8].

Table S2: *calculated lattice spacings from Rietveld refinement of XRD data.*

d value (Å)	h	k	l	Intensity %
6.21287	1	0	0	55.5
5.61948	1	0	1	1.2
3.587	1	1	0	54.7
3.46104	1	1	1	2.2
3.10643	2	0	0	89
4.51996	1	0	2	17.6
3.02354	2	0	1	3.2
3.15031	1	1	2	9.9
2.34824	2	1	0	8.4
2.80947	2	0	2	2.2
2.31182	2	1	1	1.7
4.392	0	0	3	1.2
2.07096	3	0	0	3.4
3.58637	1	0	3	54.7
2.04584	3	0	1	4.9
2.21193	2	1	2	29.0
2.77818	1	1	3	1.5
1.7935	2	2	0	9.3
2.53617	2	0	3	1.2
1.97564	3	0	2	9.7
1.77711	2	2	1	2.1
1.72314	3	1	0	11.8
1.70859	3	1	1	2.0
2.07083	2	1	3	3.8
1.73052	2	2	2	5.3
2.91026	1	0	4	100
1.55322	4	0	0	2.1
1.66706	3	1	2	2.1

1.54254	4	0	1	1.4
1.87316	3	0	3	4.8
2.42619	1	1	4	11.8
2.25998	2	0	4	6.8
1.42533	3	2	0	1.5
1.51177	4	0	2	2.0
1.41706	3	2	1	1.4
1.6604	2	2	3	1.6
1.35576	4	1	0	5.7
1.6041	3	1	3	2.6
1.91211	2	1	4	36.6
1.34864	4	1	1	8.5
1.3931	3	2	2	2.5
1.75324	3	0	4	13.2
2.426	1	0	5	11.8
1.46434	4	0	3	1.1
1.32793	4	1	2	2.0
1.24257	5	0	0	1.8
1.23708	5	0	1	1.6
2.1237	1	1	5	1.6
1.57515	2	2	4	3.2
2.00954	2	0	5	3.9
1.52685	3	1	4	3.8
1.22104	5	0	2	1.6
1.29544	4	1	3	2.2
1.75317	2	1	5	13.2
1.40487	4	0	4	3.6

3. Infrared measurements

During infrared measurements a potentially useful inversion of peaks at ~600 cm^{-1} and ~645 cm^{-1} when comparing hydrate to Celestine is observed. However, in the presence of water, noise of order of magnitude of 1/3 the large peak height for the hydrate (when present) was observed. This results in a loss of the “true” peak (noise causes the relative maximum to shift); in addition, it is possible that particularly large noise fluctuations could result in a premature observation of the presence of celestine, especially if the relative water/solid mass ratio were to increase either during the experiment or under different experimental conditions in future works. Furthermore, the slight shift in peak location coincidental with increasing celestine particle size is both more difficult to observe and is a shift that includes the same peak location as hemihydrate (603 cm^{-1} for both hydrate and larger celestine particles, 608 cm^{-1} for small celestine particles)- this effect is also more difficult to observe when analyzing this vibration mode. In summary, the v_3 sulfate vibration mode is the more reliable and accurate choice for analyzing the hydrate to celestine transformation reaction.

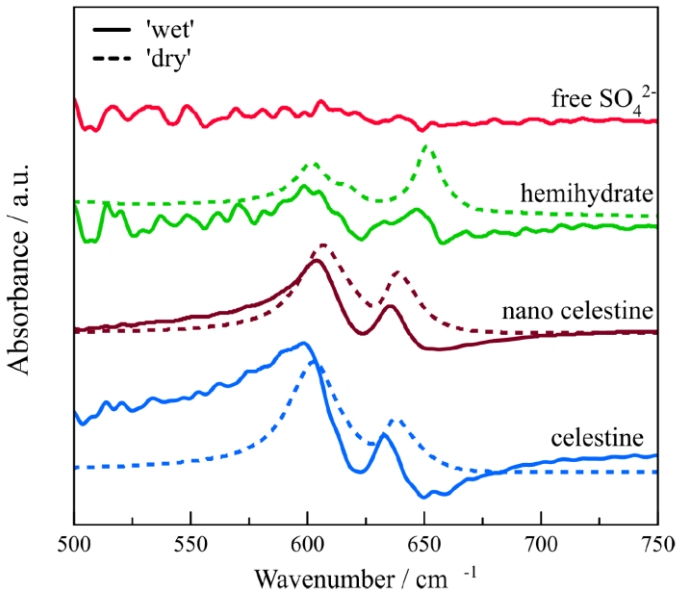

Figure S2: *The v_4 sulfate vibration during the IR experiments of free sulfate, hemihydrate, and celestine in the solution, suspension, and dry state.*

4. Vibration mode of in situ Raman measurements

The reasoning for focusing on a single vibration mode in the *in situ* Raman experiments is illustrated below. The experimental chamber featured a sapphire glass window trotecting the Raman probe in an aqueous environment. Outside of the peaks

attributable to the S=O symmetric stretch, all the observed peaks can be explained by either the sapphire window or water vibrations.

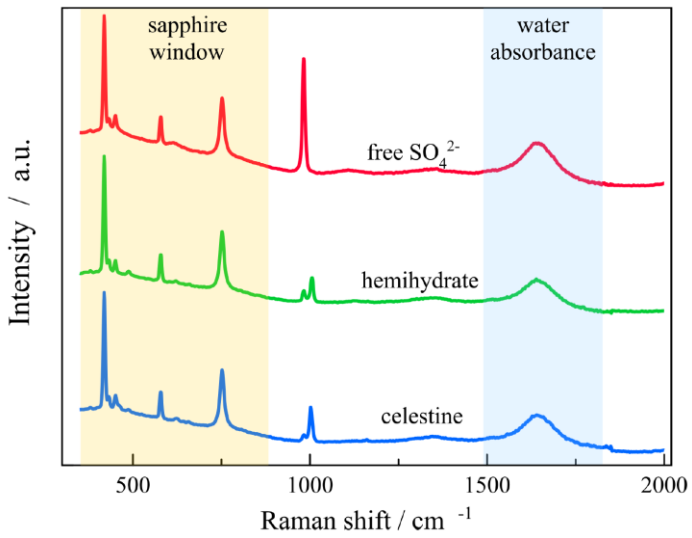

Figure S3: *In situ Raman spectra of hemihydrate, celestine, and free sulfate ions in solution. In all cases the peaks below 800 cm^{-1} are the same and can be attributed to the sapphire window protecting the Raman probe. The broad peak at ~1600 cm^{-1} is due to water. Thus, only the S=O stretch peak was used as a probe for the transformation process.*

5. Thermogravimetric analysis (TGA)

To determine the water content of the samples, TGA analysis were conducted using a Mettler Toledo TGA-DSC3+. Powdered samples were placed in an unsealed alumina crucible and scanned over a temperature range from 23 to 500 °C at 5 °C/min. Data were normalized and the total volatile mass in each sample was determined for comparison to the mass ofo structural water in the samples.

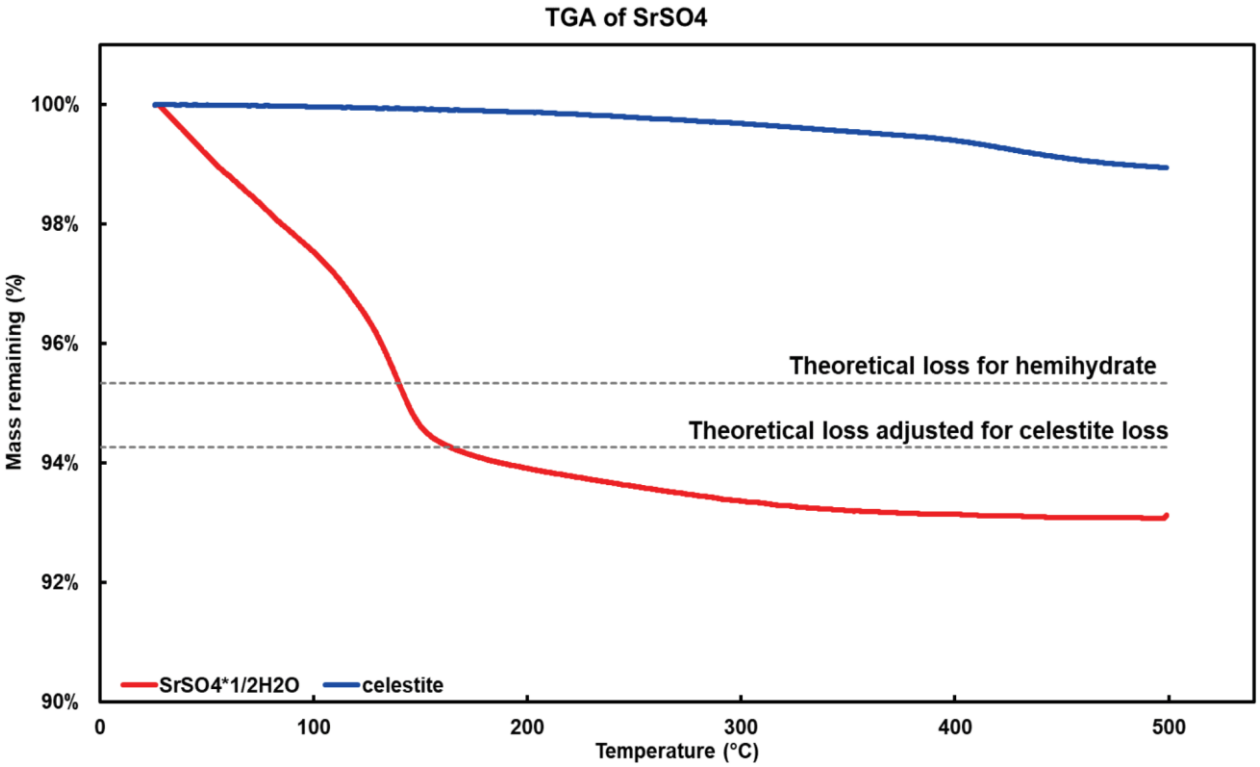

Figure S4: *Thermogravimetric analysis (TGA) of celestine and hemihydrate. The nominal mass fraction of water in the $SrSO_4 \cdot 1/2H_2O$ is 0.047. In the figure above, the top-most dotted grey line indicates the theoretical $SrSO_4$ mass and what would be expected to remain after the removal of structural water. The lower dotted grey line adjusts the expected final solid mass in a TGA of the hemihydrate based on the mass loss experienced due to adsorbed water from celestine under the same conditions. The additional mass loss below the lower grey line is indicative of the fact that hemihydrate carries more adsorbed water under atmospheric conditions, supporting the hypothesis that the hemihydrate to celestine transformation reaction is driven by adsorbed atmospheric water.*

Supplemental References

1. Kashchiev, D. Nucleation - Basic Theory With Applications, Butterworth-Heinemann, 2000.
2. Nielsen, A.E. Nucleation and Growth of Crystals at High Supersaturation. *Kristall und Technik* **1969**, 4, 17-38.
3. Garten, V.A.; Head R.B. Nucleation in salt solutions. *Faraday Transaction, Chem. Soc. London* **1973**, 69, 514-520.
4. Bennema P. and Sohnel O. Interfacial surface tension for crytsallisation and precipitation from aqueous solutions. *J. Cryst. Growth* **1990**, 102, 547-556.
5. He, S.L.; Oddo, J.E.; Tomson, M.B., The nucleation kinetics of strontium sulfate in NaCl solutions up to 6M and 90 ºC with or without inhibitors. *Journal of Colloid and Interface Science* **1995**, 174, 327-335.
6. Pina, C. M.; Tamayo, Á., Crystallisation of strontium sulphates from Si-bearing aqueous solutions. *Geochimica Et Cosmochimica Acta* **2012**, *92*, 220-232.
7. Temgoua, L.G. The fate of Eu(III)/Cm(III) during the nucleation and growth of celestite ($SrSO_4$) and strontianite ($SrCO_3$). PhD thesis, 2015. DOI: 10.5445/IR/1000053698.
8. Takahashi, S.; Seki, M.; Setoyama, K. Formation of $SrSO_4 \cdot 1/2H_2O$ in an $SrSO_4$ - H_2O System and Its Solid Solution in a $CaSO_4$ -$SrSO_4$ -H_2O System. *Bull. Chem. Soc. Jpn.* **1993**, 66, 2219-2224.

Chapter 3
The effects of confinement on the nucleation of strontium sulfate

Abstract

In this previously unpublished chapter, the effects of confinement on the nucleation of strontium sulfate are evaluated through a series of counterdiffusion experiments in silica hydrogel matrices. The experiments were monitored *in situ* using various x-ray scattering techniques (SAXS, WAXS) and absorption (XANES) to probe the reaction kinetics and structures of the early-formed particles. We confirm the results discussed in previous chapters by demonstrating that metastable strontium sulfate hemihydrate forms at high supersaturations within the pores. Furthermore, we provide additional evidence differentiating the nucleation pathways of celestine (two-step) and hemihydrate (single-step). The system generally follows the trend of nucleation occurring preferentially in the largest pores available. However, we note a counter-intuitive result: the induction time for nucleation decreased with decreasing average pore size. Additionally, we highlight the potential for surface functionality to drive kinetic changes during the nucleation process. Overall, the work included in this chapter lays the foundation for further studies of nucleation by demonstrating the capacity of the silica hydrogel counter-diffusion experiments to probe not just the effects of confinement but also the fundamental nature of nucleation in general.

1. Introduction

Fluids play a vital role in geological and geochemical processes, influencing metal dissolution, transport, and rock properties[1]. Understanding the fate of fluid contaminants in porous geological formations is also essential for preserving environmental safety in applications like waste disposal, freshwater contamination, industrial processes, and carbon storage[9]. To fully understand and evaluate fluid transport in geological systems, the manner and rate at which fluids can travel and carry solutes through pore spaces is of critical importance. Models of fluid transport in mesoporous systems have shown that flow and transport properties within a pore space are related by a power-law relationship to the volume fraction of pores present in a system – thus the precipitation of solids within the pore space has the potential to change the total porosity and therefore the transport properties of the system[10,11]. More recent studies have shown that at the low porosity limits and interfaces between fluid systems, the effects of precipitation can be even more pronounced by blocking principal transport conduits[12].

Furthermore, movement and mixing of fluids within these pore spaces[13], as well as factors like changing temperature[14] have the potential to drive the chemical reactions within the pores that can, in turn, influence the fluid transport within the system. Understanding and predicting these phenomena is necessary to many large-scale engineering situations that interact with their environments on a geologic scale. The mixing, and precipitation, of dissolved salts driven by hydraulic fracturing can lead to clogging or otherwise hinder the performance of drilling operations[15–17]. Mineral precipitation can also lead to reduced efficiency of membranes used in water desalination[18], or be used to remove contaminants from aquifers[19]. This contaminant scavenging, and other remediation technologies used for cleaning chemical spills in pore spaces can result in by-products that drive precipitation reactions as well[20], and, pressures generated by precipitation reactions in pore space can lead to large fractures in engineered structures[21–23].

Significantly, in the context of biomineralization processes, nature has seemingly mastered the manipulation of confinement to control the nucleation and growth of biominerals[24]. Particularly, confinement has been shown to influence the kinetic persistence of transient phases that appear during the nucleation process[25]. This phenomenon has been exploited by sea urchins, for example, to control the

polymorph selection between amorphous calcium carbonate and calcite during their shell formation[26,27]. Other mineral phases like aragonite are also known to be promoted by confined environments[28].

Finally, it is well established that the pore space can dramatically alter the thermodynamics and kinetics of the reactions themselves. For example, nanometer scale pores can dramatically alter the effective solubility of salts in water[29,30]. A general result of this effect is that when a range of pore sizes exist, nucleation occurs preferentially in the largest pores[31,32]. This is proposed to be driven by surface interactions (contact angle between pore walls and nucleates), as well as the radius of curvature present in the pore space[33]. A less frequently discussed implication of this is that in the event of highly favorable surface interactions, nucleation could theoretically be driven to preferentially occur in the smallest pores first (a detailed discussion of the formulation and theory can be found in the Results & Discussion section of this chapter). This has been shown to hold true for specific surface interactions during the nucleation of $CaCO_3$ in matrices with varied surface interactions[34].

While many minerals, such as $CaCO_3$, have been evaluated for their nucleation in pore spaces, little attention has been given to the class of sulfate minerals, and particularly strontium sulfate, in this field of study despite their abundance, and significance, in geologic and biologic environments (see Chapter 2 for elaboration). It's constituent ions, Sr^{2+} and SO_4^{2-}, are known to exist at or above solubility concentrations in pore waters around the world[35]. Furthermore, strontium sulfate is also an interesting system to observe the effect that nanopores can have on the different stages of a multistep nucleation process. This system has a known transient hydrated form, which has not yet been observed in nature[36,37]. This phase, referred to as strontium sulfate hemihydrate (or simply "hydrate" and "hemihydrate" in this context) grows in needle form[8,37] similar to calcium sulfate hemihydrate, a transient phase in the calcium sulfate system[38]. These needles generally have nano-scale diameters, making them an ideal candidate for stabilization in nano-scale pores, which has the possibility to reveal a natural mechanism for the formation and increased persistence of this elusive mineral phase. Additionally, evidence gathered during this PhD dissertation (c.f. Chapter 2) suggests that the nucleation of celestine, the thermodynamically stable solid phase of strontium sulfate, could form via a pathway of pre-nucleation species[39]. However, as with other mineral systems[40], the exact role of these prenucleation species is still debated. It is possible that retarded nucleation and simultaneous stabilization of

transient species driven by nanoporous environments could allow for the identification the role these precursor species have during nucleation.

To probe the $Sr\text{-}SO_4\text{-}H_2O$ mineral system and its behavior under confinement conditions, a series of counterdiffusion experiments were conducted in matrices of silica hydrogel with a variety of pore sizes. The evolution of the system, from the prenucleation regime to first nucleation, as well as the growth of the crystals, was monitored *in situ* using x-ray absorption (small-angle x-ray scattering, or SAXS, and wide-angle x-ray scattering, or WAXS) and x-ray near edge spectroscopy (XANES). These experiments together provide a holistic picture of the evolution of the pores space during the nucleation and growth stages as well as the phases that appear under varying conditions. The formation and persistence of the hemihydrate phase will be observed with respect to the known observation that nanopores stabilize transient phases in other mineral systems. We explore the effect of surface functionality and pore size on the reaction kinetics as well as the nucleate phase selection, and finally, we search for evidence of the presence of other, still undescribed prenucleation species.

2. Materials and methods

2.1 Synthesis of nanoporous silica gels

Counter-diffusion experiments were conducted using silica gel substrates of varying pore sizes contained in 1.2 mm diameter kapton capillaries (or 1 mm ID glass capillaries graciously provided by Vitrex medical). The capillaries were ca. 5 cm long and at their center a ca. 11 mm long silica hydrogel was synthesized inside the capillaries to create a water-permeable porous barrier between the two halves of the tube (Figure 1). Equimolar concentrations of strontium chloride ($SrCl_2$, 99% extra pure $SrCl_2 \cdot 6H_2O$, Acros Organics) and sodium sulfate (Na_2SO_4, 99% purity, Roth) were injected in opposite ends of the capillary, with care taken to ensure no air was trapped between the liquid solution and the gel substrate. The capillaries were sealed on both ends by dipping the capillary in molten paraffin wax (54-56°C). For all capillaries containing a gel substrate the injection sequence was Na_2SO_4, seal, $SrCl_2$, seal – the full procedure took approximately 45 seconds to complete. The reactions occurring in the porous silica gels were monitored using SAXS/WAXS and XANES.

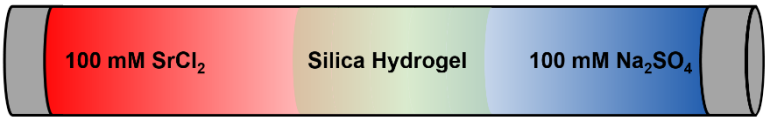

Figure 1: *Schematic of kapton capillary with gel substrate, $SrCl_2$ and $Na2SO_4$ solutions and paraffin wax seals.*

Gels were formed by mixing tetramethylorthosilicate (TMOS – Sigma Aldrich 341436) with deionized water in volumetrically controlled concentrations: 5, 10, 15, 20, and 25% TMOS. Variation of the gel concentration was used to control the average pore size of the gels (Table 1). Functionalized gels were created at the 10% volume fraction by mixing (3-Mercaptopropyl)trimethoxysilane (“thiol precursor”, Sigma Aldrich 95%) and 3-[Methoxy(polyethyleneoxy)propyl]trimethoxysilane, 6-9 (“methoxy precursor”, ABCR 90%, 6-9 PEG units) to create thiol and methoxy surface groups respectively. Figure 2 illustrates the structure of these precursors – the functionalized trimethoxysilane groups integrate into the silica network formed by the tetramethyoxysilate. No specific controls were made to orient the functional groups within the network.

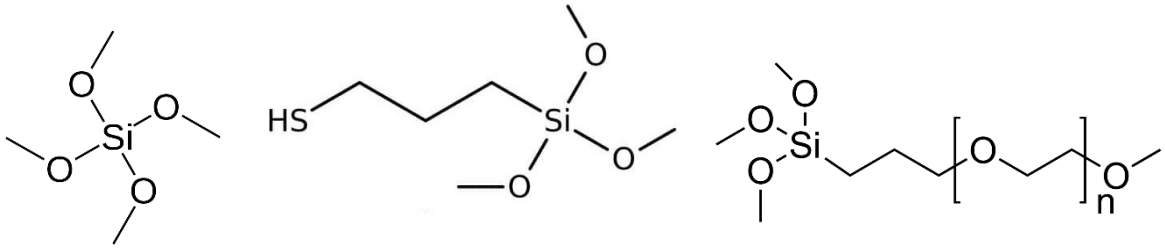

Figure 2: *Chemical structure of the silica gel precursor molecules. Left to right: TMOS, thiol precursor and methoxy precursor. "n" for the methoxy precursor ranges from 6 to 9 according to manufacturer specifications.*

These reagents were mixed at 10 and 25 volume percent of the reactive volume such that the final reaction mixture was either 1% thiol precursor (or methoxy precursor), 9% TMOS, and 90% water or 2.5% thiol precursor (or methoxy precursor), 7.5% TMOS and 90% water. The reactive solutions were prepared by measuring the volumes of each constitutive reactive component with a pipette into a 10 mL centrifuge tube with a total solution volume of 2 mL. Homogeneous mixing was ensured by using a pulsed ultrasonic mixing technique (Figure 3). The ultrasonic mixer was pulsed at a 30% intensity with a 0.2 seconds on/off cycle for 4 min. After one mixing sequence, the solution was evaluated for heterogeneity by eye. If phase separation could be observed, a second 4 min mixing sequence was applied. The mixing container was placed in an ice bath of EtOH, with an initial temperature of -40°C, in order to prevent evaporation of the reactive solution during mixing. Approximately 30 mL of EtOH was used in a 50 mL beaker – using too much EtOH resulted in freezing of the solution before mixing was completed.

Table 1: *Approximate pore sizes of TMOS based silica gels used in the experiments estimated from data from Cabane et al*[41].

TMOS v%	Approximate Mesh size (nm)
5	250
10	100
15	60
20	40
25	30

After mixing was completed, the reactive solution was immediately injected into the center of a capillary that had been sealed on one end by a small epoxy plug such that the length of the silica gel inside the capillary was ca. 1.1 cm. The epoxy plug ensured that the injected volume of reactive solution would remain in place when the capillary was stored vertically so that a series of capillaries could be prepared with the

same reactive solution. The injected capillaries were stored at room temperature in a sealed, upright centrifuge tube for curing. The entire sample preparation involving liquid TMOS (measuring, mixing, and curing) was performed in a fume hood to prevent exposure to toxic gases.

The silica gels were cured in the capillary approximately 7 days (minimum 4, maximum 10 days) before the experiment – with the lowest concentration gels generally requiring longer curing. A series of visual inspections assured the gel quality before the experiment. First, the bulk solution that was prepared during the mixing phase was checked to ensure that it was solid and the reaction was complete. When a bulk solution was fully cured, it was assumed that the solutions in the capillaries were similarly fully reacted. Then, the seal between the gel and the capillary had to be observed to ensure that no experimental solutions could pass between the gel and capillary. Gels were checked for large surface delamination, and to see if the gel moved easily during the initiation of the counterdiffusion experiments. Both were indications that sealing was not correct. Finally, the gels were also checked for internal flaws and fractures that could be seen by light reflections off the fracture surface. Gels used in experiments had no, or minimal, observable damage from these visual examinations.

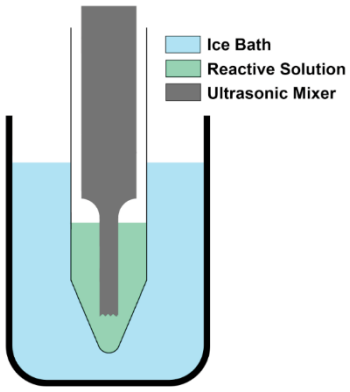

Figure 3: *Schematic of the ultrasonic mixing setup used for dissolving the TMOS into water.*

To prepare for the counter diffusion experiments, the epoxy plug was cut off the capillary, and the interior of the capillaries were exposed to air for a minimum of 60 minutes to allow for the EtOH, byproduct of the gelification reaction, to evaporate. During this time, the locations of the edges of the gel were marked on the capillary using a marker, or lead tape, to facilitate sample alignment in the x-ray beam. After injection of the $SrCl_2$ and Na_2SO_4 solutions and subsequent wax sealing of the capillaries, the Sr^{2+} and SO_4^{2-} counter-diffusion experiments could begin.

2.2 In situ monitoring of SrSO4 nucleation under confinement

All experiments were conducted placing the capillaries with the counterdiffusion experiments in a horizontal orientation to reduce possible effects from gravity. When possible, the samples were aligned horizontally using a system of cameras where the center of the beam on the image was determined for each experiment set before injection of the samples. When not possible, the samples were aligned using horizontal X-ray absorbance scans and the lead tape marks on the capillaries. Vertical alignment was always conducted using the vertical X-ray absorbance scans to find the center of the capillaries for each sample.

2.2.1 *Small-angle/wide-angle X-ray scattering (SAXS/WAXS)*

One series of SAXS/WAXS experiments were conducted at the BL11-NCD beamline of the ALBA synchrotron (Spain). These experiments utilized a 12.4 keV X-ray beam energy (λ = 1 Å), with a SAXS sample-detector distance of d_{SAXS1} = 6.7 m (calibrated using a silver behenate standard). This led to an accessible *q*-range from 0.0134 to 2.224 nm^{-1}. The WAXS sample-detector distance was d_{WAXS1} = 135.7 mm (calibrated using a Cr_2O_3 standard). During data treatment, an error was found in the WAXS calibration, and was re-computed by identifying known hydrate and celestine peaks manually for each experiment.

The second series of SAXS/WAXS experiments were conducted at the BM02 beamline of the European Synchrotron Radiation Facility (ESRF, France), using a 15.7 keV beam energy (λ = 0.79 Å), a SAXS sample-detector distance of d_{SAXS2} = 3.59 m, and WAXS detector distance of d_{WAXS2} = 130.5 mm. Detector distances were calibrated via a procedure of measuring AgBh, LaB_6 and Cr_2O_3 at different sample-detector distance to overcome limitations in sensor size at the long distances used.

For SAXS/WAXS experiments, 3 or 6 experiments (ALBA and ESRF respectively) were run simultaneously with 5 measuring points on each sample – with a spot size of approximately 500 µm and separated by 1 mm (distributed around the center of the gel, see Figure 3).

2.2.2 SAXS/WAXS data analysis

SAXS/WAXS data sets were treated using standard procedures for each beamline. The sample-detector distance was pre-calibrated before the experiment using known diffraction samples (depending on the availability at the beamlines), and

the samples were carefully arranged such that this distance did not change with each experiment. The scattered intensities of each pattern were corrected to the incident intensity of the beam and normalized to absolute scattering units using a water standard. This ensured valid comparisons between different time points of the same experiment.

First, data from gels prior to the counterdiffusion experiments were analyzed following the procedure for non-polydisperse polymer gel analysis outlined by Cabane et. al[41], as well as a more universal Guinier approximation analysis in the low q regime (to the extent possible with the available data). To begin, the fractal dimensionality of the gel was determined by analyzing the slope of the diffraction patterns for each gel in the high *q* regime (selected from where log(*I*) vs log(*q*) was linear). The intensity of the scattering in this regime follows the law $I(q) \propto q^{-D}$ where *D* is the fractal dimension of the polymer in question[42]. In this regime, the principal interest for evaluating the gels was the dimensionality, so fitting was done using Equation 1 where a_0 and a_1 cover the remaining scattering terms:

$$I(q) = a_0 + a_1 * q^{-D} \qquad \textit{Eq. 1}$$

From the result of this fitting (with a result of D~2) we applied a Guinier approximation to the low *q* regime following for lattice-like systems, which can be approximated by eq. 2[41]:

$$\frac{1}{I(q)} = \frac{1}{I_0}\left(1 + \frac{q^2\xi^2}{3}\right) \qquad \textit{Eq. 2}$$

where ξ is a characteristic size of the lattice mesh. The data was fit to this equation using a linear least squares approach of the data in the regime $q\xi < 1$ for the plot of 1/I(*q*) vs q^2.

For a more generalized system, the Guinier approximation for the low *q* regime follows[43]:

$$I(q) = I_0 e^{-(q*r_g)^2/3} \qquad \textit{Eq. 3}$$

where R_g is the radius of gyration for of the typical scattering element. The gels were analyzed using a unified model posed by Beaucage[44] in which Equations 1 and 3 are combined to model the scattering pattern in its entirety. An error function accounts for the transition between the Guinier and power-law regimes where around $q^*R_g=1$[44]:

$$I(q) = Ge^{-q^2R_g^2/3} + B\left\{\frac{\left[erf\left(\frac{kqR_g}{\sqrt{6}}\right)\right]^3}{q}\right\}^P \qquad \textit{Eq. 4}$$

A further generalization of this model allows for contributions from multiple scattering elements of n discrete sizes, but for this work, no more than two *R*g were needed to describe the gels across the q range analyzed and the following model, also from Beaucage[44], was :

$$I(q) = \sum_{i=0}^{i}\left\{G_i e^{-\frac{q^2R_{g,i}^2}{3}} + B_i e^{-\frac{q^2R_{g,i+1}^2}{3}}\left(\frac{\left[erf\left(\frac{kqR_{g,i}}{\sqrt{6}}\right)\right]^3}{q}\right)^{P_i}\right\} \qquad \textit{Eq. 5}$$

This model was intended for systems whose structural elements span orders of magnitude difference. For the systems in which $R_{g,i}$ and $R_{g,i+1}$ are not significantly separated – there is no or limited power-law decay between the $R_{g,i} \approx 1$ and $R_{g,i+q} \approx 1$ regions – the B_i term will tend towards zero. Given this tendency, and the range of q available to analyze, the generalized equation:

$$I(q) = G_1e^{-q^2R_{g,1}^2/3} + G_2e^{-q^2R_{g,2}^2/3} + Be^{-q^2R_{g,3}^2/3}\left(\frac{\left[erf\left(\frac{kqR_{g,2}}{\sqrt{6}}\right)\right]^3}{q}\right)^P \qquad \textit{Eq. 6}$$

was chosen to describe the scattering from the TMOS gels used in this work. The radii of gyration and the power-law exponent were calculated for each gel size, wherever there was sufficient data (i.e., *q*-range) to do so.

For the *in situ* counter diffusion experiments, the previously described scattering behavior was subtracted from the data to focus on the contributions to the scattering pattern from the nucleating particles. This background subtraction was performed on all the SAXS patterns using the pattern taken from the first scan at a given location for a particular experiment. The timing of the initiation of the precipitation reaction was estimated by tracking the Porod invariant (*Q**), a reflection of the phase composition and mean scattering density that measures the total scattering in a system, over time. This was calculated following Equation 7:

$$Q^* = \int_0^\infty q^2I(q)\,dq = \int_{-0.003}^{0.1} q^2I(q)\,dq \qquad \textit{Eq. 7}$$

with the integral being discretized using a trapezoidal approximation covering the *q*-range of available SAXS data.

When new particles are formed, the scattering from each contributes to the total scattering of the system according to (Equation 8):

$$I^{particle} = 2\pi^2 \int_V \rho^2(r)dr \qquad Eq.\ 8$$

Which represents the integral over the volume of the new particle ρ is the particle density (relative to its surroundings). The cumulative increases in scattering can be seen in the example data presented in Figure 4. At the point of first nucleation, the total scattering in the system increases – and can be seen as in increase in the porod invariant. The time point of this change in Porod intensity can be used to determine the induction time of the precipitation reaction. These induction times were determined individually as the differences between experiments were significant enough to not necessitate an automated algorithm to determine the changes.

Simultaneously, the WAXS data were analyzed to determine the nature of the forming crystalline solids. An example of a typical WAXS pattern is shown in Figure 4. In order to quantify the relative percentage of each crystalline phase, the background was removed using a polynomial fitting algorithm in which the curve was fit in segments while ignoring points located on a peak. This algorithm was necessary to avoid the negative values that would be reported by a simple background subtraction of patterns that had a decreasing background over time as shown in Figure 4b. With the background removed, the presence of different solid phases could be detected by simple measurements of peak heights (analyzing the peak area did not significantly change the accuracy), and changes in the relative concentration of different solid phases could be measured by tracking the relative intensity of different scattering peaks.

Especially during the first stages of nucleation, it is not guaranteed that the forming crystals will have sufficiently random orientations (significantly, there may not even be enough crystals to generate a full complement of random orientations) to guarantee perfect powder diffraction patterns comparable to those obtained for powder samples of celestine and hemihydrate[45]. To account for this, multiple peaks were tracked for each solid and the sum of the intensities of the peaks were reported. To facilitate the tracking of these peaks, *q* values from the synchrotron experiments were converted into two theta scattering angles for easy comparison to XRD data presented

in chapter 1. For celestine the peaks at 2θ = 27.1°, 30.1°, 32.9° and 44.3° were tracked and for the semi-hydrate, peaks at 2θ = 14.2°, 24.8°, and 28.7° were monitored.

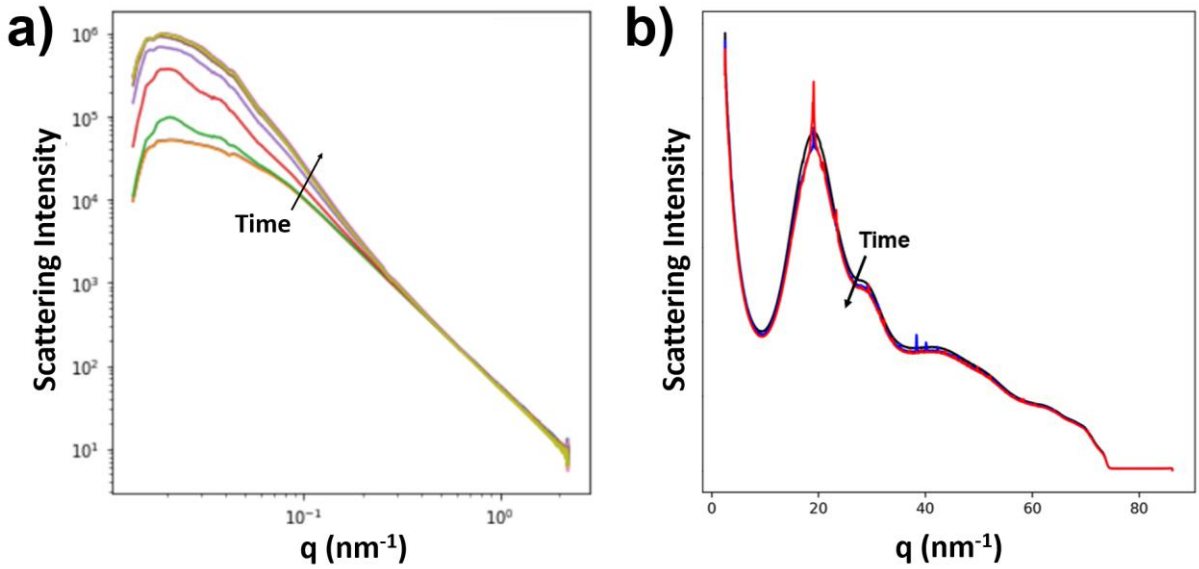

Figure 4: *Left – example of integrated SAXS scattering during an experiment (including gel scattering) showing how total scattering increases during the experiment. Right – Example of integrated WAXS data with high background levels. The background levels decrease during the experiment, making background removal a necessary step for tracking peak growth. Both sets of example data were taken from experiments of 500mM salt diffusion into a 15 v% TMOS gel measured in glass capillaries.*

2.2.3 X-ray absorption near-edge spectroscopy (XANES)

One set of XANES experiments was conducted at beamline BM30/FAME[46] of the ESRF (France). X-ray optics consisted of 2 mrad horizontal and 0.3 mrad vertical divergences focused by Rhodium mirrors and limited by four sets of micrometic slits resulting in a spot size of roughly 100 μm (vertical) by 200 μm (horizontal). The beam was monochromated by two Si(111) crystals. Incoming and transmitted beam intensity was monitored by measuring x-rays scattering during passage through air filled chambers. For certain experiments and standards, supplemental data were recorded using a Ge fluorescence detector shielded with layers of Al foil chosen as necessary for the conditions in each *in situ* experiment. Spectra were collected from 16 to 16.35 keV with 1.5 seconds integration time resulting in a time resolution of ca. 6 minutes per scan.

A second set of XANES experiments were conducted at the XAFS (x-ray absorption fine structure) beamline of the Elettra synchrotron (Italy)[47]. X-ray optics incorporate a tungsten mask and water-cooled, Pt coated Si-mirror placed 3mrad from the beam. Two Si(111) crystals were again used to monochromate the beam. Finally, a second set of tungsten slits are used to define the beam incident on the sample

(roughly 500 μm horizontal and vertical spot size). Beam intensity incident and transmitted are measured using ionization chambers. For these experiments, spectra were collected from 16 to 16.4 keV with an integration time of 1 s for a time resolution of ca. 7 min. For these experiments, only the absorption/transmission signal was observed.

For XANES experiments 3 samples were monitored simultaneously. Samples measured at ESRF were measured in three locations, 1 mm apart each, with the central spot aligned with the center of the gel. Each spot had a roughly 500 μm spot size. At Elettra, due to a larger spot size (ca. 1.5 mm in diameter) and a desire to increase time resolution, only two locations were scanned, each overlapping in the center of the gel. Schematics of the scan locations and spot sizes are shown in Figure 5.

Figure 5: *X-ray beam spot and size configurations for gel diffusion experiments. Each black dot represents the approximate spot size and location of the incident beam on the sample. The light green region indicates the location of the silica gel, and the orange the kapton (or glass) capillary. When multiple samples were evaluated together, all spots on one sample were measured before moving on to the next sample.*

The scanning parameters (energy range, number of discrete energies measured, acquisition time, etc.) for each experiment were selected to balance spectral information accuracy and time resolution. Measurement time at each energy was selected by finding the duration needed to get an absorption spectrum for a gel containing 20 mM $SrCl_2$ that had minimal noise. This time, ~1 s per energy measured, was considered to be the minimum usable measuring time to ensure accurate statistics. Additionally, a non-uniform density of the measured energies was collected.

The highest density of measured energies occurred near the absorption edge, where the density of information is greatest, and fewer points were measured further from the edge. The exact measuring parameters for the experiments at ERSF BM30 and Elettra XANES beamline can be found in Supplement A.

Note on the nomenclature: XANES is used to describe the data and experiments in this section, but the data actually collected includes information that is generally associated with XAFS experiments as well. However, due to time resolution constraints – namely, a single scan requiring upwards of 5 minutes to acquire enough statistics for a good absorption spectrum – and the rapidly changes occurring within the system during a nucleation reaction, it was decided to limit the scope of the analysis. This was done to avoid "discovering" artifacts that are the result of a scan being from one system state near the absorption edge, and a different one far from the system edge. Some brief attempts were made to calculate some structural information by looking at only the first shell where the time-resolution effects would be the smallest, but there was little-to-no useful information gained at that level of analysis. Thus, the name "XAFS" deemed inappropriate for describing the results that could be reported with sufficient confidence.

2.2.4 XANES data analysis procedure

In situ XANES spectra were compared to standards taken at the beginning of the experiment. Solid standards of celestine and hydrate (as synthesized according to previous descriptions[45]), $SrCl_2*6H_2O$ (Acros Organics, 99% pure), SrAc (Sigma Aldrich, >98%), $Sr(NO_3)_2$ (Honeywell Fluka, >98%), and $Sr(OH)_2$ (Sigma Aldrich, 94%) were measured in pellet form at BM30 (ESRF) and used as comparisons for all XANES experiments. These solid pellets were measured in transmission mode. Additional aqueous strontium standards were measured using the fluorescence mode: $SrSO_4$ 0.5 mM (undersaturated with respect to Celestine), $SrSO_4$ 10 mM (supersaturated with respect to celestine), and 500 mM $SrCl_2$ (undersaturated). The aqueous standards were taken again at Elettra during the beam calibration phase in transmission mode. All experimental data were analyzed using the aqueous standards measured at the same beamline.

XANES data were analyzed using the Athena software from the Demeter package[48]. Standards and experimental data were normalized in the pre- and post-edge regimes following standard practices for XANES data analysis[49]. For standards,

an effort was made to ensure (as was reasonable) that the post-edge normalization curve bisected the portion of the absorbance curve after the first peak and before the first local minimum above the absorbance edge.

Linear combination fitting was used to evaluate the species present at different time points during the experiment. For this analysis the Athena linear combination fitting tool was employed. The purpose of these fits was to track the relative quantities of aqueous $SrCl_2$ and $SrSO_4$, celestine, and hydrate, as well as to see if there are any features of the spectra not explainable by a combination of the previously listed standards indicating the presence of a previously unknown phase. Considering that all of the aqueous standards were nearly identical (see Results and Discussion), we are essential dealing with a three-parameter system: aqueous Sr^{2+}, celestine, and hydrate.

Before doing the fitting, all standards and experimental spectra were aligned to the same Sr K absorption edge (based off that of celestine) using the Athena auto-align feature in “align first derivative” mode. This resulted in fits that were “blind” to small variations in the adsorption edge – a feature that was necessary in order to prevent overfitting to small, random variations in the measured absorption edge. For the data collected here with fast scans, this was necessary as spectra of the same standard were varying by up to 0.5 eV randomly – thus presenting a feature where the least squares fitting algorithm over-fitted these small fluctuations in absorption edge at the cost of accurately fitting the oscillations behind the absorption edge. The accuracy of the fits was verified manually (without mathematical parameters) using the data without alignment treatment. All fits are presented without any alignment applied to the data, but the χ^2 values are taken from the “edge blind” least squares fitting algorithm.

Fitting was performed with the assumptions that the linear sum of the components would equal 1 and that all standards would have a value between 0 and 1. This ensured that the linear combination fitting result represented a summation of the fractional components present, and those fractional components would represent everything in the system. Fits that included a negative concentration of one constituent species were disregarded. In order to reduce computation time, another parameter was used that limited the total possible number of standards used in evaluation to 4. This allowed for the assumed three-component system to be tested for the presence of a singular unknown phase via comparison to the other standards. The fitting range was selected to range from 20 eV below the absorption edge to 120 eV above the

absorption edge. This range encompassed the majority of the unique maxima, minima, and inflection points in the spectra of the standards, ensuring sufficient information for fitting, while still leaving some oscillations outside the fitting regime for verification that the good fit extended beyond the computed regime.

When evaluating the fits, several parameters were evaluated. The mathematical best fit was presented by Athena as the combination of standards whose fit reduced to the lowest χ^2, but a manual evaluation of each fit was performed as well. The low integration times used in the experiments frequently resulted in noisy data, which led to occasional over-fitting of noise by Athena and these over-fits were discarded. Additionally, fits were checked such that all significant maxima and minima were accounted for by the standards used. By this criterion, the “best fit” was determined not to be the mathematically smallest deviation from the curved. Finally, any standard that was “fit” at a presence of less than 0.5% was discarded – it was considered that due to noise, such small deviations from ideal fitting could not be accurately measured.

3. Results

3.1 SAXS/WAXS data of pure silica gels – pore sizes

The first step, prior to evaluating the confined nucleation experiments, was to characterize the pore sizes of the synthesized gels, and how these vary with the TMOS concentration[41] used during synthesis. As seen in Figure 6, the SAXS scattering patterns of the mesoporous TMOS silica gels are different for each of the TMOS concentrations used. A change in the slope at low *q* is visible for the scattering curves of samples with higher TMOS concentrations, characteristic of particle scattering. This particle scattering can be attributed here to the occurrence of pores in the silica matrix. The position in *q* of this change in slope varies for each sample, shifting to lower *q* values with decreasing TMOS concentration, indicating larger pores for samples synthesized with lower TMOS, as expected[41]. The Guinier regime is not observed in the accessible *q* range for the curves from the samples with lowest TMOS content, indicating pore sizes are too large to be characterized by SAXS analysis with available the experimental configuration.

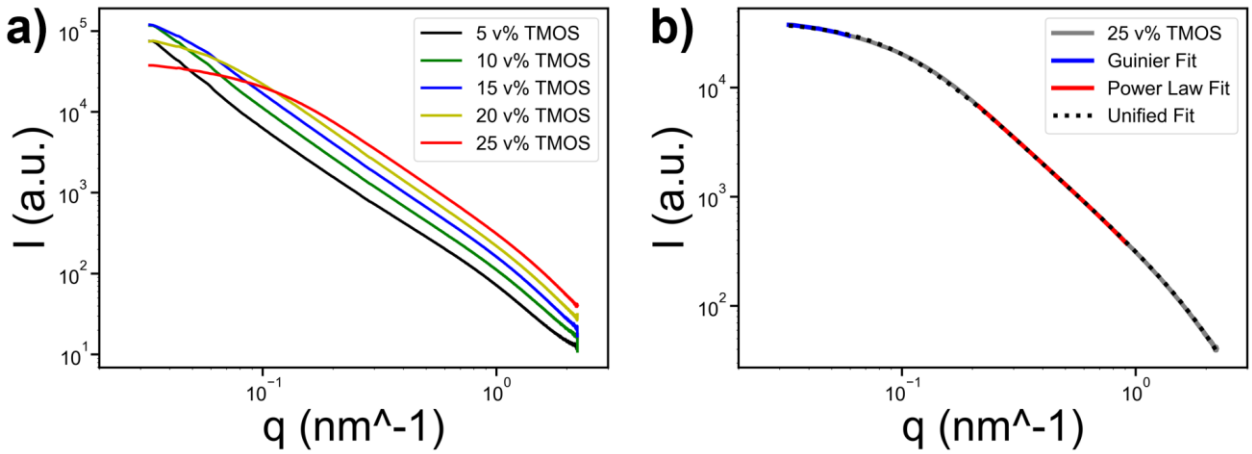

Figure 6: *a) SAXS diffraction patterns of various concentrations of silica gel – synthesized by mixing 5, 10, 15, 20, and 25 volume percent TMOS in deionized water with no additives. The increase in scattering intensity at high q and the rightward shift of the transition out of the porod regime indicates that the gels with higher silica concentrations have smaller pores. b) Fitting of a scattering pattern obtained from a gel with the smallest pore size (25 v% TMOS). In blue is an indication of what region of the pattern a single Guinier approximation fit that found a 16.8 nm R_g, and in red the regime used to fit the porod regime and has a slope of -1.88. To complete the fit and obtain the dotted black line, two more R_g of 11.8 nm and 6.7 Å were also found.*

Also seen in Figure 6a (especially apparent in the SAXS curves for the samples with TMOS 15%, 10% and 5%) are slope changes around $q = 10^0$ nm^{-1}. This slope change is indicative of the presence of a second smaller particle scattering contribution at high q values, likely indicating the presence of a second population of pores of smaller sizes, in the range of 5-6 Å. These SAXS scattering patterns were fitted to the

Equations 2 and 6 to find descriptive parameters. An example of a fitting using Equation 6 is shown as a dotted line in Figure 6 (right panel), as well as indicators of the regions where a single Guinier approximation of the largest pores and the dimensionality of the polymer fractal are seen.

Table 2 shows the results of the fitting of all the tested TMOS gels. The mesh sizes from the lattice approximation (ξ) and the power-law exponent of -2 for all gels corresponds well with those reported previously in literature.[41] As seen in the table, pore size increases as the silica volume fraction decreases (and the lack of available data for the 5% gel suggests the trend continues past the measurable *q* range), with all gels featuring pores in the nanometer length scale. This trend also suggests that the radii observed are in fact indicating pore sizes, not polymer globs, as increasing the polymer concentration would increase the measured size of polymer agglomerations. Additionally, the presence of multiple measurable R_g in the 25 v% gel is indicative of a fairly wide distribution of pore sizes.

Table 2: *Parameters of silica gels based on fitting the scattering patterns as found in figure 6. parameters absent from the table would require access to a lower q range to calculate. Errors indicated by σ are uncertainty in the fitting algorithm only and do not represent any other sources of error such as data range selected for fitting.*

Gel	ξ (nm)	$R_{g,1}$ (nm)	$R_{g,2}$ (nm)	$R_{g,3}$ (Å)	P	$\sigma R_{g,1}$ (nm)	$\sigma R_{g,2}$ (nm)	$\sigma R_{g,3}$ (Å)	σP
25 v% TMOS	19.0	16.8	11.8	6.7	-1.88	0.1	0.05	0.03	0.001
20 v% TMOS	30.8	-	27.2	5.1	-2.02	-	0.2	0.04	0.002
15 v% TMOS	61.8	-	38.5	5.7	-2.01	-	0.3	0.04	0.002
10 v% TMOS	87*	-	50*	5.0	-1.99	-	2.1	0.03	0.002
5 v% TMOS	-	-	-	5.0	-1.96	-	-	0.05	0.002

** Low confidence, minimal data available*

3.2 SAXS/WAXS monitoring of $SrSO_4$ nucleation in counter-diffusion experiments

With the goal of determining the effects of confinement on the nucleation of celestine and the hydrate phase(s), different initial solution concentrations (from 20 to 500 mM) were used in the counter-diffusion experiments with the aim of having a wide range of supersaturations during nucleation. Figure 7 illustrates the general evolution of the SAXS patterns collected during these experiments, as well as some critical

concentration dependencies. In all reactions, the first particles are observed in the lower *q* range. For example, when 100 mM solutions of $SrCl_2$ and Na_2SO_4 were counter-diffused into the silica gel substrates, the observed reactions were found in the lowest q regime, which probes the largest pores of the available *q* range. In an experiment with 500 mM reactant concentration, scattering was observed at significantly higher *q*, indicating that precipitation reaction occurred also in smaller pores. This effect suggests that, in the absence of significant surface interactions[32,34], nucleation primarily occurs in the largest pores first. This preference for nucleation in large pores was observed for all tested surface functionalizations – -OH, -SH, $-OCH_3$ – contrary to previous reports for CaCO3[34], there was no observed effect of surface chemistry driving nucleation into the smallest pores.

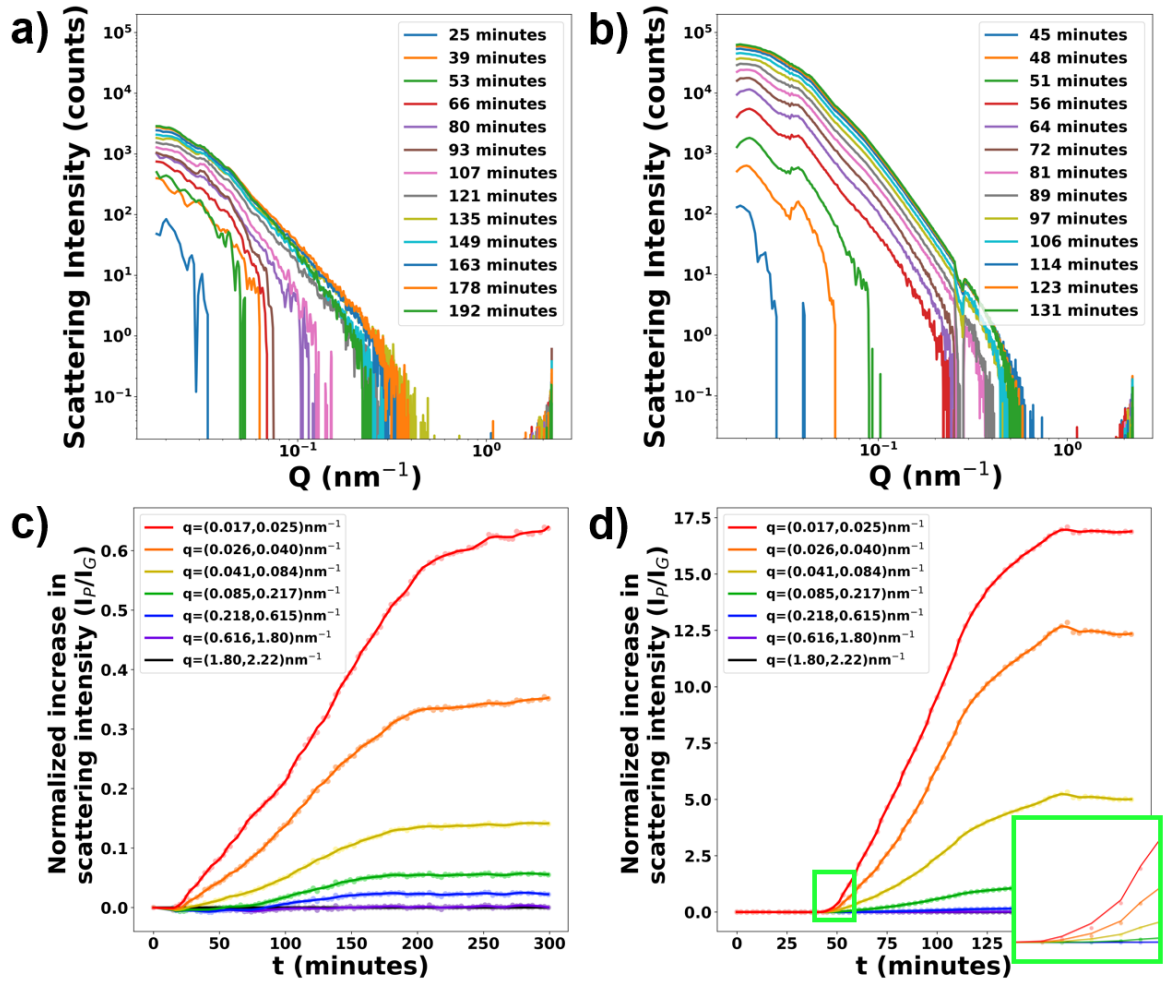

Figure 7: *SAXS scattering patterns for $SrSO_4$ counterdiffusion experiments measured in glass capillaries and their evolution by q regime as a function of time. a and b) Time-resolved patterns from a 100 mM counterdiffusion experiment (a) and a 500 mM diffusion experiment (b). Both example data have been background subtracted to remove the scattering from the silica gel and capillaries. c and d) scattering from the precipitates (I_P) measured relative to gel scattering (I_G) as a function of time across various q regimes for the above counterdiffusion experiments. Inset in d is a highlight of the early nucleation period from the 500 mM experiment.*

Additionally, the fastest rates-of-change observed in the experiment happened just after nucleation (c.f. Figure 7 c & d, and Figure 8). This indicates that after the first nucleation event, the rate of solid formation in the system initially increases, but a relatively steady state is reached by the end of the experimental time. Despite this relative steady state, the *q* range for which nucleation was observed in the 100 mM does not reach the same extent as that observed in the 500 mM system. A possible explanation for this is that once nucleation occurs in the largest pores, ion diffusion is significantly restricted in the system, greatly reducing the rate of further solid formation. This effect is consistent with literature results for macro pores and observations made during simulations of nucleation in mesoporous systems[12,32].

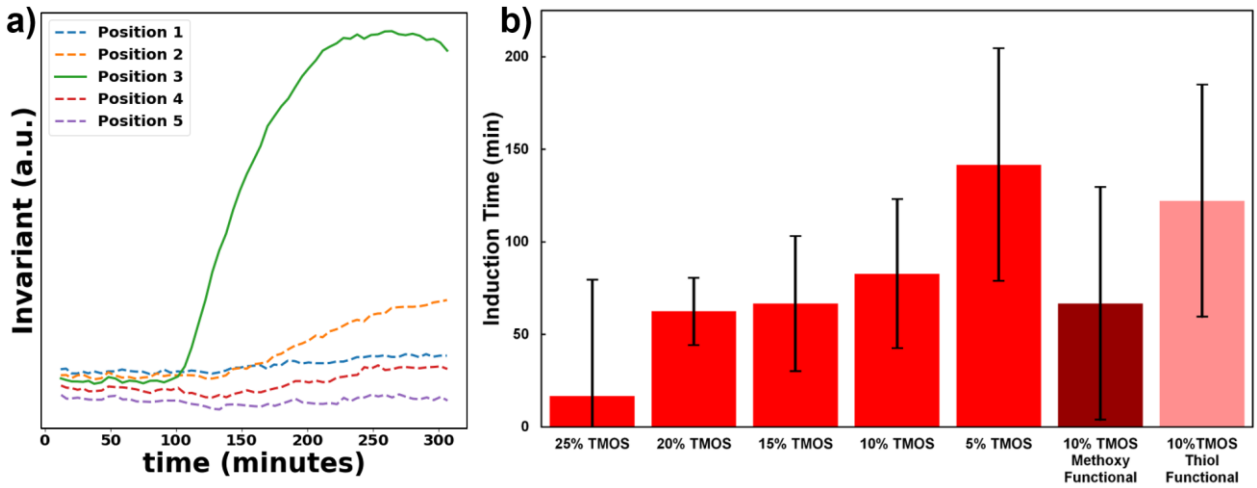

Figure 8: *a) Evolution of the porod invariant during an experiment where 100 mM ion concentrations were diffused into a 10% TMOS gel functionalized with thiol groups measured in glass capillaries. b) Induction time for nucleation defined by changes in the porod invariant across experiments of 100 mM ion diffusion into TMOS gels measured in glass capillaries. Error bars represent standard deviation from all measured experiments (n=2 for 20% TMOS, n=3 for 10% TMOS, 15% TMOS, and thiol functionalized gel) experiments, except for the cases where only one experiment was successfully completed (5% TMOS, 25% TMOS, and methoxy Functionalized) – the maximum error from the other conditions was assumed for those cases.*

The evolution of the precipitation reaction can be readily monitored by calculating the total scattering of the system, which is represented by the Porod invariant (Equation 7). Figure 8 illustrates a typical example of the porod invariant for an experiment of 100 mM reactant concentration. The green solid line represents the behaviour at the location in the sample where the bulk of nucleation occurred. There is an initial rapid increase in scattering, followed by a plateau, clearly indicating the completion of the nucleation reaction. Using these invariants, the induction time for nucleation is calculated. Typically, induction time refers to the time between the onset of supersaturation and nucleation being observed. For the purpose of this discussion, the diffusion time of ions into the silica gel is also included in the induction time. These

induction times were determined from the first appearance of an increase in scattering, regardless of the position within the gel.

The induction times for 100 mM diffusion experiments across all gel configurations are presented in Figure 8. Despite significant variance from experiment to experiment, it is still evident that the highest density silica gels exhibit the fastest nucleation times. This effect, along with Methoxy functional groups accelerating nucleation and Thiol functional groups slowing it, was consistent across all experiments and concentrations. During a single set of experiments where several gels were tested simultaneously, there was always an increase in induction time with increasing pore size, and the induction time sequence of Thiol functionalized > no functional groups (OH surface) > Methoxy functionalized held as well – regardless of the concentration of ions present in the system.

The increase in induction time with increasing pore size contradicts the expectations formulated by PCS theory (pore-controlled solubility). PCS predicts that in smaller pores, the critical saturation at nucleation should be higher, due to a higher effective solubility. Therefore, if diffusion rates were similar across all samples, the supersaturation levels would be lower in smaller pores, leading to slower nucleation. To explore this effect, a variation of the Kelvin equation was applied[33,50]:

$$S_p = S_0 \, exp\left(\frac{4 v_m \gamma \cos\theta}{RTr}\right) \qquad \textit{Eq. 9}$$

Where S_p is the pore altered solubility, S_0 is bulk solubility, v_m is molar volume of the mineral, γ is interfacial energy of the nucleate, θ is the contact angle between the crystal and substrate, R is the gas constant, and r is the radius of the pore. The ratio S_p/S_0 is explored by calculating the molar volume for celestine and hemihydrate from previously measured unit cell parameters[39] ($4.62*10^{-5}$ m^3mol^{-1} and $5.90*10^{-5}$ m^3mol^{-1} respectively) and taking an estimate of the interfacial energy from the supplemental information section of chapter 2 (35 $mJ.m^{-2}$ for celestine and 3 $mJ.m^{-2}$ for hemihydrate). These estimates are within reasonable agreement with literature values for celestine [eg. 51], and reports from molecular dynamics simulations of the analogous $CaSO_4 \cdot xH_2O$ systems by Mishra et al.[52] where the energy is predicted to be significantly lower when x=1/2 than when x=0 (which is corroborated logically by the mineral with lower solubility having higher surface energy). No data exists for the $SrSO_4 \cdot xH_2O$ system/silica contact

angle, so a full range from 0 to 90° was modeled, as well as a range of pore radii to the range of possible PCS effects in this experiment (Figure 9).

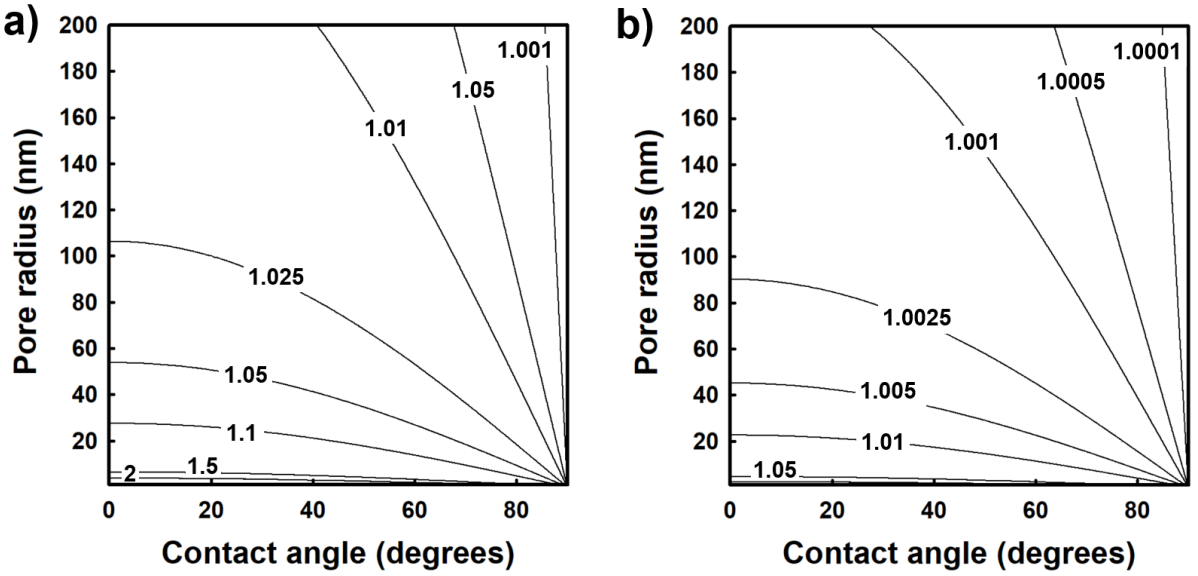

Figure 9: *Estimations of PCS effect by contact angle and pore radius for $SrSO_4$ in water as estimated by the modified Kelvin equation (Eq. 9). a) PCS effect for celestine nucleation, b) PCS effect for hydrate nucleation.*

For the samples with the smallest pores, ca. 16 nm (Table 2), it would be expected that saturations would have to reach approximately 1.3x bulk saturation to initiate celestine nucleation within these pores. At the same time, for the largest pores (an extrapolation of Table 2 data estimates 90-100 nm), the PCS effect would be predicted to be minimal, no more than 1.025 for celestine nucleation. If hydrate is the first nucleated phase, the PCS effect would be predicted to be less of a factor. However it would still be somewhat harder to nucleate in a 16 nm pore (ca. 1.01x bulk saturation) compared to a 90-100 nm pore (ca. 1.002x bulk saturation). The prediction that the PCS effect increases the critical supersaturation in solution is based on unfavorable surface interactions, which would incur an energetic “price” to form a crystal/substrate interface or even in cases of homogeneous nucleation. If there are favorable interactions between the substrate (where the contact angle would become greater than 90 degrees), this same analysis starts to predict lower supersaturations necessary for smaller pores as the cosine term from Equation 9 would change sign, causing the exponential to drop below 1.

A continuation of this analysis raises the question of what type of particles nucleates first within the pores. To learn the shape of the first solids formed, the power-law regimes of the scattering patterns were fitted to Equation 1. Power law slopes of -

4 are indicative of scattering from smooth-surfaces and particles, while the gels and pore spaces had a fractal slope of -2 – which is common of mass fractals or lamellar structures (generally considered to have a slope in the range [-2,-3]). Intermediate slopes (range [-3,-4]) are attributed to surface fractals, or very rough surfaces. Figure 10 shows analyses of some characteristic experiments at 100, 50, and 20 mM reactant concentrations.

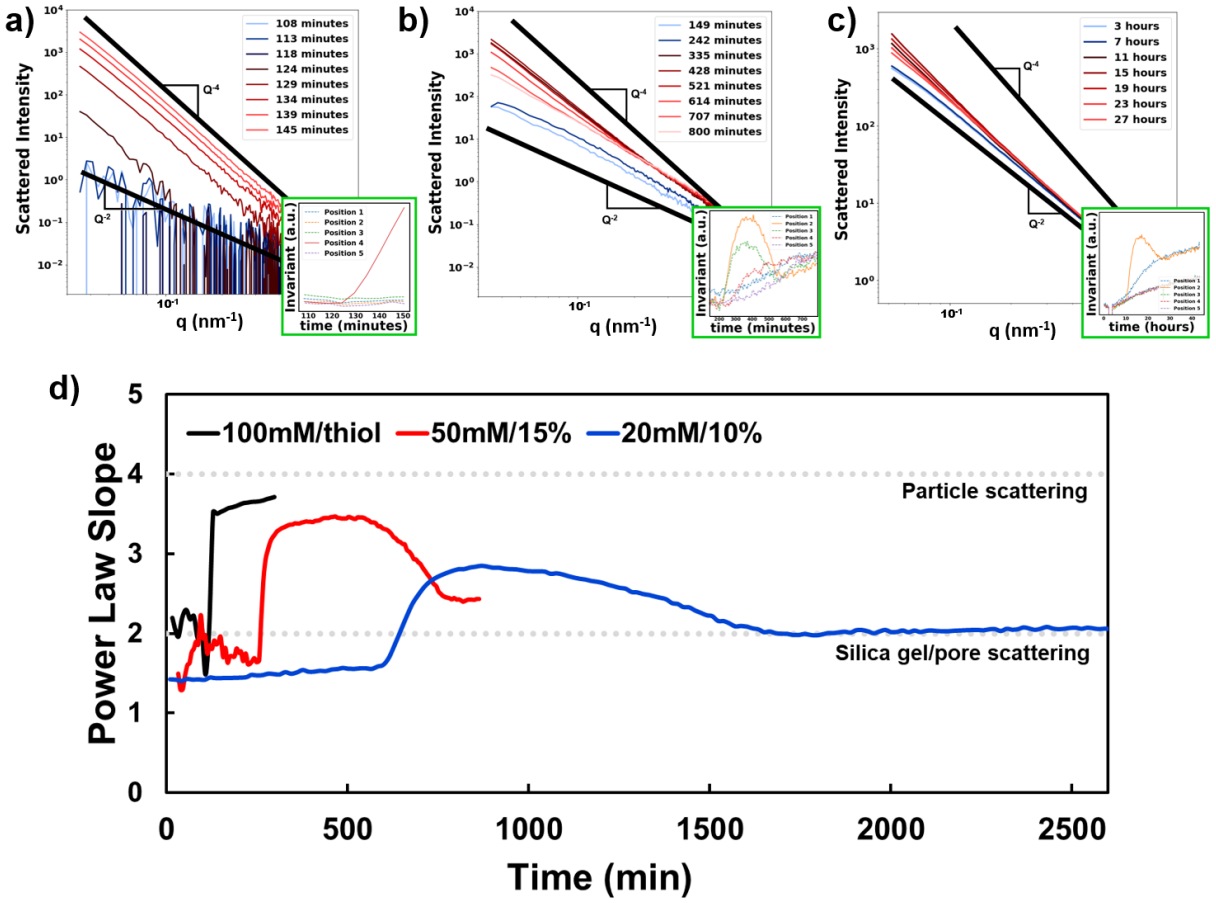

Figure 10: *Porod regime analysis for counterdiffusion experiments of different concentration salts. a) time evolution of scattering in a 100mM counterdiffusion experiment in 10% TMOS gel with thiol functionalization, b) time evolution of scattering in a 50mM counterdiffustion experiment in 15% TMOS gel and c) time evolution of scattering in a 20mM counterdiffustion experiment in 10% TMOS gel. d) time evolution of the absolute value of the slope of the line of best fit for the plot of Log(I) vs Log(Q) in the example experiments. the sudden change in slope from the initail baseline value is indicative of nucleation occuring.*

Figure 10a shows only the scattering immediately before and after nucleation for a 100 mM counterdiffusion experiment (alongside an inset that shows the invariant for only the shown scattering patterns). It is apparent that before the nucleation, there is a slope of ca. -2 as expected for scattering from the pores, visible due to slight increases in the solution density as the salinity increases. At nucleation, slopes of ca. -3.6 are achieved almost immediately with the slope continuing to approach -4 as the

experiment progressed. For the lower concentrations (Figure 10 b and c) this trend is slightly less clear. At 50 mm, slopes of -3.4 were achieved rapidly, but after some time, the slope of the scattering pattern began to trend back towards -2. For the 20 mM experiment, the change is more stark as the power-law slopes never exceed -3 before returning to -2 by the end of the experiment. The bottom plot shown in Fig. 10 tracks these slopes over time for the example experiments and reveals that, while none of the experiments attained the $I \propto q^{-4}$ slope representative of spherical particle scattering, the slowest and lowest concentration experiments have the lowest extrema in the power-law exponent. For the two slower experiments, after the initial appearance of steeper scattering curves, there is a return to the $I \propto q^{-2}$ (at least much closer to that) slope that is representative of the shape of the pore space.

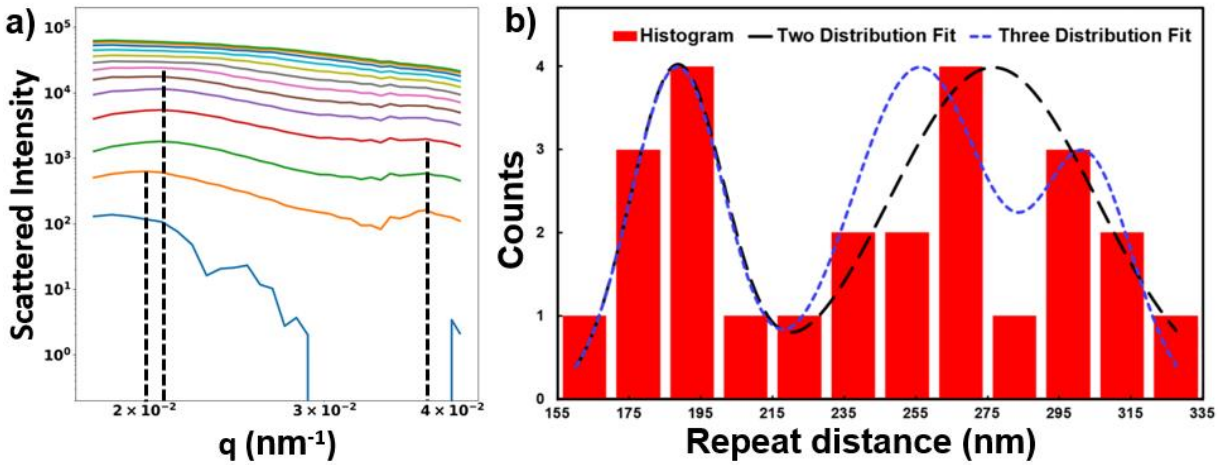

Figure 11: *Left: Zoom of low q region from scattering pattern of a 500 mM $SrSO_4$ counterdiffusion experiment (Figure 7b). Dashed vertical lines indicate local maxima. Right: Histogram of the repeat distances found in all experiments by analyzing the protrusions and local maxima in the scattering patterns. For this analysis, the example experiment resulted in a count of two local maxima – one of which developed over time (at q≈0.02 and 0.0205). Fits of the histogram with normal distributions show that there are likely two or three regular repeat distances that appear during the experiments.*

An analysis of scattering at the lowest *q* available in any experiments reveals another feature of the early-nucleation scattering curves. Several experiments contain local maxima in the scattering patterns like those illustrated with dotted lines in the scattering patterns of Figure 11. Maxima like this in SAXS exeperiments are most frequently attributed to frequently repeated spacings between scattering interfaces. The right plot of Figure 11 shows a histogram of all local maxima found after the associated *q* has been translated into the actual distance by the relation $d=2\pi/Q$. The distribution of repeat distances was found to be best represented by two (means = 188.4 nm and 276.4 nm) or three (means = 188.4 nm, 256.0 nm and 302.7 nm) normal distributions. In any case, all the repeat distances found associated with local maxima

in the scattering patterns during nucleation far exceeded the predicted pores sizes of the silica gels.

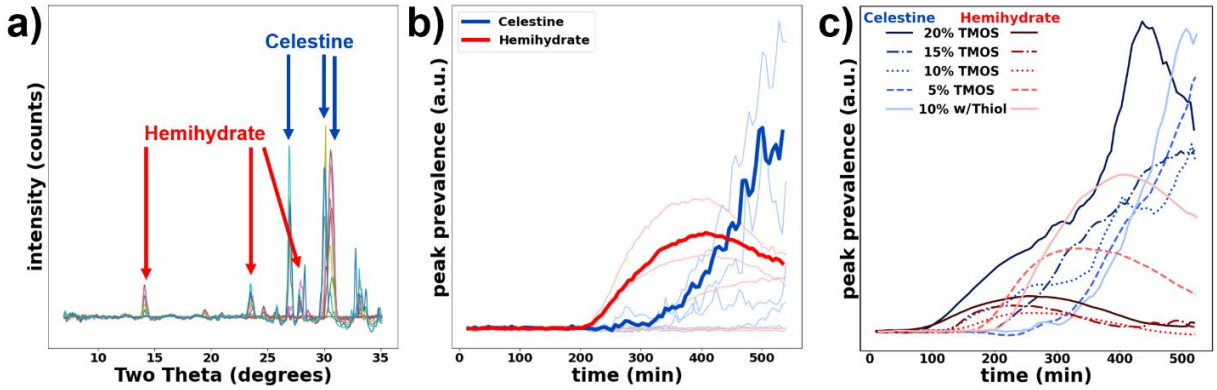

Figure 12: *WAXS analysis of a series of 100 mM counterdiffusion experiment. a) example of development of WAXS scattering pattern evolution during an experiment (taken from experiment using a 20% TMOS gel with peaks that were used to trace solid species indicated by arrows (one additional peak was used for celestine – not shown for figure clarity). b) example time evolution tracing of peak heights. The heavy lines indicate 2x the average of total peak height from all observed positions measured in the gel, with the individual positions shows lightly behind. c) smoothed and averaged time evolutions for all gels evaluated in the experiment.*

While the SAXS data indicate where and when solid is forming, it does not allow to characterize the crystal phase present. Simultaneously acquired WAXS patterns can probe the crystal structure and help to elucidate the nature of the solids being formed. For these analyses, the measured *q* has been translated into two theta diffraction angles to facilitate comparison to the diffraction patterns presented in Chapter 2 of this work. Early observations of reactions performed in glass capillaries, the peak at an equivalent diffraction angle of 14.2° (the peak at the lowest scattering angle shown in Figure 12a), which is unique to the hydrate solid phase, appears in diffusion cells containing 500 mM initial salt concentrations, but is not readily apparent in systems with 100 mM and below. However,–For experiments performed in 1.2 mm kapton capillaries (in 1 mm it was more difficult to observe hydrate), the presence of the hydrate phase was found in all gels without regard of pore size or surface functionality (Figure 12). Furthermore, the amount of hydrate present in the system appears to increase initially, reach a peak concentration, and subsequently begin to decrease. This is fully consistent with the behavior of the hydrate phase as a metastable phase that dissolves and transforms into celestine, as discussed in detail in chapter 2. The kinetic persistence of this phase while confined in these gels, even at relatively low quantities of hydrate, was shown to significantly exceed the 300 min maximum found during experiments outside of gels. This is in agreement with a known effect where porous media can stabilize metastable species[53].

Another observable trend from the experiments presented in Figure 12 is that the relative amount of hydrate present in the system is significantly higher for thiol functionalized gels than for any of the pure silica gels. When considering all of the experiments conducted and the data presented in Supplements B and C, this promotion of the hydrate phase is not consistent in methoxy functionalized gels, but does appear to be consistent in gels containing thiol functional groups.

Additional observations of the gels in kapton capillaries using the WAXS detector (Figure 12c – with further evidence in the supplements), suggest that most experiments run with 100 mm solution concentrations show the presence of hydrate – either nucleating before, or coincidentally with celestine. Some experiments conducted using 50 mM diffusing solutions also showed the presence of the hydrate phase – including an experiment with the thiol functionalized gel. It is apparent that in the system of ca. 1.1 cm silica gels in kapton capillaries, 50 mM ion counterdiffusion experiments result in conditions near critical for hydrate formation. Thus, this condition will be the focus for evaluation of species formed using XANES analysis.

3.3 XANES data

The first step in evaluating the species present during diffusion and nucleation in the Sr-SO_4-H_2O system was to evaluate the spectra of Sr^{2+} ions in solution. Experiments discussed in earlier chapters indicated the possible presence of uncharged species, such as ion pairs and larger, during the nucleation of celestine. In an attempt to directly observe these species, XANES spectra of $SrCl_2$, as well as two concentrations of $SrSO_4$ (with NaCl background ions) were compared (see Figure 13). No significant differences were observed in the shape of the XANES spectra that would indicate a detectable presence of ion complexes when the sulfate ions were present. This observation leads to two very important considerations for analyzing counter-diffusion experiments. First, aqueous Sr^{2+} ions can be treated as a possible contribution without differentiation between the other ions present (i.e. the contribution of Sr^{2+} ions can be treated independently of the presence of SO_4^{2-} ions), and, second, that if complexes exist, they would need to have much higher concentrations in order to be observable by XANES in the bulk solution (during these experiments, it was observed that concentrations <3% resulted in unreliable measurements).

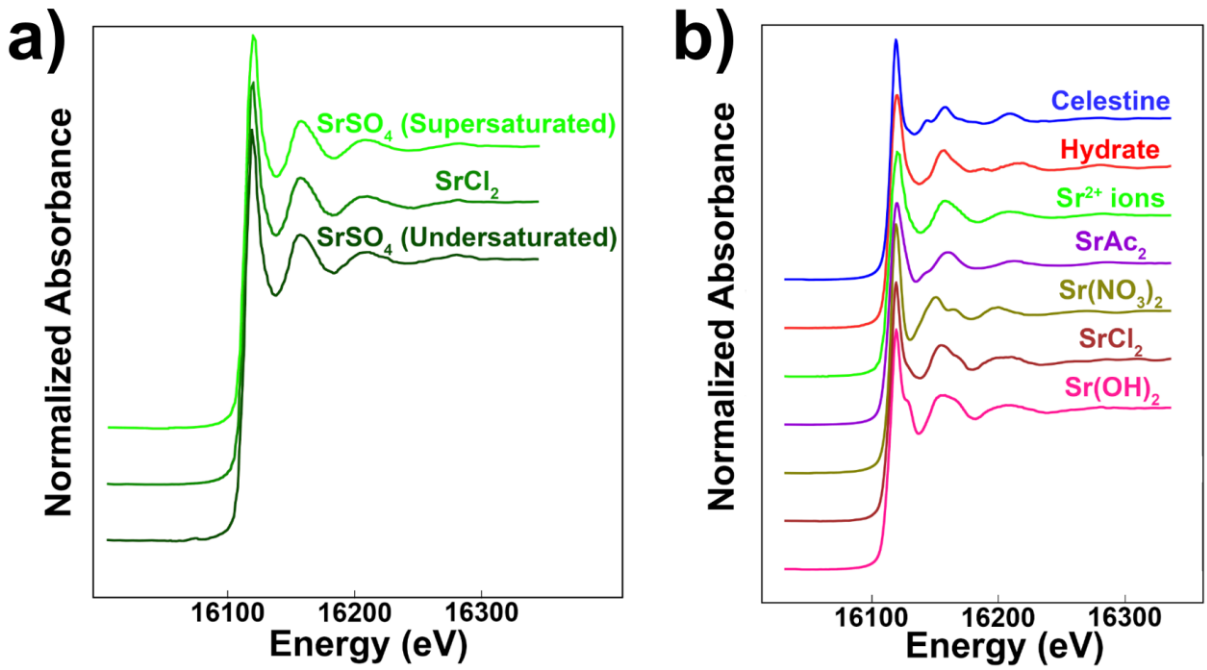

Figure 13: *Standards used in analysis of XANES data. a) aqueous standards showing that there is little to no difference between the absorbtion spectra of aqueous Sr^{2+} ions with respect to concentration or the presence of SO_4^{-2} in comparison to Cl^- ions. b) XANES spectra of solid reference spectra measured in pellet form, alongside the reference spectrum for Sr^{2+} ions in water.*

Linear combination fitting of the standards from Figure 13 (right) was used to analyze the in situ measurements of counter-diffusion experiments. Figure 14 shows an example of how the best fit was chosen. In this example, a slight improvement to the fit quality (as measured by χ^2) could be achieved by considering more standards, but this came at the cost of removing peaks from the absorbance spectra predicted by the linear combination fit. This is illustrated in Figure 14, where the inclusion of the Sr^{2+} ions in the model causes a flattening of the small absorption peak at 16180 eV that is indicative of hydrate presence (inset). A much higher ratio of hydrate to celestine concentration is predicted if the fit is chosen to preserve the peaks. Thus, when choosing the best fit for each experiment, peak preservation was prioritized over χ^2 reduction as long as the difference in χ^2 was minimal. Additional controls were made to ensure that the majority of the fitting was accounted for by phases that are known to be present and that the unknown phases (i.e. other potential transient phases) would be represented by minority concentrations. Important to note is that for the remainder of the discussion “known” standards will refer to Sr^{2+} ions, celestine and hydrate, and “unknown” standards will refer to the standards used to stand in for the potential previously unobserved phases – $SrAc_2$, $Sr(NO_3)_2$, $SrCl_2$, and $Sr(OH)_2$.

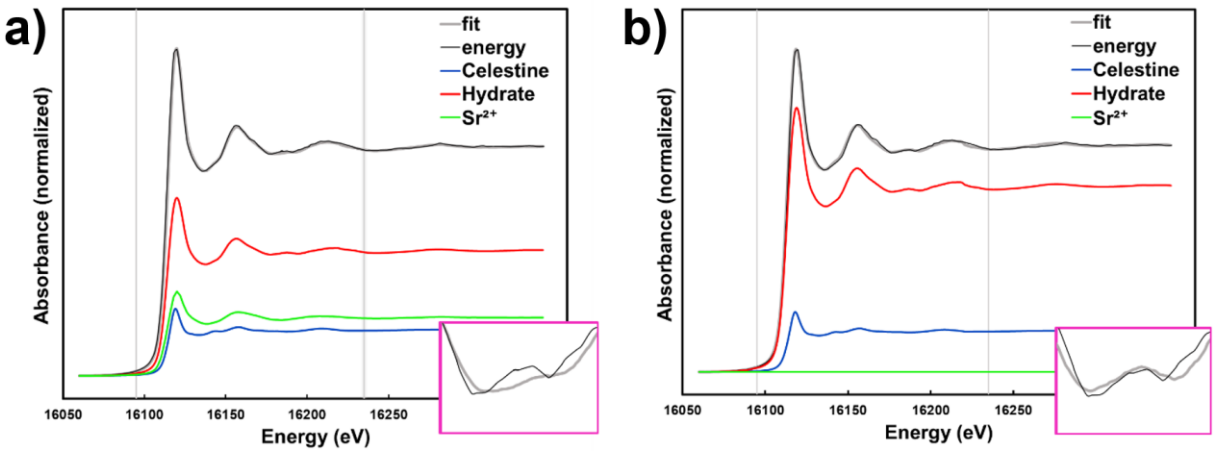

Figure 14: *Comparison of fitting of example spectrum from an experiment of 500 mM counterdiffusion in a thiol functionalized 10% TMOS gel. a) Same example spectrum fit with only the solid samples, and b) fitting utilizing Celestine, Hydrate, and Sr^{2+} ion standards. The mathematically better fit utilizes all three standards, improving deviations from the data around 16160 eV and 16200 eV. However, the inclusion of the Sr^{2+} ions in the model causes a flattening of the small absorption peak at 16180 eV that is indicative of Hydrate presence (inset). A much higher ratio of hydrate to celestine concentration is predicted if the fit is chosen to preserve the peaks.*

Table 3 highlights selected results from XANES fits of various experiments. In all experiments, the first observed strontium structure, as expected, is Sr^{2+} ions, indicating that the time resolution of the experiments was sufficient to observe the pre-nucleation stage of the experiments. The next significant species to appear in all experiments was the hemihydrate, which would increase in concentration, before gradually being replaced by celestine. This trend again agrees with results from observations of the bulk reaction in chapter 2 as well as the WAXS results presented in Figure 12.

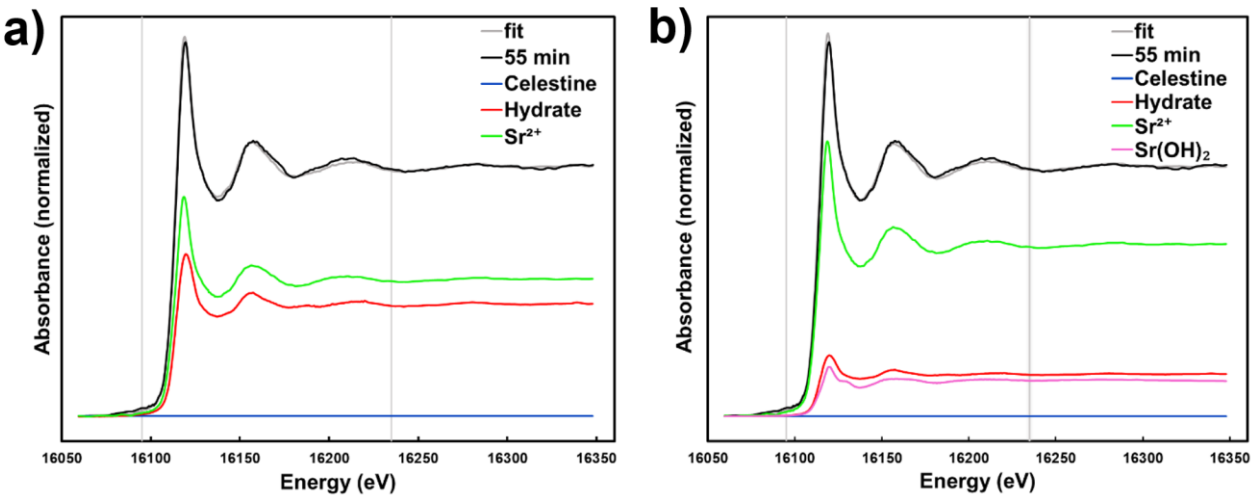

Figure 15: *example best fits, with and without references representing unknown species for an absorbtion spectra taken at 55 minutes into a 50mM counterdiffusion in a 10% TMOS silica gel. On the right is the fit using only the "known" species of Sr^{2+} ions, celestine and hemihydrate, while the right shows a fit using the same species augmented by the addition of "unknown" species. An improvement in fit can be observed in the first local minima (ca. 16140 eV).*

In the lower concentration experiments, the linear combination fitting could be improved by the addition of "unknown" species for most of the conditions. The predicted microstructure of these unknown species varied from measurement to measurement, sometimes best represented by $Sr(OH)_2$, $SrCl_2$, and $Sr(NO_3)_2$ – in one example, strontium acetate was even measured as a possible structural analog for the unknown species.

Table 3: *Concentrations of strontium species found by XANES observations during select counter-diffusion experiments. For all data points except 1, χ^2 improvement was achieved by adding possible unknown species to already good fits with only combinations of Sr^{2+} ions, celestine, and hemihydrate. For the experiment with 50 mM salts in a thiol functionalized gel, the best χ^2 at 188 minutes was found by fitting to $SrCl_2$ instead of Hemihydrate. Thus, the relative concentrations of Hemihydrate and unknown species could not be predicted for this measurement.*

	50mM Salts / 10% TMOS with thiol				**50mM Salts / 10% TMOS**			
Time (min)	**55**	**188***	**321**	**454**	**21**	**153**	**285**	**417**
Sr^{2+} Ions	87.3%	87.5%	0.0%	0.0%	81.4%	79.6%	51.4%	25.10%
Celestine	0.0%	0.0%	1.5%	18.4%	0	0	23.0%	57.20%
Hydrate	4.2%	12.5%	93.6%	73.1%	0.00%	14.5%	19.6%	17.70%
Hydrate fraction (of solids)	100.0%	100.0%	98.4%	79.9%	n/a	100.0%	46.0%	23.63%
Unknown standard	8.5%	?	4.9%	8.5%	18.6%	5.90%	5.9%	-
Best fitting unknown standard	$Sr(OH)_2$	$SrCl_2$	$Sr(OH)_2$	$Sr(NO_3)_2$	$Sr(NO_3)_2$	$SrCl_2$	$Sr(NO_3)_2$	-
Best χ^2	5.1E-04	1.8E-03	1.8E-04	1.2E-04	2.6E-03	6.3E-05	1.3E-04	2.1E-04
χ^2 improvement considering unknown species	6.8%	27.2%	2.0%	13.2%	7.77%	15.7%	5.8%	-

	500 mM Salts / 10% TMOS with thiol						
Time (min)	**10**	**102**	**192**	**292**	**377**	**462**	**548**
Sr^{2+} Ions	no data	97%	48.9%	27.3%	NQ**	NQ	NQ
Celestine	-	0	0.0%	7.9%	18.0%	39.9%	59.7%
Hydrate	-	0	51.1%	64.8%	82.0%	60.1%	37.3%
Hydrate fraction (of solids)	-	N/A	100.00%	89.13%	82.00%	60.10%	38.45%
Unknown standard	-	3.0%	0.0%	0.0%	0.0%	0.0%	3.0%
Best fitting unknown standard	-	$Sr(NO_3)_2$	-	-	-	-	$Sr(OH)_2$
Best χ^2	-	1.6E-04	8.4E-05	8.6E-05	7.3E-05	7.7E-05	6.8E-05
χ^2 improvement considering unknown species	-	2.42%	-	-	-	-	1.03%

* The best fits in this experiment replaced hydrate with $SrCl_2$, $SrAc_2$, and $Sr(OH)_2$ standards at roughly 15-20% concentration. A fit with 1% $Sr(NO_3)_2$ was also marginally better than the fit including only the Sr^{2+} ions and hydrate.

** Non-Quantifiable: assumed to be present in concentration <3%

Better mathematically fits do not necessarily tell the full story. As previously mentioned, fitting to more standards reduces χ^2, but information about fluctuations in the spectrum are lost. This means that while contributions from the unknown species reduce the χ^2, that alone is not a sufficient indication that the fits are representing more accurately the absorbance spectra of the measured system. However, as shown by Figure 14, this is insufficient proof that a particular fit is actually a better representation of the data. Figure 15 shows an example of the fit improvements from Table 3. Specifically, the 55 min measurement from the experiment with the 50 mM diffusing salts and the thiol functionalized gel. In this example, there is a small, but noticeable improvement in the fitting of the first local minimum after the absorption edge (ca. 16140 eV) – a suggestion that the improvements in fit may reflect actual changes in the system.

An additional observation from Table 3 is that there is significantly less measured unknown species in the experiment with 500 mM diffusing salts. In this experiment, both the concentrations found of “unknown” species, and the improvements to the fit quality are minimal (≤3%). In addition, the fits are generally more accurate (lower χ^2) than those for the 50 mM reactants. Finally, in this experiment there is 38% hemihydrate remaining after >9 hours. This can be compared to previous observations from Chapter 2 where the longest surviving example of hemihydrate in solution fully transofrmed into celestine within 5 hours. The relative concentration of hemihydrate mesaured in all XANES experiments where good fits could be found are presented in Figure 16. It can be seen that the persistence of the hemihydrate confined in the hydrogel always exceeded 300 minutes, or the maximal 5 hours required for full transformation in a non-confined environment.

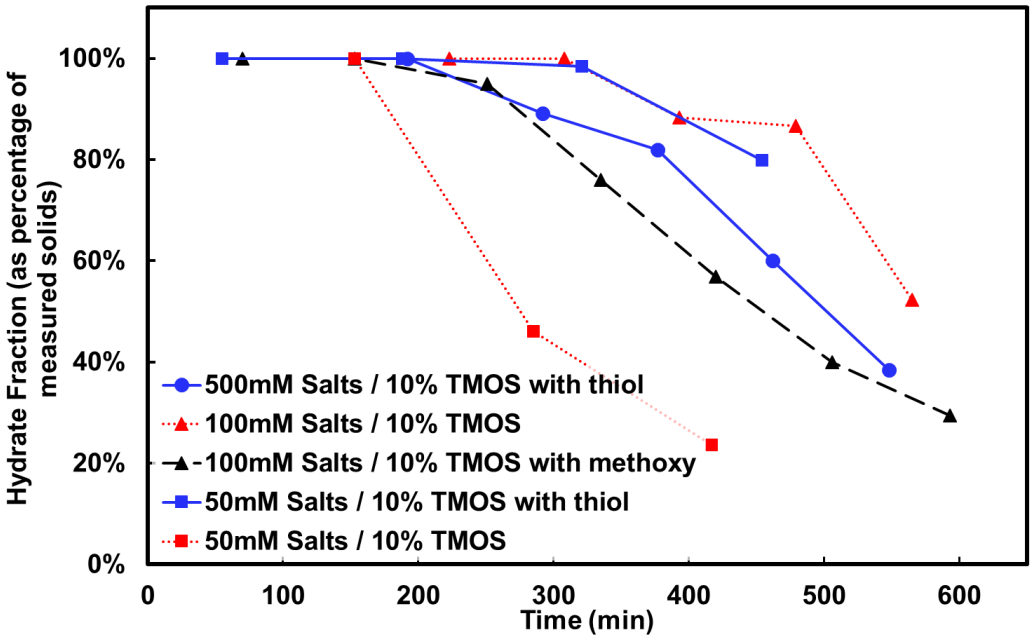

Figure 16: *Hemihydrate concentration (measured as a fraction of total solids, or Celestine + Hemihydrate) during XANES experiments.*

4. Discussion

The results presented in this chapter are numerous, diverse, and speak to a wide range of subjects regarding nucleation, confinement, and the strontium sulfate system. For clarity, the discussion will be divided into three sections. Part I will delve into general effects of confinement on nucleation – focusing on aspects independent from discussions of multistep nucleation and alternative nucleation theories. Part II will center on those concepts of multistep nucleation, particularly how they apply within the strontium sulfate system, and part III will explore the solid strontium sulfate phases and their interaction within the confined system. Finally, in a fourth section, some of the limitations and ideas to improve the experiments are briefly discussed.

Part I: pathway independent effects of confinement

Pore controlled solubility (PCS), as discussed in Figure 9, predicts that starting form a certain size smaller pores require greater supersaturations to drive nucleation. Estimates for $SrSO_4$ in the silica hydrogels used in this work showed that the smallest pores (~16 nm) should require approximately 1.5x the concentration of ions for nucleation to occur when compared to the largest pores (100-200 nm). As diffusion rates are predicted to be driven by pore volume fraction, and not the size of individual pores, we consider that during a counterdiffusion experiment, the total concentration of ions in pores increases at similar rates across pores of all sizes. Consequently, the threshold supersaturation for nucleation should be reached first in the largest pores. The evolution of scattering, as depicted in Figure 7 (and, to a lesser extent Figures 10a and 11), reveals that the initial scattering occurs at the lowest measured q. This q corresponds to the largest distances in real space, suggesting that the likely first nucleation sites are the largest pores. Furthermore, the shape of the invariant vs time curve (Figure 8) demonstrates a rapid increase in one location, followed by a plateau, while remaining constant at all other measured locations. This is consistent with an explanation where nucleation occurs in the largest pores, then continues into smaller and smaller pores until all transport conduits are blocked, halting and diffusive mixing of ions, which is consistent with simulations conducted by other research groups[12].

However, not all experimental results are in agreement with the phenomenon of large pores favoring nucleation over smaller ones. Figure 8 shows that the induction time for nucleation was shortest in experiments with the highest volume fraction of TMOS (which have the smallest pores as shown in Figure 6 and Table 2). This

apparent contradiction becomes even more perplexing when considering the relationship between porosity and diffusion rates. Generally, the higher volume fraction gels, with their correspondingly lower volume fraction pore space, would be expected to have lower diffusion rates compared to lower volume fraction gels[12]. Yet, the gels that would be expected to have the slowest diffusion and require the highest saturation for nucleation to occur resulted in the fastest start of nucleation.

There are several possible explanations for this discrepancy. The simplest of which is that the by-product of the gelification reaction is methanol[54]. While efforts were made to allow this methanol to evaporate before the experiments were conducted (see Materials and Methods), however, should these efforts have been unsuccessful, it would be expected that the highest volume fraction gels would contain the highest concentrations of alcohol – which is known to have lower solubility for most mineral phases[6,55]. Hence, the lowest critical saturations for nucleation might appear in the highest density TMOS gels, or those with the smallest pores as would agree with the trend of short induction times for the system with the smaller pore size overall. An extension of this idea could be that despite the gel being fully formed, it is possible that the TMOS was not fully consumed, leaving trace amounts of TMOS monomer behind as additives. Again, if this were to have occurred, the highest additive effect would likely be found in gels with the highest TMOS concentrations and the smallest pores – this is not to claim that TMOS monomers are catalysts for nucleation, but they may be present and alter the nucleation process in some way. The counterintuitive result seen in Figure 8 where larger pores had slower induction times is not proof that alcohol and TMOS monomer were present in the system during the nucleation reactions, but it does raise the question that such species may have influenced the outcome of the experiments. For the remainder of this chapter, discussion of this possibility of contamination is very limited, but it must always be remembered that unlike the Sr-SO_4-H_2O system discussed in Chapters 1 and 2, these experiments may contain methanol and TMOS additives as well for the results of this chapter.

An alternative explanation for the short induction times observed for gel systems with the smallest average pore size can be found in Equation 9. In a case where there is a strong affinity between the nucleating crystal and the pore wall, it is possible for the contact angle to exceed 90°, with the result of the exponential changing signs due to the presence of the cos(θ) term. This sign change would result in an inverse effect

where the critical saturation for nucleation decreases in smaller pores. This possibility is somewhat supported by the induction times measured in functionalized silica hydrogels. Figure 8 also shows that Methoxy functionalization has a possible small effect of accelerating nucleation, while thiol functionalization has a considerable effect retarding the nucleation within the 10% TMOS gels. Without any further information, it is clear that surface functionality of the pores plays a significant role on nucleation kinetics in this system. This could be in relation to polarity, adsorption rates, stereochemistry, or a number of other effects. Further research is needed to elucidate the nature and mechanisms behind the surface effects. However, it must be stated that this explanation could also predict that the smallest pores in a single experiment would also see nucleation before the larger pores (if diffusion rates and tortuosity don't result in pore size dependent salt concentration), something that was never observed and therefore would need substantial additional analysis to verify.

Another possible consideration for the reasoning behind differences in induction time is the diffusion rate of ions in the silica gels. There was an attempt to measure the diffusion rates by finding the time needed to observe Sr^{2+} ions during the XANES experiments, but ultimately there were too many sources of error (precise size and position of silica gel, low time resolution, low repeatability, and minimal calibration of concentration) to discern if the diffusion rates varied significantly.

Part II: Multi-step nucleation:

Chapter 2 proposed that celestine undergoes a multi-step nucleation pathway. If this hypothesis were accurate, whatever species participate in the intermediate steps may be measurable in XANES. Measurements of slightly supersaturated $SrSO_4$ in solution (shown in Figure 13) did not find any evidence of complexation, at least not different from whatever structures can be found in undersaturated solution or solutions without any SO_4^{2-} ions ($SrCl_2$ solutions). This shows that any extant intermediate structures either occur starting at very low concentrations (<0.5 mM), or do not appear until a nucleation process has begun.

However, the analysis of nucleating solutions shown in Table 3 (and validated in Figure 15) does indicate the presence of species that are not Sr^{2+} ions or known mineral species (celestine or hemihydrate). While XANES can theoretically enable structural predictions, the absorption profile of this unknown species could not be consistently correlated to a single tested analog. The structures of solid $Sr(NO_3)_2$,

$Sr(OH)_2$, and $SrCl_2$ all at some point were shown to be possible analogs, but a more likely explanation is that the unknown species has a structure different from all of the analogs tested. Finally, the detected presence of unknown species (or the inability of the three known standards to fully describe the x-ray absorption behavior) is more pronounced in the slower reactions where more celestine is expected to be formed. In a fast reaction (with 500 mM diffusing salts) where hemihydrate would be expected to form first, little to know unknown species were observed. This is consistent with observations from Chapter 2 where a multi-step reaction was described for the formation of celestine, but not hemihydrate.

Some observation from SAXS experiments also need to be considered in the context of multi-step nucleation, particularly the idea that nuclei could form from the coalescing of nanoparticles. Figure 11 reveals local maxima in the SAXS patterns that are indicative of structure factors and frequently describe arrays of nano-particles. While this could be considered evidence of nano-particle mediated nucleation, the real-space distances characteristic of these structures are far greater than the characteristic structure sizes of the pores, indicating that they are likely representative of spacings between different nuclei, or a quasi-structure formed by multiple growing particles. Such a structure could be formed by ion-depletion zones, where the formation of a nucleus consumes ions locally, creating a relative low concentration zone in the adjacent spaces, impeding further nucleation.

Additionally, the Porod regime slopes shown in Figure 10 should also be considered in this discussion. Diffraction from the TMOS gels have a Porod exponent of -2, indicative of mass fractals or lamellar structures (frequently described as exponents in the range [-2,-3]). Particles with a smooth surface (like spherical classical nuclei) would be expected to have a Porod exponent of -4, and generally the remaining range [-3,-4] is considered to describe surface fractals – which can be thought of as large particles with rough surfaces. The fastest experiments, again where hemihydrate is expected to form, feature exponents of ca. -3.6 immediately upon nucleation and continue to progress towards -4 as further nuclei are formed and grow. This is highly consistent with a single step nucleation pathway where each nucleus forms from a single particle and grows in a sphere or rod shape. However, the slower experiments where there is more celestine expected feature minimum Porod exponents in the -3 to -3.4 range, which could be indicative of mass fractals or crystal masses formed by the

coming together of many smaller units into a single mass with a rough surface. This analysis requires much more extensive analysis to validate, and would benefit massively from larger q-ranges so that more than only the Porod regime could be analyzed and fit to models. However, the above-described explanation is consistent with data from chapter 2 and the XANES experiments, so nano-particle agglomeration is a hypothesis for the intermediate step of celestine nucleation that certainly warrant closer inspection and further research.

Here it is worth noting that the scattering patterns were found by integrating radially and assuming radial symmetry in the SAXS images. It was observed that some of the scattering images taken, like that presented in Figure 17, were not radially symmetric, so some of the observed slopes are the result of the radial integration of an asymmetric signal. This further calls the results described in this paragraph into question, and warrants for further analysis and research.

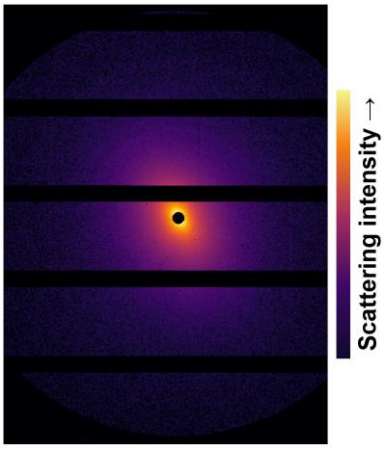

Figure 17: *example assymetric scattering pattern that was observed during SAXS experiments. The horizontal black bars represent the physical gaps between detector panels.*

Part III: Celestine and Hemihydrate

WAXS and XANES results suggest that both phases are present in the majority of counterdiffusion experiments conducted for this chapter. Furthermore, as seen in Figure 16 (and comparing with Figure 7 from Chapter 2) the persistence of the metastable hemihydrate when confined in the hydrogel is far greater than the non-confined case. In the capillary experiment without gel in chapter two revealed that the hemihydrate dissolved “frontally”, such that the dissolution proceeded from the region of highest Sr^{2+} concentration towards the region of highest SO_4^{2-} concentration, as seen by a dissolution front moving right to left across the hemihydrate. Assuming this dissolution front exists in the pores as well, it is likely that this persistence is driven

largely by the reduced rate at which the hemihydrate can be dissolved when ions must be transported via diffusion from the solid through a pore network instead of freely through a solution. However, the possibility of thermodynamic (energy-driven) influences like surface effects was not explored and remains open for further investigation.

Of greater interest is how the precipitating phase is selected during nucleation. Experiments during which lower concentration reactants were diffused in the narrower (1 mm) glass capillaries only celestine formation was observed, where higher reactant concentrations in the same conditions resulted in hemihydrate appearing as well. This suggests that concentration and supersaturation rate were the principal driving factors in hemihydrate formation, as was the case in bulk solution.

Non-quantitively comparisons of the amount of diffraction detected from hemihydrate scattering seen in Figure 12 suggest that the largest amount of hemihydrate was created during the reactions in gel functionalized with thiol, and the second most in 5% TMOS gels. Figure 8 shows that those two gels are the cases with the longest induction times. Applying an assumption of relatively similar diffusion rates would suggest that the critical supersaturation for nucleation was greatest during these reactions where the most hemihydrate was detected. Figure 12 also shows hemihydrate formed gels with 10, 15, and 20% TMOS, but without a clear trend in quantity between the gel densities – however, the induction time differences in these gels was not nearly as significant as those of the 5% and Thiol-functionalized gels (Figure 8). In any case, to verify these observations, more experiments with accurate quantitative capacity would be needed to fully validate these observed trends. If diffusion rates across gel sizes is similar (with correspondingly similar saturation rates at the mixing zone), it suggests that supersaturation, not supersaturation rate, may be the driving force behind phase selection during the nucleation reaction in the SrSO4 system.

This observation raises questions about the precise nature of nucleation reactions. In chapter 1, it was hypothesized that a kinetic slow step can be responsible for some of the observations of intermediate particles in multi-step nucleation. It was further concluded that the transition from two-step celestine formation to single step hydrate formation may result from the fast reaction kinetics (i.e. reduced time for intermediates to form) driven by the lower energy barrier present at high

supersaturations. However, regarding Figures 8 and 12 of this chapter, the experiments featuring the most time before nucleation observed the most single-step nucleation as well. Despite the differences in co-titrations (chapter 1) and the counter-diffusion experiments – particularly how these the counter-diffusions have non-homogenous supersaturation levels, different supersaturation rates, and the possible presence of methanol and TMOS additives – both feature concentrations that increase until the critical supersaturation is reached, and it is reasonable to predict similar trends in both sets of experiments. The discrepancy in results between the chapters opens the door for more discussions about the interplay between kinetics, mechanisms, and the actual time of the nucleation process.

An important caveat is that here we consider “induction time” and the “the time allowed for the reaction” to be the same thing. However, in the capillary counterdiffusion system, induction time considers both the diffusion time and the time spent in a supersaturated state. One already discussed possible explanation for the relationship between pore size and induction time is variance in diffusion rate, it is possible that a longer “induction time” for nucleation in these experiments is indicative of a case where diffusion was slower and the time spent supersaturated was actually the same or even less. This is an unlikely explanation due to the fact that this could suggest hemihydrate being formed at similar or even lower supersaturations than celestine, which is not considered probable based on the results of Chapter 2. However, without improved diffusion rate and critical supersaturation measurements, this explanation cannot be fully discounted.

More likely, the hemihydrate forms most readily in the systems that achieve high supersaturations before nucleation – be that because of fast diffusion in the case of high reactant concentrations or pore-mediated suppression of nucleation that allows for supersaturation to increase higher in certain conditions due to surface effects and/or additive presence. This suggests that supersaturation itself, and not the rate at which it is achieved is the critical variable in phase selection during nucleation. This is in agreement with observations in Chapter 2 where the threshold supersaturation for the formation of hemihydrate was ca. 10 mM regardless of how that supersaturation was achieved (direct mixing or co-titration). However, only under confinement conditions is a case where longer experimental time is needed to achieve the higher supersaturation.

This raises some questions about the proposed nucleation mechanisms from Chapter 1. There, the idea of a nucleation "slow-step" driving the appearance of particle mediated nucleation in celestine (it is not a "slow-step" as defined for multi-step reactions as there is no thermodynamic stopping point between the steps, instead it is a region of relatively slow kinetics on the continuum of transformation), but the fast rate of hydrate formation in effect bypassing that step to find an alternate solid phase does not necessarily fit with finding more hemihydrate in longer induction time experiments. One way to find agreement in these results is to consider the nucleation reaction as separate from the time spent supersaturated during induction. Put simply, this would suggest that the random fluctuations of the system before nucleation are kinetically independent of the nucleation step itself.

Part IV: Experimental limitations and possible improvements

The above analysis was conducted to the fullest extent possible given the limitations and quality of the collected data. The majority of the SAXS data featured a *q* range limited to only the Porod regime post-nucleation. Experiments with a wider *q* range often had an unresolved background peak that could not be removed (Figure 7, at $q=4*10^{-7}$), making accurate fitting of data to mathematical models for particle size and shape challenging. WAXS, without controlling grain orientations, is inherently a non-quantitative technique, and XANES is limited in time resolution to the point that individual scans are likely significantly longer than nucleation reactions, potentially losing finer details to time-averaging. Given that the majority of scattering during early nucleation occurred at low *q* (Figures 7 and 11), future investigations should focus on this lower *q* range. Additionally, discussions with Elettra beamline staff revealed that technology for dramatically improved time resolution in XANES should be available in the near future (if not already at the time of presentation of this dissertation).

Finally, the gels themselves warrant a significantly expanded examination and characterization. First, the concerns about the possible presence of alcohol or TMOS monomers during experiments must be addressed before any future experiments in a similar system. Additionally, exploration of steps to ensure strong adhesion between the gels and capillary walls – such as functionalization or the use of smaller diameter capillaries – would be beneficial. It is also worth considering a procedure where gels are grown in an open bulk environment for easy characterization (for properties like surface functionalization and specific adsorption)[†] and cleaning. Only after that would

they be fitted and inserted into a capillary, potentially providing greater experimental control.

†Experiments attempting to probe these properties were attempted, but the results obtained proved inconclusive within the time available. More details and discussion can be found in the prospectus.

5. Concluding Remarks

The nucleation of strontium sulfate under confined conditions was observed through a series of counterdiffusion experiments using silica hydrogel with a variety of pore sizes in the nanometer range. The precipitation reactions were observed with SAXS, WAXS, and XANES to observe the sizes, locations, and structures of precipitates as they formed.

As with experiments in bulk solution, higher reactant concentration resulted in the formation of the metastable hemihydrate phase, and the pores had a stabilizing effect on this transient phase resulting in specimens surviving aqueous environments far longer than any observations made in non-confined experiments.

In the exploration of multi-step nucleation, the XANES data agree with the findings of chapter 2 in which two-step nucleation is predicted for celestine, but not for the metastable hemihydrate – shown by how the experiments with the most celestine present during nucleation required the consideration of nucleation precursors to fully model the absorption edge.

Additionally, in any individual experiment with silica (-OH), thiol (-SH), and methoxy (C-O-C) surface functionalities nucleation occurred in the largest pores first, progressing into smaller and smaller pores as limited by open transport networks for continued ion diffusion. The thiol surface functionality also demonstrated a significant elongation of the induction time for nucleation relative to the other surfaces.

Despite the preference for nucleation to occur in large pores in individual experiments, a seemingly inverse result was observed where the induction times for nucleation scaled inversely with average pore size. The exact causes of this are yet unknown, but the apparent greater amount of hemihydrate observed in the longer induction time, open an interesting conversation regarding how much of the induction time “participates” in the nucleation reaction.

Overall, the results obtained from these experiments raise interesting questions about the nature of nucleation and the effects of confinement, warranting further

examination and research. However, confirming the hypotheses suggested by these data would require additional development and exploration of these experiments and similar ones. Importantly, these experiments demonstrate the promise that confined counter-diffusion experiments show for examining nucleation (and the effects of confinement) in mineral systems considering the dynamic nature of the experiments (resembling real world conditions) and the ability to simultaneously probe a variety of conditions and their interactions.

References

1 B. W. D. Yardley and K. I. Shmulovich, in *Fluids in the Crust*, Springer Netherlands, 1994, pp. 1–12.

2 D. G. Fahrenheit, *Philos. Trans. R. Soc. London*, 1724, **33**, 1–3.

3 *Nature*, 1929, **124**, 119–120.

4 M. Volmer and A. Weber, *Zeitschrift für Phys. Chemie*.

5 A. G. Walton, *Microchim. Acta*, , DOI:10.1007/BF01217569.

6 B. V. Enüstün and J. Turkevich, *J. Am. Chem. Soc.*, , DOI:10.1021/ja01502a015.

7 D. H. Klein and J. A. Driy, *Talanta*, , DOI:10.1016/0039-9140(66)80037-1.

8 B. Lambert and W. Hume-Rothery, *J. Chem. Soc.*, 1926, **129**, 2637–2648.

9 M. J. Bickle, *Nat. Geosci.*, 2009, **2**, 815–818.

10 C. I. Steefel and A. C. Lasaga, *Am. J. Sci.*, 1994, **294**, 529–592.

11 C. I. Steefel and P. C. Lichtner, *Geochim. Cosmochim. Acta*, 1994, **58**, 3595–3612.

12 H. Deng, C. Tournassat, S. Molins, F. Claret and C. I. Steefel, *Water Resour. Res.*, , DOI:10.1029/2020WR028483.

13 S. Emmanuel and B. Berkowitz, *Adv. Water Resour.*, 2005, **28**, 337–344.

14 L. Griffiths, M. J. Heap, F. Wang, D. Daval, H. A. Gilg, P. Baud, J. Schmittbuhl and A. Genter, *Geothermics*, 2016, **64**, 235–245.

15 H. M. Ezuber, *J. ASTM Int.*, , DOI:10.1520/JAI100958.

16 J. C. Lindlof and K. G. Stoffer, *JPT, J. Pet. Technol.*, 1983, **35**, 1256–1262.

17 A. N. Paukert Vankeuren, J. A. Hakala, K. Jarvis and J. E. Moore, *Environ. Sci. Technol.*, 2017, **51**, 9391–9402.

18 A. Rahardianto, B. C. Mccool and Y. Cohen, *Environ. Sci. Technol.*, 2008, **42**, 4292–4297.

19 K. E. Wright, T. Hartmann and Y. Fujita, *Geochem. Trans.*, 2011, **12**, 8.

20 H. Chen and E. Park, *Environ. Earth Sci.*, 2017, **76**, 1–8.

21 R. M. Espinosa-Marzal and G. W. Scherer, *Acc. Chem. Res.*, 2010, **43**, 897–905.

22 I. Sass and U. Burbaum, *Acta Carsologica*, 2010, **39**, 233–245.

23 R. J. Flatt, F. Caruso, A. M. A. Sanchez and G. W. Scherer, *Nat. Commun.*, 2014, **5**, 1–5.

24 F. Kohler, O. Pierre-Louis and D. K. Dysthe, *Nat. Commun.*, 2022, **13**, 1–8.

25 H. Ping, H. Xie, Y. Wan, Z. Zhang, J. Zhang, M. Xiang, J. Xie, H. Wang, W. Wang and Z. Fu, *J. Mater. Chem. B*, 2016, **4**, 880.

26 E. Beniash, J. Aizenberg, L. Addadi and S. Weiner, *Proc. R. Soc. B Biol. Sci.*, , DOI:10.1098/rspb.1997.0066.

27 M. Albéric, E. Zolotoyabko, O. Spaeker, C. Li, M. Tadayon, C. N. Z. Schmitt, Y. Politi, L. Bertinetti and P. Fratzl, *Cryst. Growth Des.*, 2022, **22**, 3727–3739.

28 M. Zeng, Y. Y. Kim, C. Anduix-Canto, C. Frontera, D. Laundy, N. Kapur, H. K. Christenson and F. C. Meldrum, *Proc. Natl. Acad. Sci. U. S. A.*, 2018, **115**, 7670–7675.

29 S. Emmanuel and B. Berkowitz, *Geophys. Res. Lett.*, , DOI:10.1029/2006GL028962.

30 L. A. Rijniers, H. P. Huinink, L. Pel and K. Kopinga, *Phys. Rev. Lett.*, , DOI:10.1103/PhysRevLett.94.075503.

31 A. Putnis and G. Mauthe, *Geofluids*, 2001, **1**, 37–41.

32 Godinho, Ma, Chai, Storm and Burnett, *Minerals*, 2019, **9**, 480.

33 S. Emmanuel and J. J. Ague, *Water Resour. Res.*, , DOI:10.1029/2008WR007170.

34 A. G. Stack, A. Fernandez-Martinez, L. F. Allard, J. J. Bañ, G. Rother, L. M. Anovitz, D. R. Cole and G. A. Waychunas, , DOI:10.1021/es405574a.

35 G. Hoareau, C. Monnin and F. Odonne, *Geochim. Cosmochim. Acta*, , DOI:10.1016/j.gca.2010.03.033.

36 S. Takahashi, M. Seki and K. Setoyama, *Bull. Chem. Soc. Jpn.*, 1993, **66**, 2219–2224.

37 A. R. Lauer, R. Hellmann, G. Montes-Hernandez, N. Findling, W. L. Ling, T. Epicier, A. Fernandez-Martinez and A. E. S. Van Driessche, *J. Chem. Phys.*, , DOI:10.1063/5.0136870.

38 A. E. S. Van Driessche, T. M. Stawski and M. Kellermeier, *Chem. Geol.*, 2019, 530, 119274.

39 A. R. Lauer, M. A. Durán-Olivencia, A. Fernandez-Martinez and A. E. S. Van Driessche, *Faraday Discuss.*, 2022, **235**, 95–108.

40 A. E. S. Van Driessche, M. Kellermeier, L. G. Benning and D. Gebauer, *New Perspectives on Mineral Nucleation and Growth: From Solution Precursors to Solid Materials*, 2017.

41 B. Cabane, M. Dubois, F. Lefaucheux and M. C. Robert, *J. Non. Cryst. Solids*, 1990, **119**, 121–131.

42 J. E. Martin and A. J. Hurd, *J. Appl. Crystallogr.*, 1987, **20**, 61–78.

43 C. D. Putnam, *J. Appl. Crystallogr.*, 2016, **49**, 1412–1419.

44 G. Beaucage, *J. Appl. Crystallogr.*, 1996, **29**, 134–146.

45 A. Lauer, R. Hellmann, A. Fernandez-Marinez, N. Findling, T. Epicier, W. L. Ling, G. Montes-Hernandez and A. E. S. Van Driessche, .

46 O. Proux, X. Biquard, E. Lahera, J. J. Menthonnex, A. Prat, O. Ulrich, Y. Soldo, P. Trévisson, G. Kapoujyan, G. Perroux, P. Taunier, D. Grand, P. Jeantet, M. Deleglise, J. P. Roux and J. L. Hazemann, *Phys. Scr. T*, 2005, **T115**, 970–973.

47 U. Marini, B. Marconi, A. Petri, A. Di Cicco, M. J. Rosolen, R. Marassi, G. Aquilanti, M. Minicucci, E. Principi, N. Novello, A. Cognigni and L. Olivi, *J. Phys. Conf. Ser*, 2009, **190**, 12043.

48 B. Ravel and M. Newville, in *Journal of Synchrotron Radiation*, International Union of Crystallography, 2005, vol. 12, pp. 537–541.

49 R. Koningsberger, D C; Prins, *X-ray absorption: Principles, applications, techniques of EXAFS, SEXAFS and XANES*, 1987.

50 G. W. Scherer, *Cem. Concr. Res.*, 2004, **34**, 1613–1624.

51 S. He, J. E. Oddo and M. B. Tomson, *J. Colloid Interface Sci.*, , DOI:10.1006/jcis.1995.1398.

52 R. K. Mishra, K. Kanhaiya, J. J. Winetrout, R. J. Flatt and H. Heinz, *Cem. Concr. Res.*, 2021, **139**, 106262.

53 F. C. Meldrum and C. O'Shaughnessy, *Adv. Mater.*, 2020, **32**, 2001068.

54 B. Shi, L. Xie, B. Ma, Z. Zhou, B. Xu and L. Qu, *Gels*, 2022, **8**, 744.

55 S. P. Pinho and E. A. Macedo, *J. Chem. Eng. Data*, 2005, **50**, 29–32.

56 K. Momma and F. Izumi, *J. Appl. Crystallogr.*, 2011, **44**, 1272–1276.

57 B. R. W J ames and W. A. W ood, *Proc. R. Soc. London. Ser. A, Contain. Pap. a Math. Phys. Character*, 1925, **109**, 598–620.

58 W. Abriel and R. Nesper, *Zeitschrift fur Krist.*, 1995, **205**, 99–113.

59 R. Becker and W. Döring, *Ann. Phys.*, 1935, **416**, 719–752.

60 D. Gebauer, A. Völkel and H. Cölfen, *Science (80-.).*, , DOI:10.1126/science.1164271.

61 M. Sleutel, J. Lutsko, A. E. S. Van Driessche, M. A. Durán-Olivencia and D. Maes, *Nat. Commun.*, 2014, **5**, 1–8.

62 M. A. Durán-Olivencia and F. Otálora, *J. Cryst. Growth*, 2013, **380**, 247–255.

63 A. Fick, *Ann. Phys.*, 1855, **170**, 59–86.

Supplement A: Beam information

ALBA SAXS – Example File Header:

{
HeaderID = EH:000001:000000:000000 ;
ByteOrder = LowByteFirst ;
DataType = SignedInteger ;
Size = 4092732 ;
Dim_1 = 981 ;
Dim_2 = 1043 ;
Image = 0 ;
acq_frame_nb = 1 ;
time = Thu Apr 15 11:10:02 2021 ;
time_of_day = 1618477802.645509 ;
time_of_frame = -12345678901234567168.000000 ;
Monitor = 93600.0 ;
MonitorRing = 124.870 ;
Photo = 275 ;
Pilatus = /beamlines/bl11/projects/cycle2021-I/2020094679-alauer/DATA/temp/pilatus_A00_000_0001.edf ;
Rayonix = /beamlines/bl11/projects/cycle2021-I/2020094679-alauer/DATA/temp/rayonix_A00_000_0001.edf ;
acq_autoexpo_mode = OFF ;
acq_expo_time = 0.5 ;
acq_latency_time = 0.105 ;
acq_mode = Single ;
acq_nb_frames = 10 ;
acq_trigger_mode = ExtGate ;
att1 = 72.000 ;
att2 = 72.000 ;
auxstage = 104.600 ;
bs0x = 48.087 ;
bs1_alpha = -247.601 ;
bs1_beta = 33.768 ;
bs2x = 62.938 ;
bs2z = 0.001 ;
current = 249.73974597013444 ;
det_x = -96.581 ;
det_z = -46.553 ;
energy_bragg = 12.402 ;
exposure = 0.5 ;
ft_length = 6530.0 ;
ft_xdown = -71.681 ;
ft_xup = -11.244 ;
ft_zdown = -64.796 ;
ft_zup = -12.368 ;
image_bin = <1x1> ;
image_flip = <flip x : False,flip y : False> ;
image_roi = <0,0>-<981x1043> ;
image_rotation = Rotation_0 ;
pt_no = 1 ;
spitch = 0.120 ;
sroll = 0.690 ;
stz = -40.200 ;
sx = 2.640 ;

syaw = 0.000 ;
sz = 12.320 ;
tfg_ch1 = 93600 ;
tfg_ch2 = 129 ;
tfg_ch3 = 275 ;
tfg_ch4 = 133 ;
tfg_ch5 = 0 ;
tfg_ch6 = 0 ;
tfg_ch7 = 0 ;
tfg_ch8 = 0 ;
waxs_x = 127.000 ;
waxs_z = 46.939 ;

ALBA WAXS – Example File Header:

== pyFAI calibration ==
Distance Sample to Detector: 0.118365048916 m
PONI: 1.835e-01, 4.472e-02 m
Rotations: -0.013731 0.510766 0.000001 rad
#
== Fit2d calibration ==
Distance Sample-beamCenter: 135.695 mm
Center: x=523.405, y=2821.331 pix
Tilt: 29.274 deg TiltPlanRot: 88.596 deg
#
Detector Rayonix LX255 PixelSize= 8.854e-05, 8.854e-05 m
Detector has a mask: True
Detector has a dark current: False
detector has a flat field: False
#
Wavelength: 9.998725596484449e-11 m
Mask applied: provided
Dark current applied: False
Flat field applied: False
Polarization factor: 0.99
Normalization factor: 1
--> /beamlines/bl11/projects/cycle2021-I/2020094679-alauer/DATA/20210415_WaterDiffusionReference/rayonix_10pctTMOS_pos2_004_0000.dat

ALBA SAXS/WAXS – Example Experimental Header File:

Thu Apr 15 14:43:18 2021
SaxsWaxs /beamlines/bl11/projects/cycle2021-I/2020094679-alauer/DATA/20210415_WaterDiffusionReference 10pctTMOS_pos1_004_ 1 0.5 5.0 0.105
base_dir: /beamlines/bl11/projects/cycle2021-I/2020094679-alauer/DATA/20210415_WaterDiffusionReference
experiment: SaxsWaxs
exposure: 5.0
frames: 1
groups: ['8', '1', '', '', '1 0.500000 5.000000 0 15 0 0', '-1 0 0 0 0 0 0']
latency: 0.105
offset: 0.5
prefix: 10pctTMOS_pos1_004_

```
# pilatus    rayonix  Counter0    Counter1    Counter2    Counter3    Counter4
    Counter5    Counter6    Counter7    Texp(10ns)    current  force  linkam
    ndac_ch1    uxtimer
pilatus_10pctTMOS_pos1_004_0000.edf    rayonix_10pctTMOS_pos1_004_0000.edf  928944  1283
    10312  1329  0  0  0  0  499999996  251.11078100276893
    None  None  None  5.0
```

ALBA SAXS – Poni File:

```
# Nota: C-Order, 1 refers to the Y axis, 2 to the X axis
# Calibration done at Thu Apr 15 12:34:38 2021
poni_version: 2
Detector: Pilatus1M
Detector_config: {}
Distance: 6.7
Poni1: 0.00647284112442
Poni2: 0.162398043477
Rot1: 0.0
Rot2: 0.0
Rot3: 0.0
Wavelength: 9.998725596484449e-11
```

ALBA WAXS – Poni File:

```
# Nota: C-Order, 1 refers to the Y axis, 2 to the X axis
# Calibration done at Thu Apr 15 12:27:39 2021
poni_version: 2
Detector: RayonixLx255
Detector_config: {"pixel1": 8.85417e-05, "pixel2": 8.85417e-05}
Distance: 0.118365048916
Poni1: 0.183471644088
Poni2: 0.0447178036779
Rot1: -0.0137309255007
Rot2: 0.510765641958
Rot3: 1.31647863242e-06
Wavelength: 9.998725596484449e-11
```

ESRF SAXS – Example File Header:

```
{
HeaderID      = EH:000015:000000:000000 ;
VersionNumber = 1 ;
Image         = 1 ;
ByteOrder     = LowByteFirst ;
DataType      = SignedLong ;
Dim_1         = 576 ;
Dim_2         = 958 ;
Size          = 2207232 ;
S70 ITHL offset =   ;
WOS ITHL offset = 0 ;
D5 ITHL offset = 0 ;
S70 config Name =   ;
WOS config Name = 8kev_fast_20210313 ;
D5 config Name = 8kev_fast_20210313 ;
sample Name    = 0 ;
Epoch         = 1637224884.5216460228 ;
config_name    = 0 ;
det_sample_dist = 0 ;
y_beam        = 0 ;
x_beam        = 0 ;
Lambda        = 0.789708 ;
offset        = 0 ;
count_time     = 1 ;
point_no      = 3 ;
scan_no       = 1 ;
preset        = 0 ;
col_end       = 1153 ;
col_beg       = 0 ;
row_end       = 597 ;
row_beg       = 0 ;
counter_pos    = 1 0 151162 0 1.91792e+06 195.354 0 0 15.7 15.7 58 3.20888e+07 0 0 0 0 0 0 0 0 22.1
909825 0 0.00061037 3276.7 ;
counter_mne    = sec pm0 pm1 pm2 vct4 Imach pseudoC pfoil Emono Ecod img roi1 roi2 roi3 roi4 roi5
pico1 pico2 pico3 pico4 hutch d0_cps adc adc2 temp ;
motor_pos      = 170.8 -6 -36.3071 0.75 -0.45 7.158 401.62 9216.13 15.8784 -58.3686 7.23466 26.2547 -
0.499077 -0.328 -1.19153 0.533939 -158.049 -5.8695 -2.14925 44.9559 37.8905 8.01875 1.86013 -82.8464
-3.53262 ;
motor_mne      = xsamp zsamp rsamp XstoP ZstoP Xdet Zdet xwos ywos zwos mono inc1 gamma courb
courbb courbf rien su8 sd8 sf8 sb8 vg8 vo8 hg8 ho8 ;
suffix        = .edf ;
prefix        = 21Nov18WOS_ ;
dir           = /users/opd02/raw ;
run           = 58 ;
title         = CCD Image ;
```

ESRF WAXS – Example File Header:

```
{
HeaderID      = EH:000482:000000:000000 ;
VersionNumber = 1 ;
Image         = 1 ;
```

ByteOrder = LowByteFirst ;
DataType = SignedLong ;
Dim_1 = 1154 ;
Dim_2 = 598 ;
Size = 2760368 ;
S70 ITHL offset = ;
WOS ITHL offset = 0 ;
D5 ITHL offset = 0 ;
S70 config Name = ;
WOS config Name = 8kev_fast_20210313 ;
D5 config Name = 8kev_fast_20210313 ;
sample Name = 0 ;
Epoch = 1637228853.3675990105 ;
config_name = 0 ;
det_sample_dist = 0 ;
y_beam = 0 ;
x_beam = 0 ;
Lambda = 0.789708 ;
offset = 0 ;
count_time = 0.1 ;
point_no = 0 ;
scan_no = 14 ;
preset = 0 ;
col_end = 1153 ;
col_beg = 0 ;
row_end = 597 ;
row_beg = 0 ;
counter_pos = 0.100001 0 1297 0 190873 194.563 0 2 15.7 15.7 291 228167 -3992 228167 0 0 0 0 0 0 21.8 90062.3 0 0 3276.7 ;
counter_mne = sec pm0 pm1 pm2 vct4 Imach pseudoC pfoil Emono Ecod img roi1 roi2 roi3 roi4 roi5 pico1 pico2 pico3 pico4 hutch d0_cps adc adc2 temp ;
motor_pos = 160.7 -6 -36.3071 0.75 -0.45 7.158 401.62 9216.13 15.8784 -58.3686 7.23466 26.2547 -0.499077 -0.328 -1.19153 0.533939 -158.049 -5.8695 -2.14925 44.9559 37.8905 8.01875 1.86013 -82.8464 -3.53262 ;
motor_mne = xsamp zsamp rsamp XstoP ZstoP Xdet Zdet xwos ywos zwos mono inc1 gamma courb courbb courbf rien su8 sd8 sf8 sb8 vg8 vo8 hg8 ho8 ;
suffix = .edf ;
prefix = 21Nov18WOS_ ;
dir = /users/opd02/raw ;
run = 291 ;
title = CCD Image ;

ESRF SAXS – Poni File:

Nota: C-Order, 1 refers to the Y axis, 2 to the X axis
Calibration done at Thu Nov 18 15:32:18 2021
poni_version: 2
Detector: NexusDetector
Detector_config: {"filename": "/Users/lauera/Documents/SAXS/ESRF/ReferenceFiles/SCRIPTS/PYFAI/geomD5_V1/D5_Geom_V1-2.h5"}
#Distance: 3.4902496596704577

Distance: 3.590015775
Poni1: 0.088729458943
Poni2: 0.03915243713076214
Rot1: 0.0
Rot2: 0.0
Rot3: 0.0
Wavelength: 7.897082702751609e-11

ESRF WAXS – Poni File:

Nota: C-Order, 1 refers to the Y axis, 2 to the X axis
Calibration done at Thu Nov 18 11:18:57 2021
poni_version: 2
Detector: NexusDetector
Detector_config: {"filename": "/Users/lauera/Documents/SAXS/ESRF/ReferenceFiles/SCRIPTS/PYFAI/geomWOS_V1/WOS_Geom_V1-2.h5"}
Distance: 0.13045844117157282
Poni1: 0.06784990101581144
Poni2: 0.08953398391147975
Rot1: -0.0008301188022412832
Rot2: 0.002345743323626343
Rot3: -1.7468185942107182e-07
Wavelength: 7.897082702751609e-11

ESRF XANES – Example File Header:

```
#S 680  Escan 16 16.35 232 0
#D Mon Oct 04 03:24:57 2021
#T 0  (Seconds)
#G0 0
#G1 0 0 0 0 0 0 0 0 0 0 0 0 0 0 0 0 0 0 0 0 0 0 0 0 0 0 0 0 0 0 0 0 0 0 0 0
#G2 0
#Q
#P0 11.6455 0.00834638 -0.25 2.75 0.135 2.9325 26.4187 23.5813
#P1 12.0758 -8.51175 20.2138 2.5 -1.5 3.0675 50 -1.39875
#P2 1.41875 3.564 10.2937 -10.4436 2.26389 0.229825 0.997125 1.19982
#P3 1.09847 7 875.793 17.0337 22.9663 40 -2.96625 0.2912
#P4 3.10014 0 60 54.1338 3.10006 217.002 5
#P5 -1.45119 1.5 1.54138 5 -0.854268 1.5 1.38325 5
#P6 1.57633 1.5 1.41369 5 0.619388 1.5 1.16747 3.79074
#P7 -1.7775 1.00662 0.261504 -18.5063 1.5 0 6 0
#P8 375 0 0 0 0 0
#P9 16 0 0 0 0 0 0 0
#P10 50 0 51.2 0 0 0 0 0
#P11 0 0 0 0 0 0 0 0
#P12 0 0 0 0 0 0 0 0
#P13 0 0 0 0 0 86.04 10.9209
#CXDI XDI/1.0 SPEC
#CXDI Scan.edge_energy: 16105.0
#CXDI Mono.name: Si 220
#CXDI Mono.d_spacing: 1.92004
#CXDI Beamline.name: BM30B/FAME
#XDIC Beamline.focusing:yes
#CXDI Beamline.harmonic_rejection: rhodium-coated mirror at 3.1 mrad
#CXDI Facility.name: ESRF
#CXDI Facility.energy: 6.00 GeV
#CXDI Facility.xray_source: Bending Magnet
#CXDI Facility.current: 0.00 mA
#CXDI Facility.mode:
#CXDI Detector.I0: diodes measuring x-rays scattered by air
#CXDI absT1: log(Monitor/I1)
#CXDI absT2: log(I1/I2)
#CXDI absF1: canb/Monitor
#CXDI absF2: I1/Monitor
#C _ESTART _ESTOP _c10 _c11 _c20 _c21 _c30 _c31 _c40 _c41 _SLEEP_FOC DSAMPLE
#C 15.498 16 0.95218 0.997581 1.15487 1.20027 0.222905 0.229892 2.46922 2.26389 0 50.065
#C [fixed ouput: no] [sagittal focusing: yes] [move EXAFS table: no] [gap offset=-2.1] [move tilt: no]
#C           1         2         s         3         k         4
#C E(keV)   16.0000   16.0500   16.1050   16.2200   16.2200   16.3500
#C k(A-1)      -         -         0       5.5204    5.5204    8.0576
#C Nbr pts             11                  170          0        51
#CO 993201 1003965 1016431 Monitor I1 I2
```

Elettra XANES – Parameter File:

```
Absorption Edge (eV) =        16105.00
eV after Edge (eV) =   30.00
```

Start energy (eV) Ei = 16000.00
End energy (eV) Ef = 16400.01
Pre-Edge energy step (eV) = 5.00
Minimum energy step (eV) = 0.40
k constant step (A^-1) = 0.04
Gaf1 = 13.00
Gaf2 = 5.00
Gamma = 3.25
Integration time:
tmin (s) = 1.00
k min (A^-1) = 3.00
t(kmax) (s) = 10.00
t = 1.000000 => index = 0
FileName = r5d7s48
Mode = 0
Rocking Curve = N
Detuning = 0.000000
Fluo Time Mode = Realtime mode
ROI min = 0
ROI max = 0
NORMAL 0
;;; mode = 0

Elettra XANES – Example File Header:

Project Name: Lauer20210272_0
Folder Name: Data_0
File Name: InSitu4_100mM_25pctTMOS_spot1_002.txt
Data and Time: Wednesday, 8 December, 2021 17:06:13
Ring energy (GeV) = 2.4
Ring current (mA) = 129.4
Slits V GAP (mm) = 0.500
Slits V CENTER (mm) = 0.100
Slits H GAP (mm) = 1.500
Slits H CENTER (mm) = 3.650
Table Vertical (mm) = 0.00
Theta ref. position (deg) = 80.00
Huber X (mm) = 0.00
Huber Y (mm) = 0.00
Huber Z (mm) = -6.50
Huber Theta (mm) = -0.00
Vertical ref. position (mm) = 45.50
MultiSample position (mm) = 116.17
Picoam I0 gain = 10^^
Picoam I1 gain = 10^^
Picoam I2 gain = 10^^
Monochromator Crystal: Si 111
Monochromator Energy (eV)= 16400.75
Auxiliary Equipment= NORMAL
Optional Parameters= ;;;

Supplement B: ALBA SAXS/WAXS Data

Presented here is a summary of the SAXS and WAXS data taken from the experiments at ALBA BL11-NCD with minimal post-processing. The capillaries used in these experiments were glass with a 1 mm inner diameter. Each page represents three experiments run simultaneously, and each column on the page is the data from a single capillary. Each figure title contains the gel details, concentration and functionality, as well as a position (pos) number that indicates which scanning point along the length of the gel is presented. The position chosen always represents the one where the most nucleation occurred.

The first row presents the raw integrated SAXS scattering patterns, while the second displays the change in scattering from the time point t=0 (theoretically the scattering from particle formation only). Below that is the raw integrated WAXS pattern followed by the WAXS data background subtracted. For the background subtracted WAXS patterns, the baseline is offset for clarity, and moving up the y-axis represents moving forward in time of the experiment. The fifth row is an attempt to track height of the unique celestine (blue) and hemihydrate (red) peaks as described in the methods section of the chapter. In the legends are the scan numbers – (eg. 002 would represent the second scan taken during the experiment). A visual summary of the above description is presented in Table S1.

Table S1: *visual description of data layout for ALBA SAXS/WAXS data*

Capillary 1	Capillary 2	Capillary 3
Raw integrated SAXS	Raw integrated SAXS	Raw integrated SAXS
Change in SAXS from precipitation reaction	Change in SAXS from precipitation reaction	Change in SAXS from precipitation reaction
Raw integrated WAXS	Raw integrated WAXS	Raw integrated WAXS
Background subtracted WAXS	Background subtracted WAXS	Background subtracted WAXS
Unique peak height sum for Celestine and Hemihydrate	Unique peak height sum for Celestine and Hemihydrate	Unique peak height sum for Celestine and Hemihydrate

100mM solutions

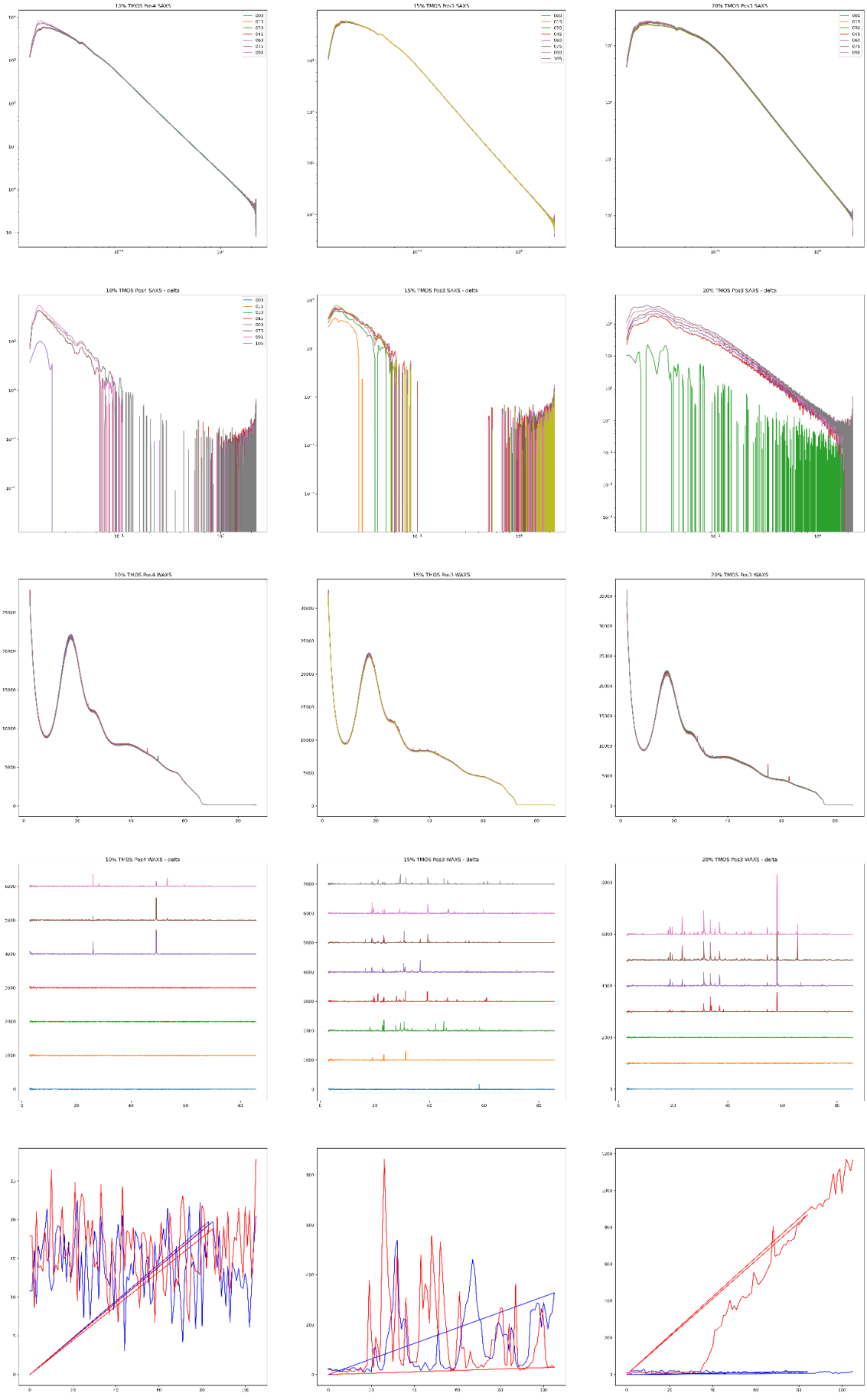

100mM solutions

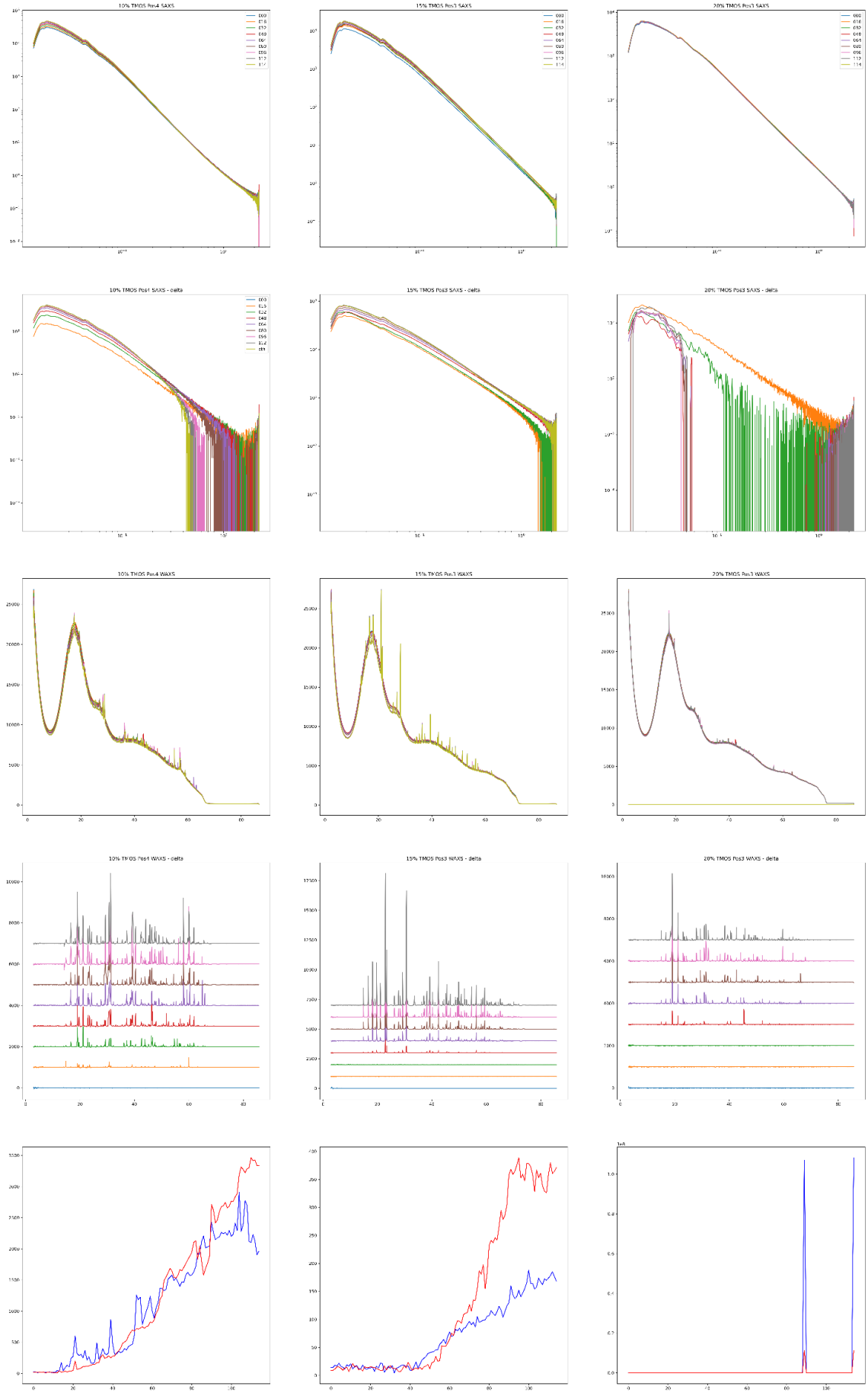

500mM solutions

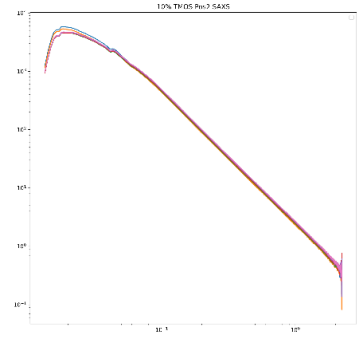

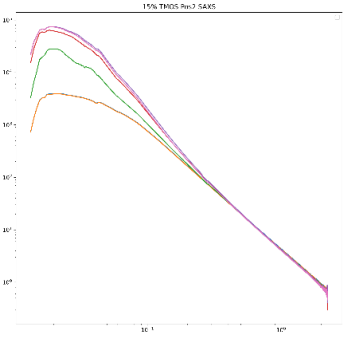

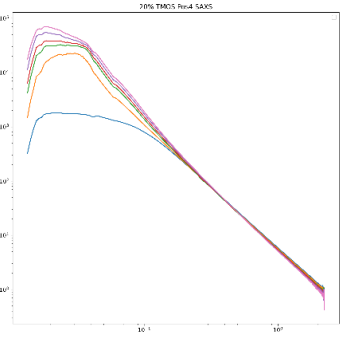

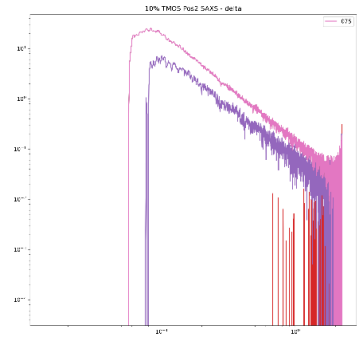

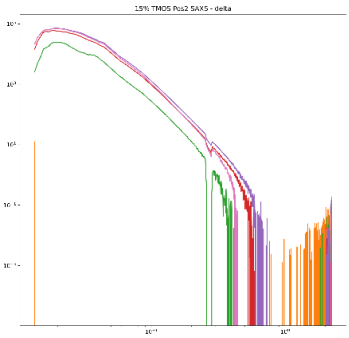

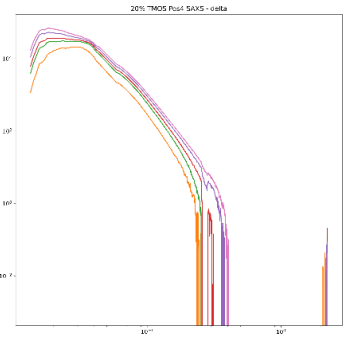

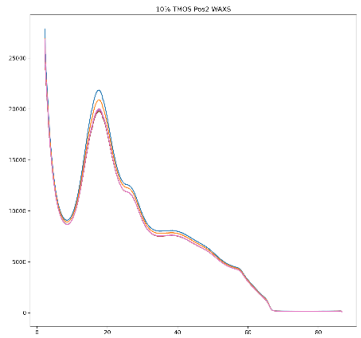

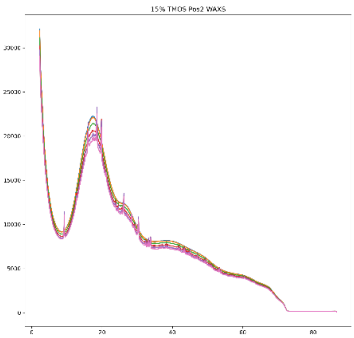

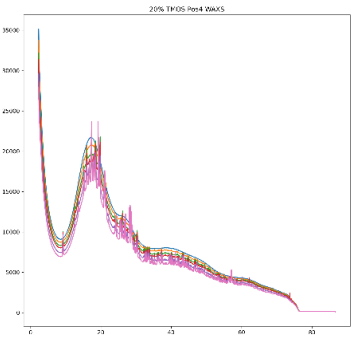

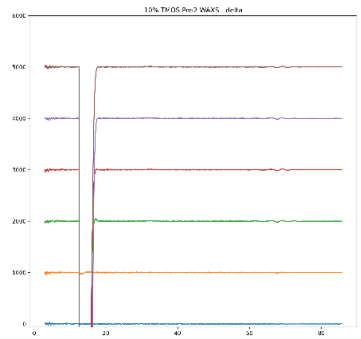

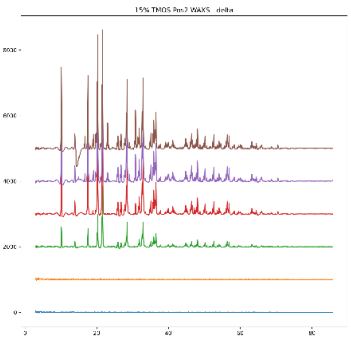

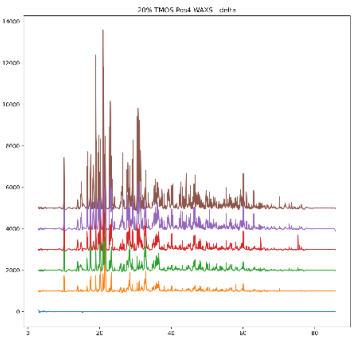

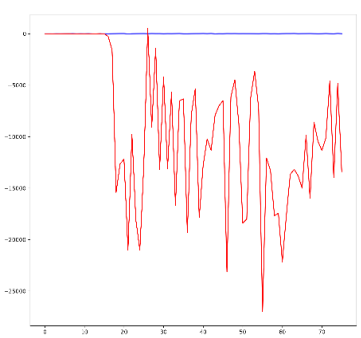

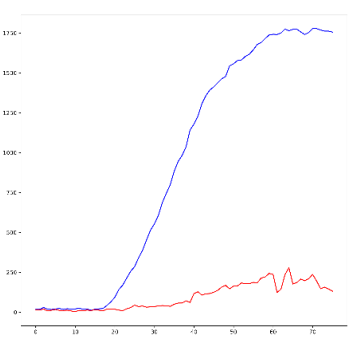

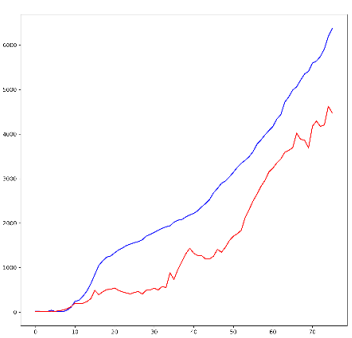

500mM solutions

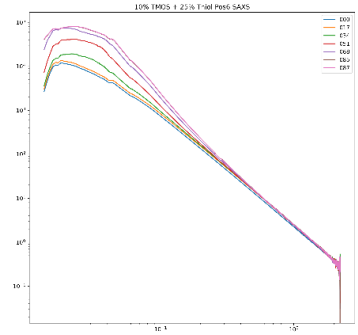

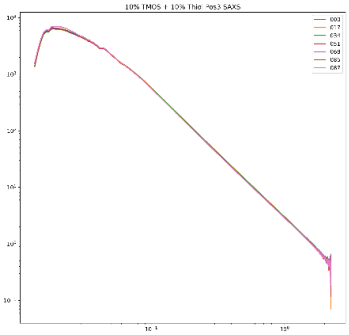

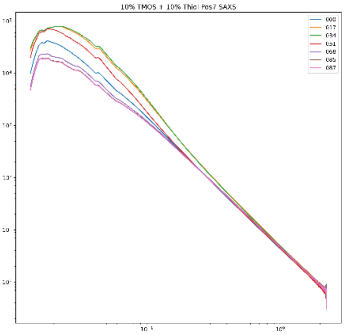

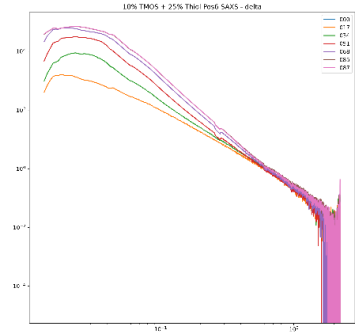

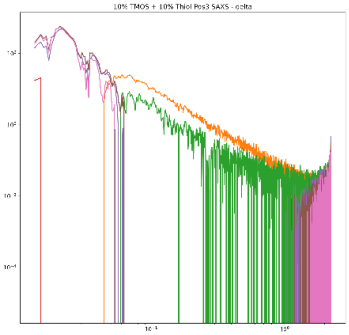

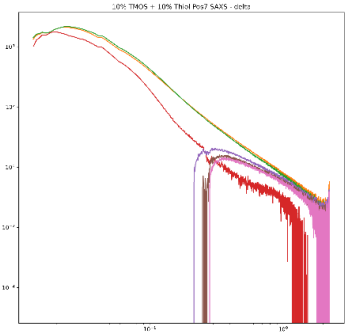

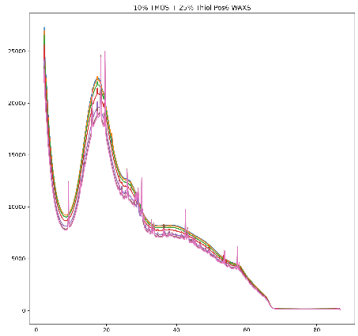

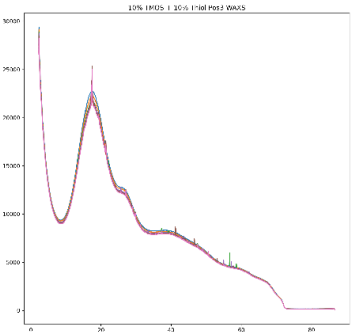

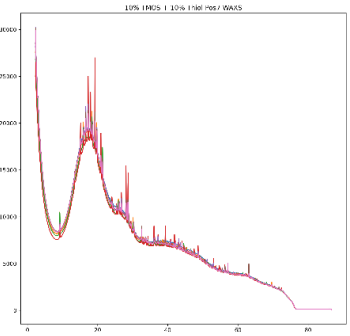

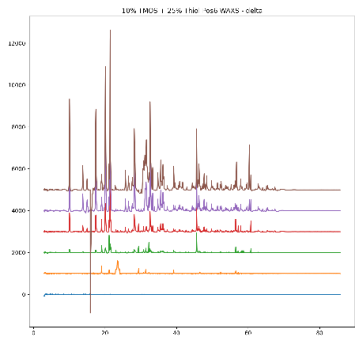

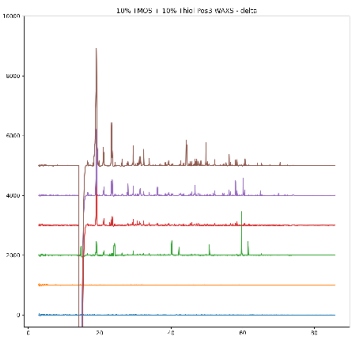

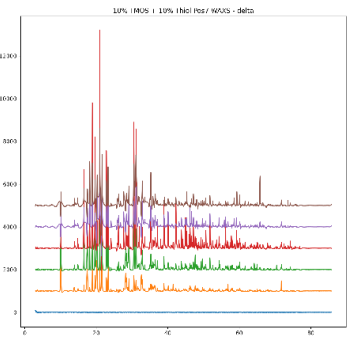

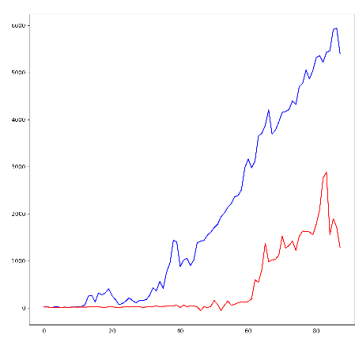

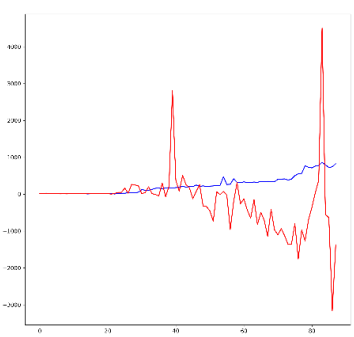

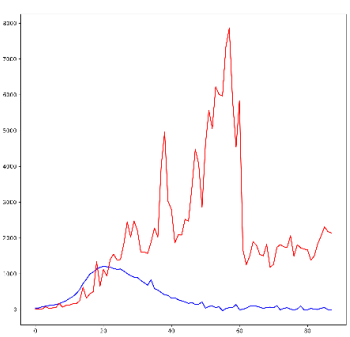

500mM solutions

100mM solutions

100mM solutions

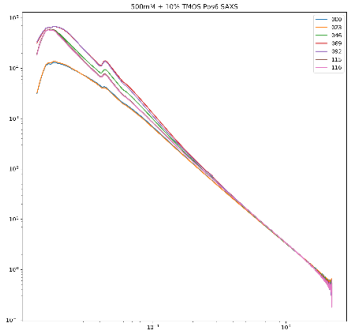

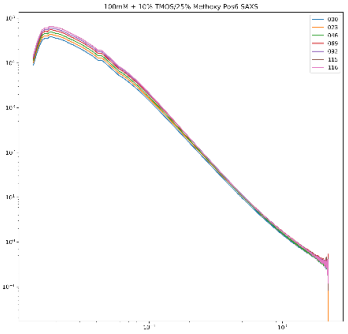

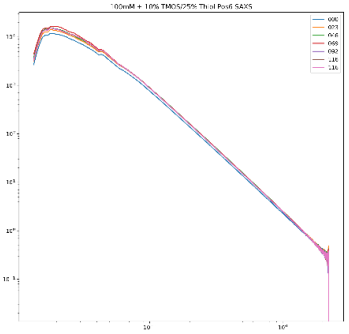

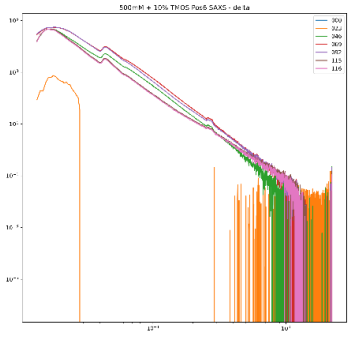

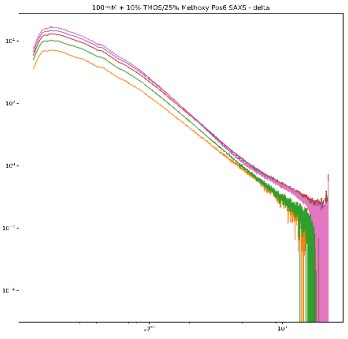

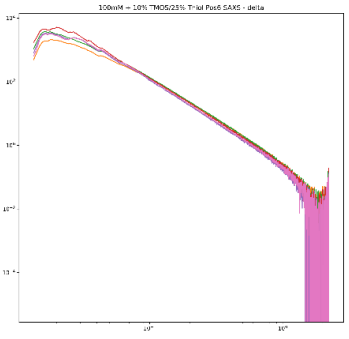

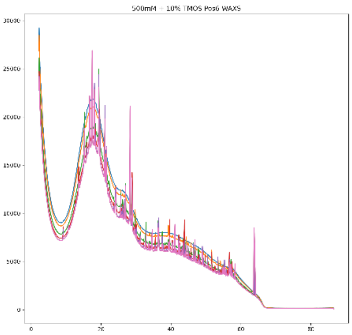

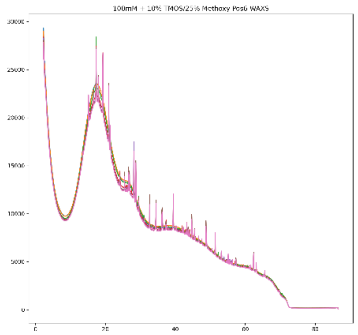

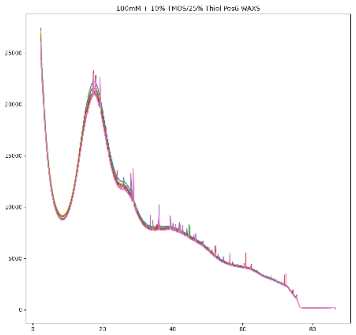

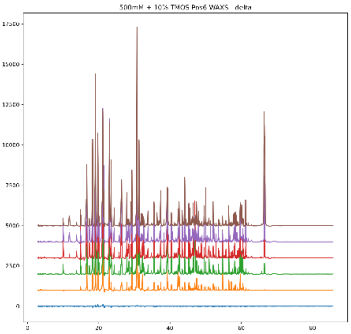

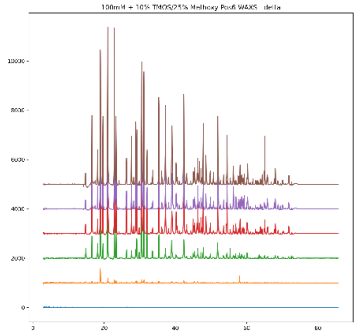

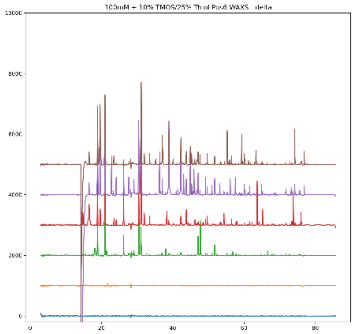

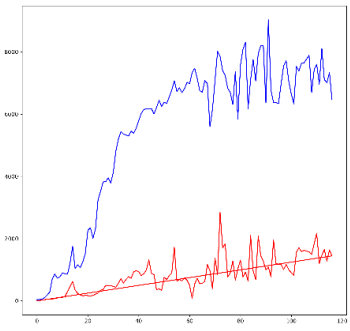

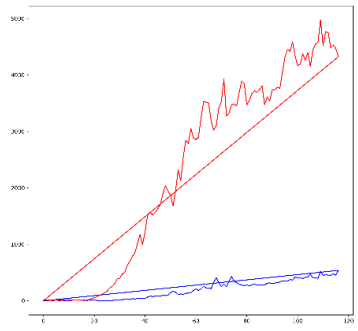

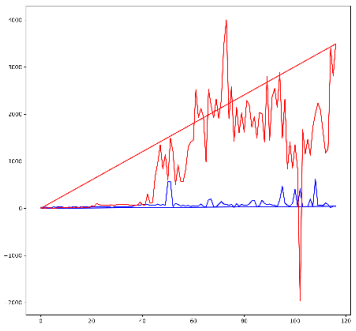

Supplement C: ESRF SAXS/WAXS Data

Presented here is a summary of the SAXS and WAXS data taken from the experiments at ESRF BM02 with minimal post-processing. The capillaries used in these experiments were Kapton with a 1.2 mm inner diameter. Each page represents six experiments run simultaneously, and each column on the page is the data from a single capillary. Each page is entitled with the experiment number (missing numbers represent experiments with data that was unusable) and the concentration of salts used for that set of reactions, and the columns are headed with the description of the gel in that capillary.

In each column are the results from a single capillary. Row 1 is the scattering invariant as calculated by Equation 7 from the methods section of this chapter for each of the 5 measured locations in the gel. The position with the biggest change in the invariant (most total scattering from precipitates) was chosen for further analysis (where a position number is written below the figure, the invariant was not enough to choose the most active position, and it was chosen manually by looking at the SAXS and WAXS scattering patterns at each position). Row 2 is the SAXS pattern of the precipitates, measured as the difference in scattering from t=0 at each time point. Row 4 shows the background subtracted WAXS patterns, and row 5 the peak height tracking for celestine (blue) and hemihydrate (red), this time again from all five measured locations in the gel. Table S2 visually summarizes the above description of the data layout.

Table S2: *visual description of data layout for ESRF SAXS/WAXS data*

Experiment number and starting concentration					
Gel 1 parameters	Gel 2 parameters	Gel 3 parameters	Gel 4 parameters	Gel 5 parameters	Gel 6 parameters
All positions Porod invariant	All positions Porod invariant	All positions Porod invariant	All positions Porod invariant	All positions Porod invariant	All positions Porod invariant
SAXS from precipitation reaction	SAXS from precipitation reaction	SAXS from precipitation reaction	SAXS from precipitation reaction	SAXS from precipitation reaction	SAXS from precipitation reaction
Background subtracted WAXS	Background subtracted WAXS	Background subtracted WAXS	Background subtracted WAXS	Background subtracted WAXS	Background subtracted WAXS
Unique peak height sum for Celestine and Hemihydrate	Unique peak height sum for Celestine and Hemihydrate	Unique peak height sum for Celestine and Hemihydrate	Unique peak height sum for Celestine and Hemihydrate	Unique peak height sum for Celestine and Hemihydrate	Unique peak height sum for Celestine and Hemihydrate

Expt1 (500mM diffusion)

25% TMOS	20% TMOS	15% TMOS	10% TMOS	10% TMOS + 25% Methoxy	10% TMOS + 25% Thiol
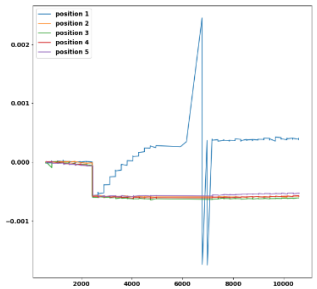	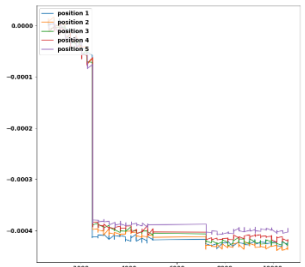	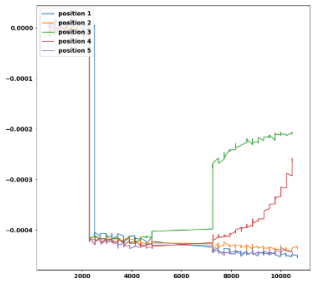	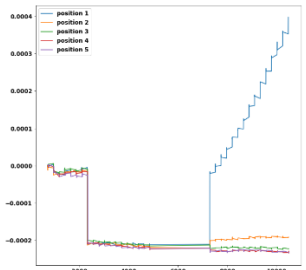	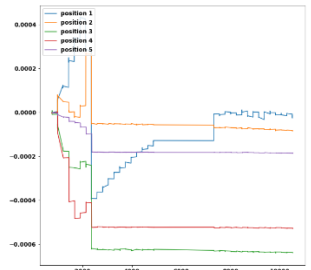	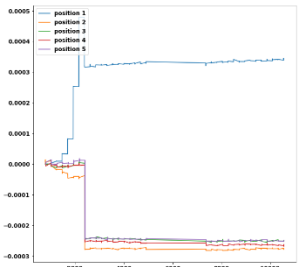
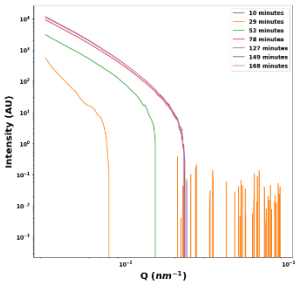	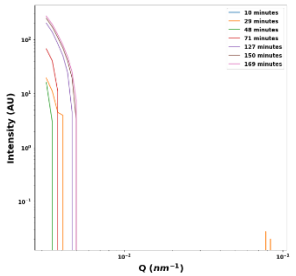	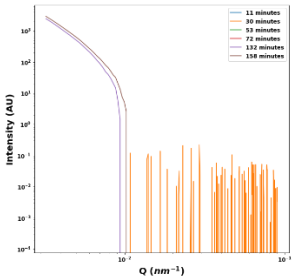	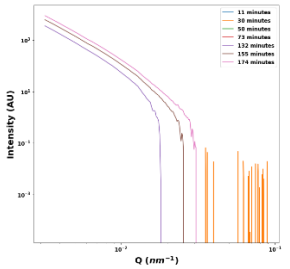	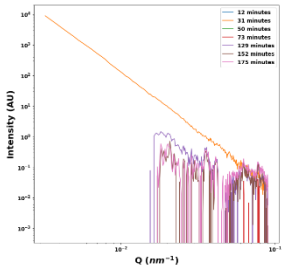	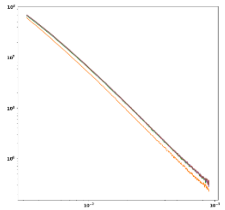
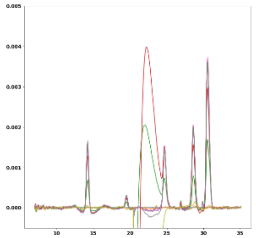	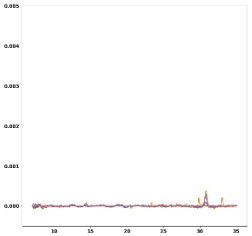	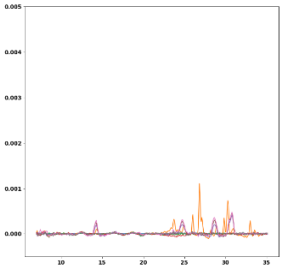	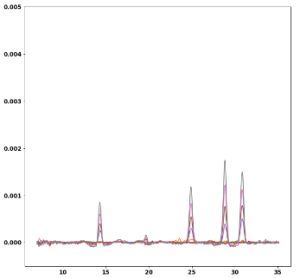	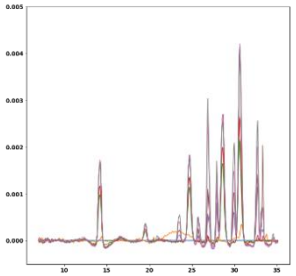	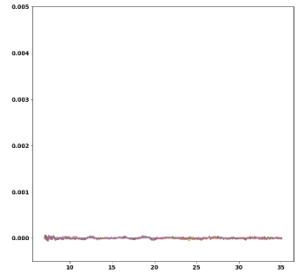
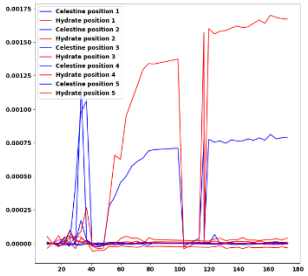	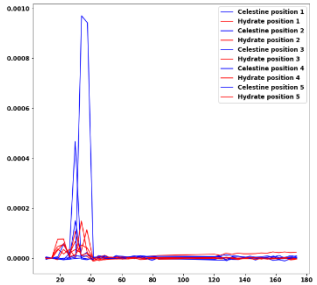	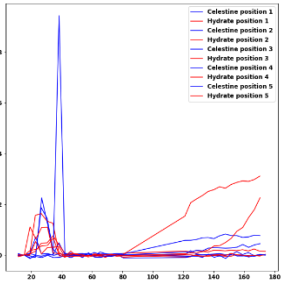	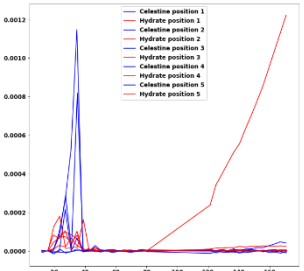	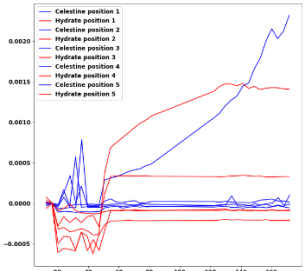	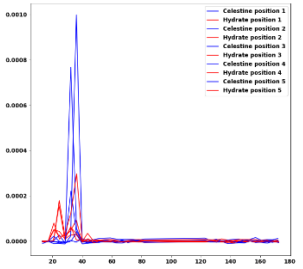

Processing error, # of datapoints

Pos1

expt2 (100mM Diffusion)

25% TMOS	20% TMOS	15% TMOS	10%TMOS	10% TMOS+25% Methoxy	10%TMOS + 25% Thiol
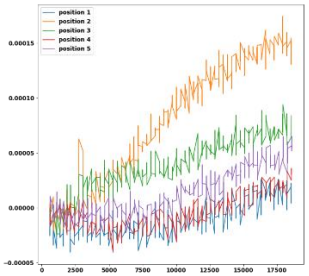	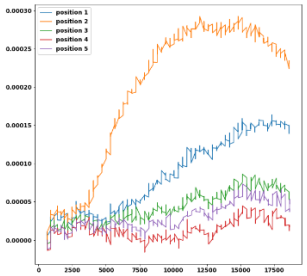	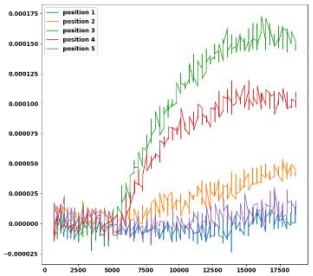	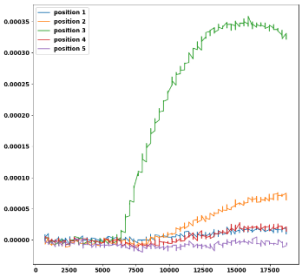	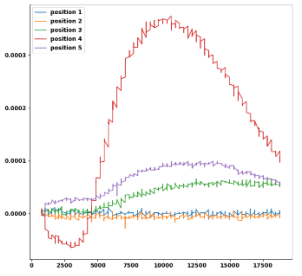	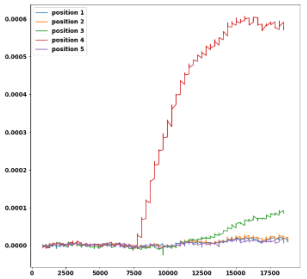
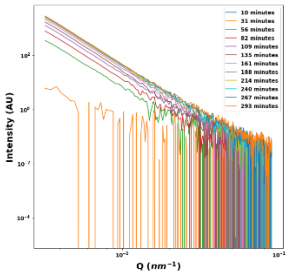	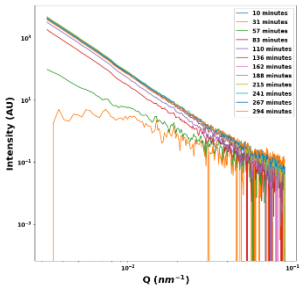	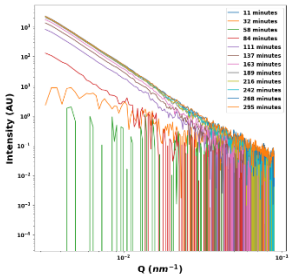	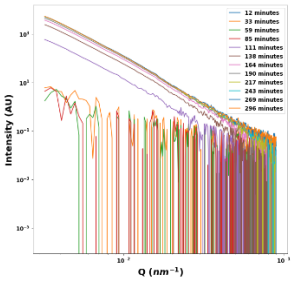	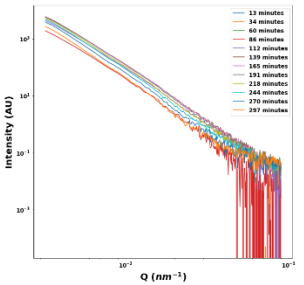	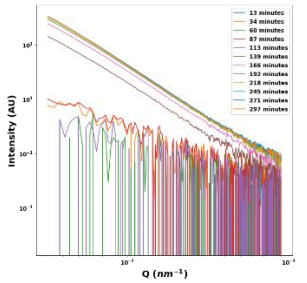
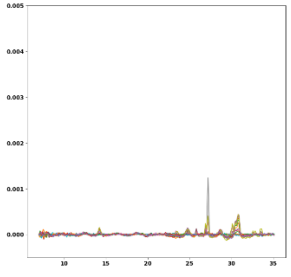	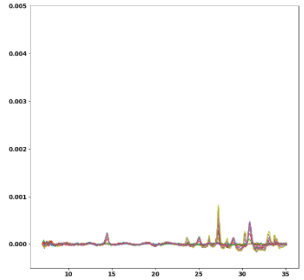	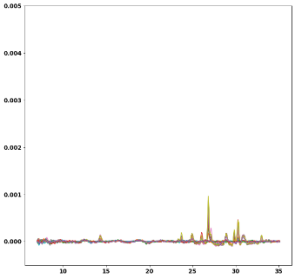	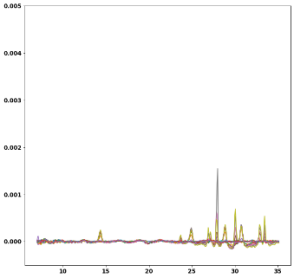	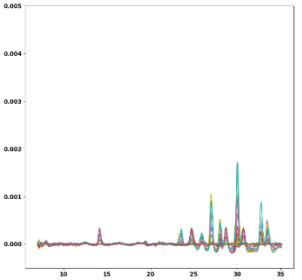	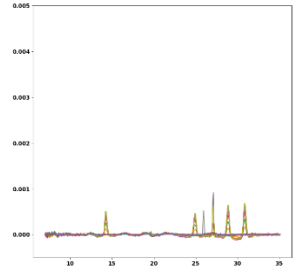
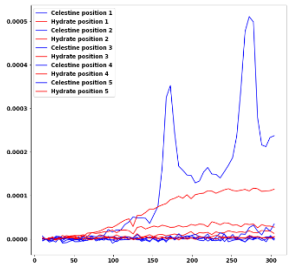	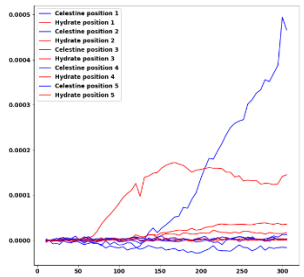	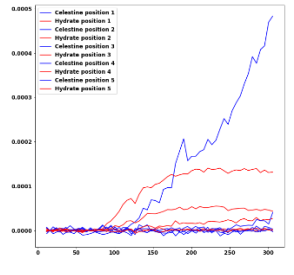	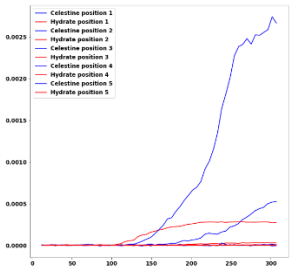	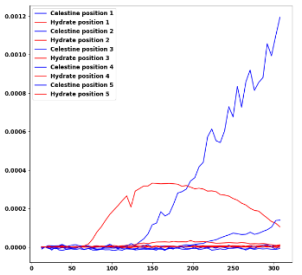	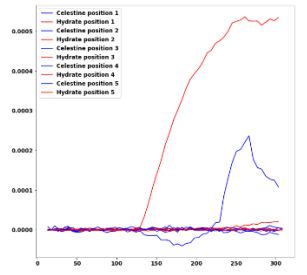

Expt3 (50mM Diffusion)

25% TMOS	20% TMOS	15% TMOS	10%TMOS	10% TMOS+25% Methoxy	10%TMOS + 25% Thiol
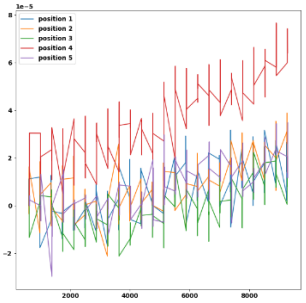	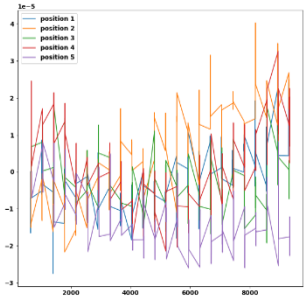	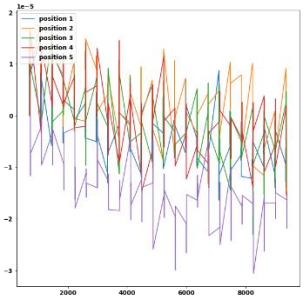	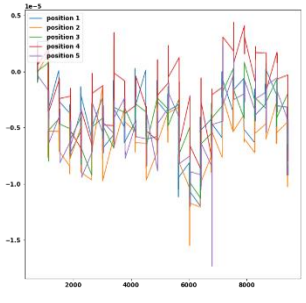	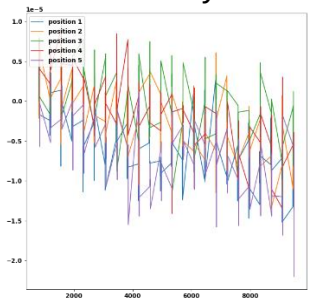	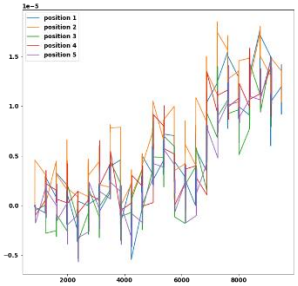
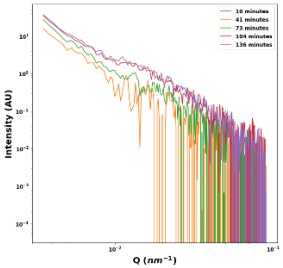	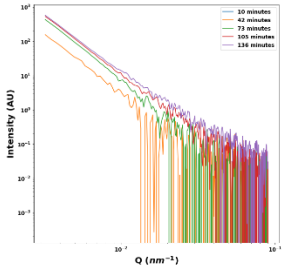	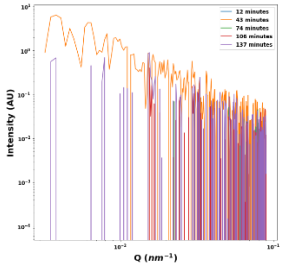	n/a	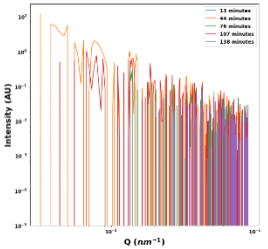	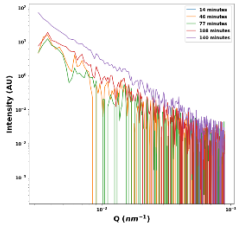
Pos5	Pos2	Pos4		Pos2	Pos5 minimal diff between positions
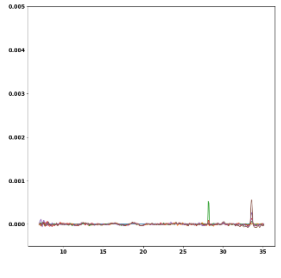	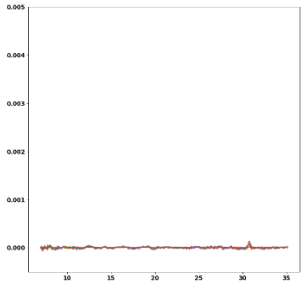	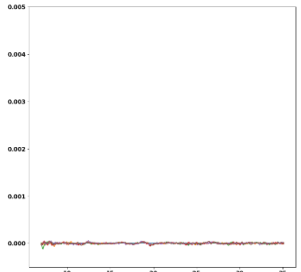	n/a	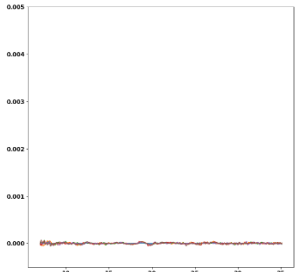	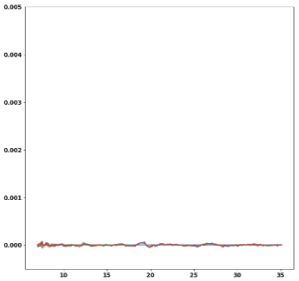
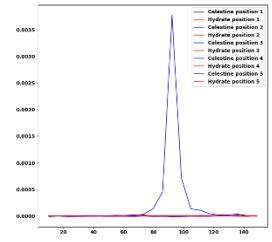	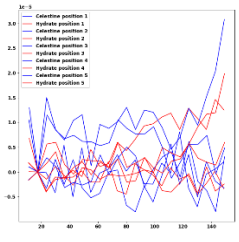	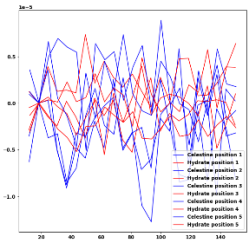	n/a	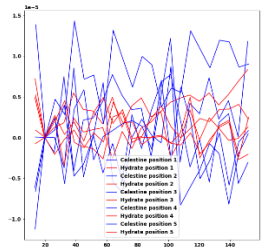	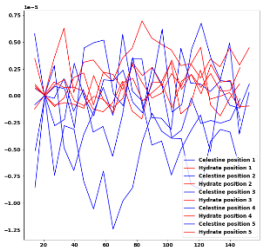

Expt5 (100mM Diffusion)

25% TMOS	20% TMOS	15% TMOS	10%TMOS	10% TMOS+25% Methoxy	10%TMOS + 25% Thiol
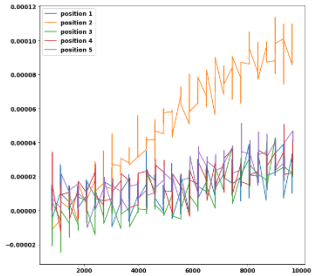	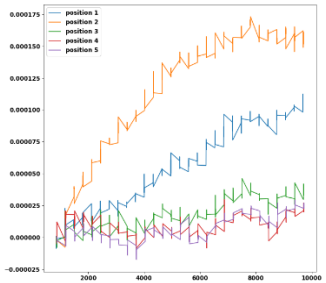	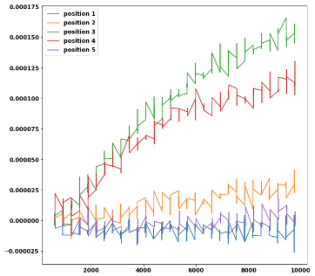	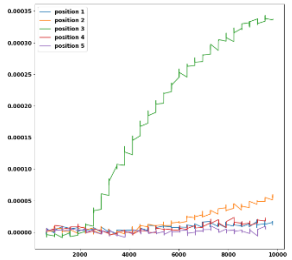	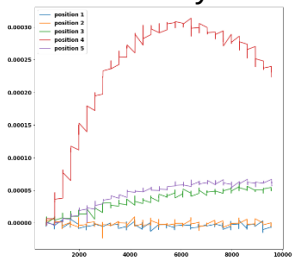	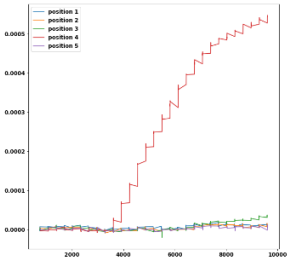
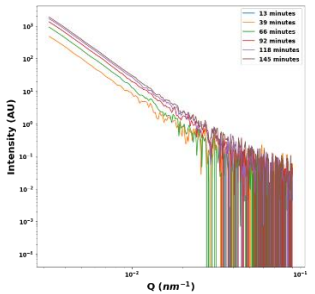	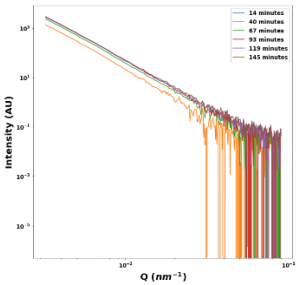	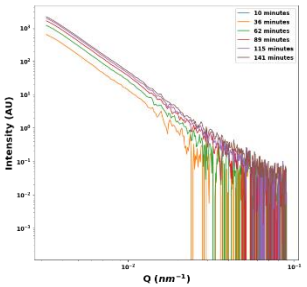	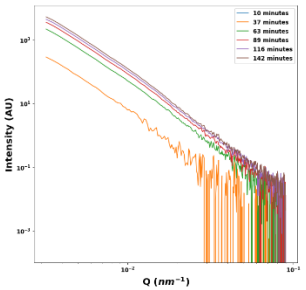	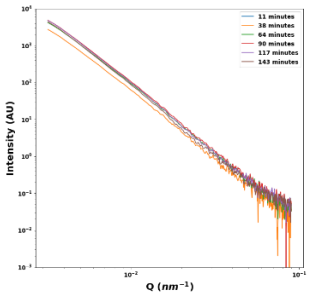	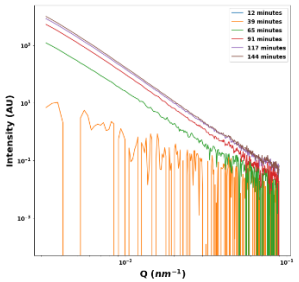
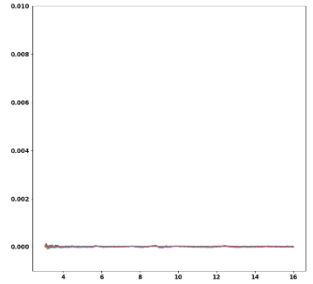	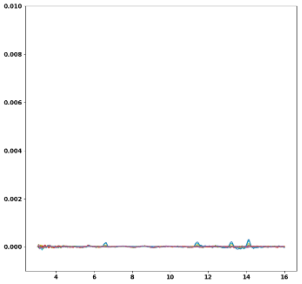	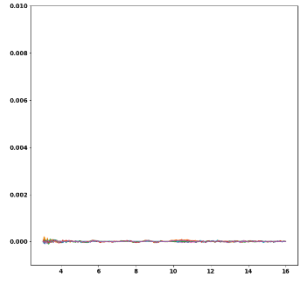	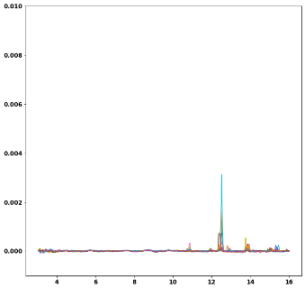	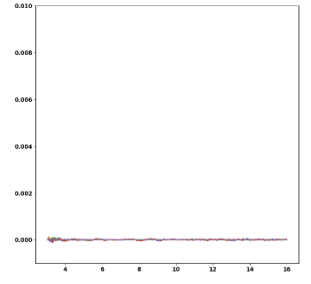	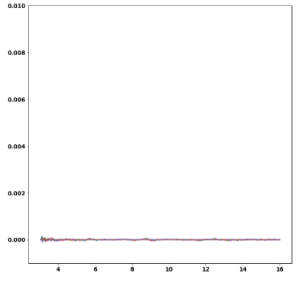
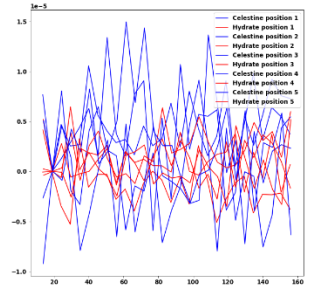	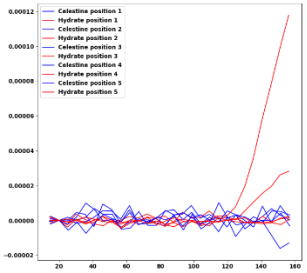	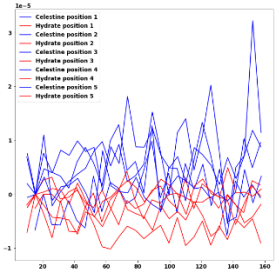	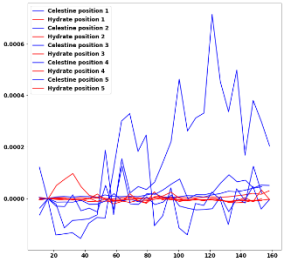	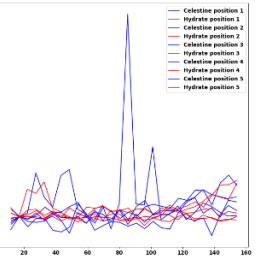	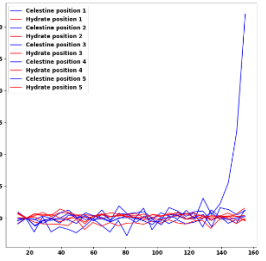

Expt6 (50mM Diffusion)

20% TMOS	15% TMOS	10%TMOS	5%TMOS	10% TMOS+25% Methoxy	10%TMOS + 25% Thiol

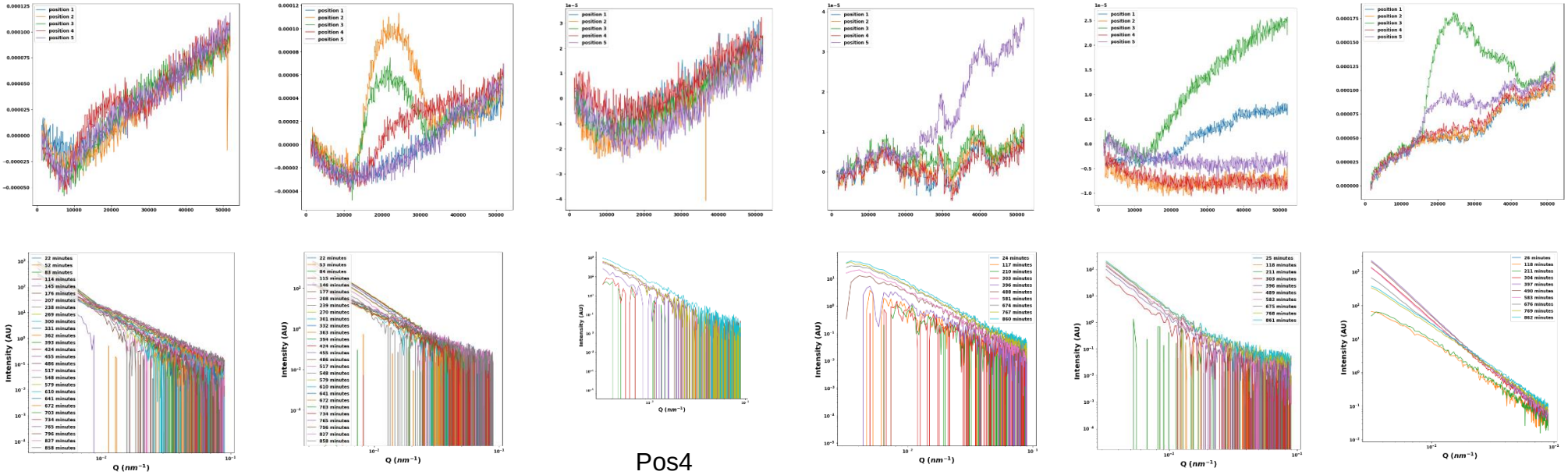

Pos4

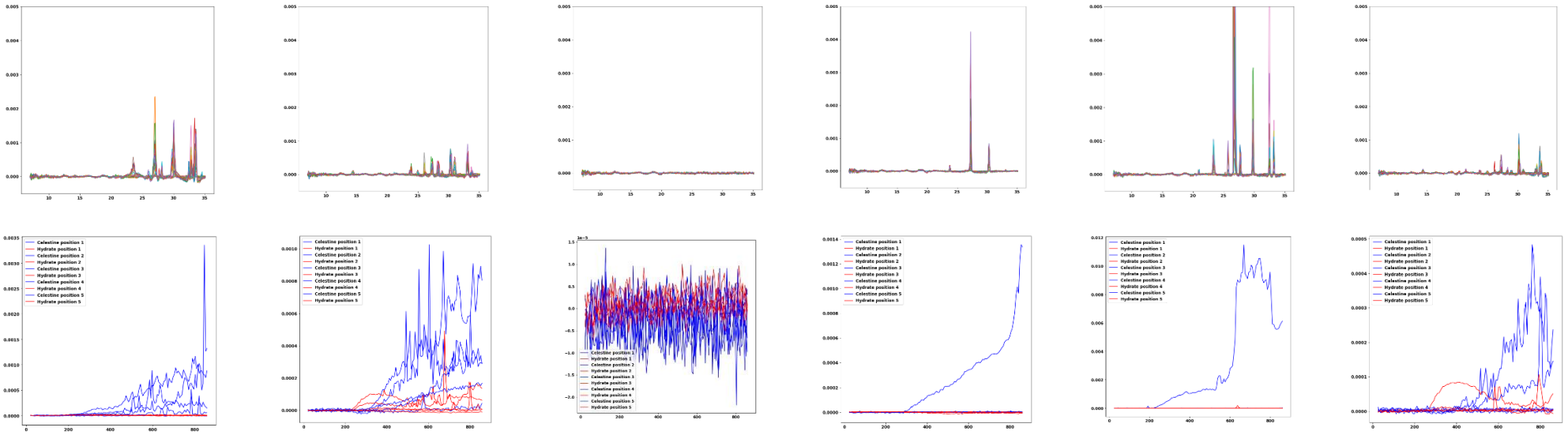

Expt8 (200mM diffusions)

20% TMOS	15% TMOS	10% TMOS	5%TMOS	10% + Methoxy	10% + Thiol
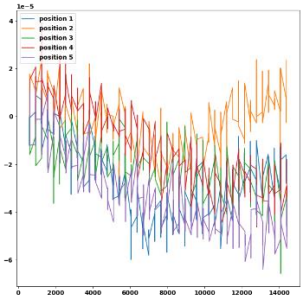	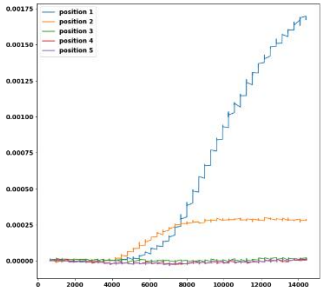	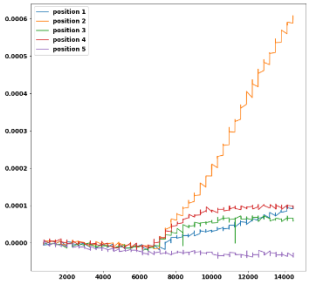	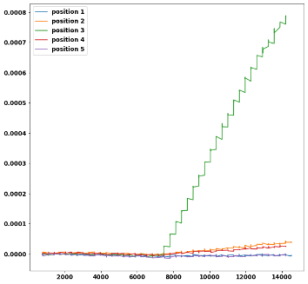	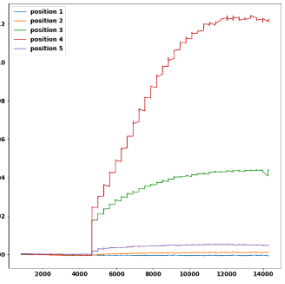	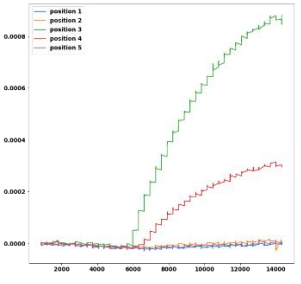
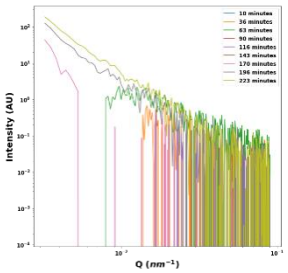	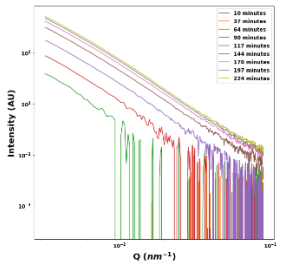	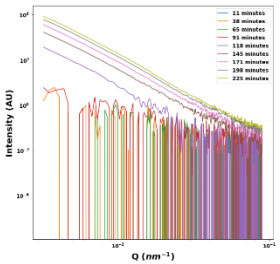	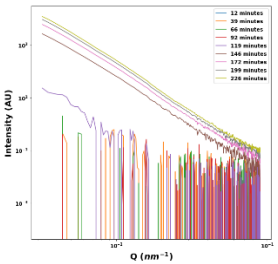	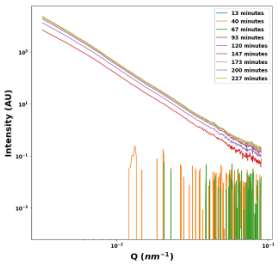	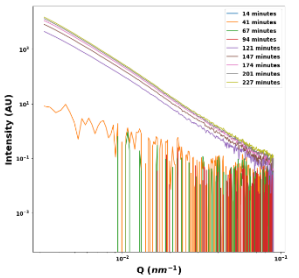
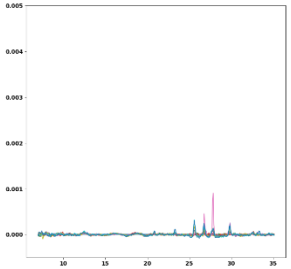	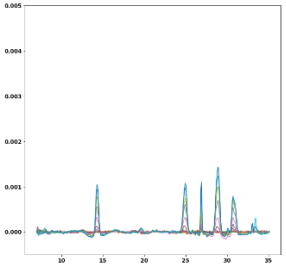	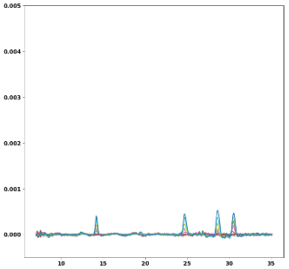	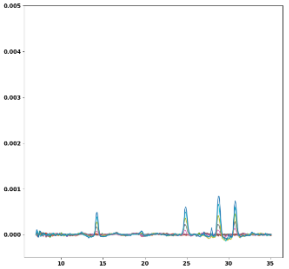	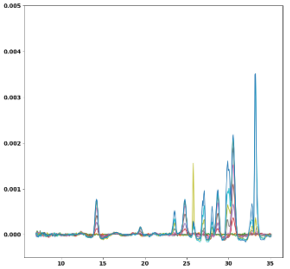	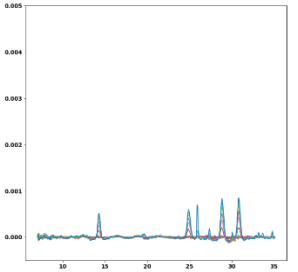
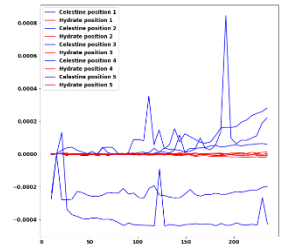	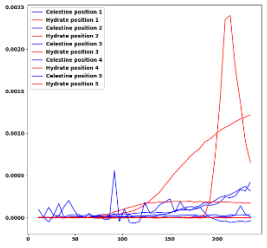	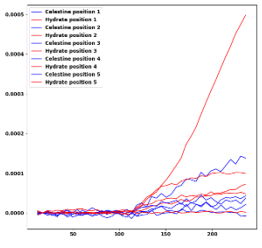	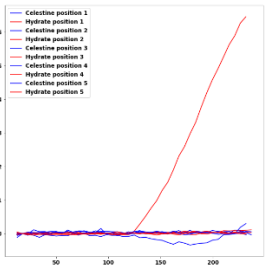	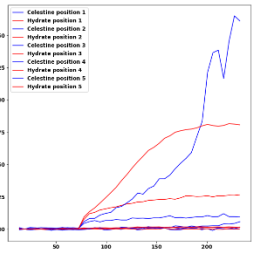	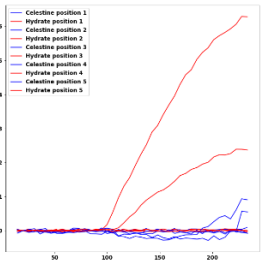

Expt9 (100mM Diffusion)

20% TMOS	15% TMOS	10% TMOS	5%TMOS	10% + Methoxy	10% + Thiol
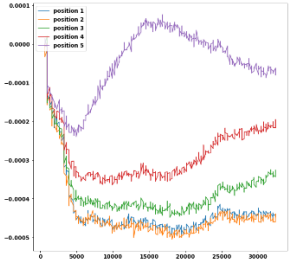	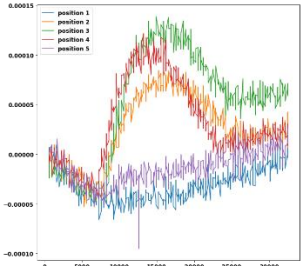	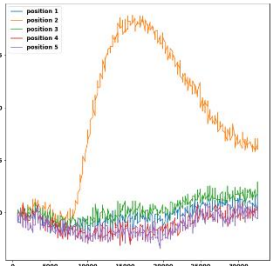		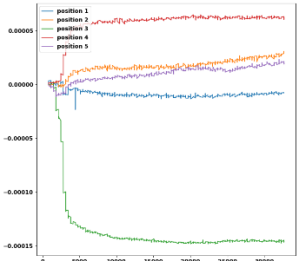	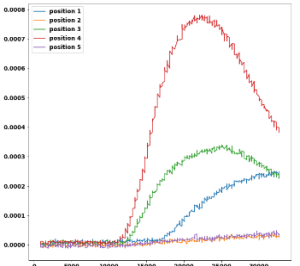
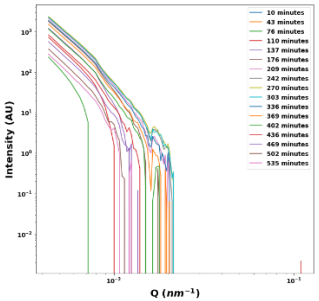	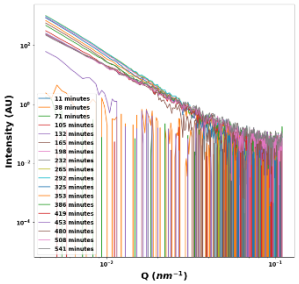	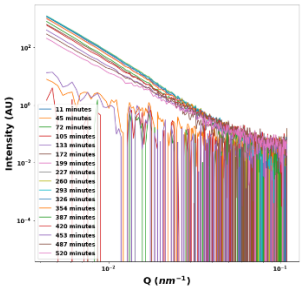	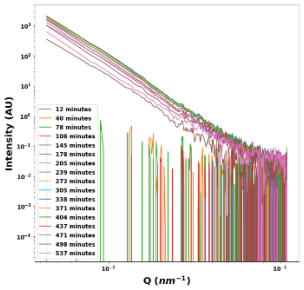	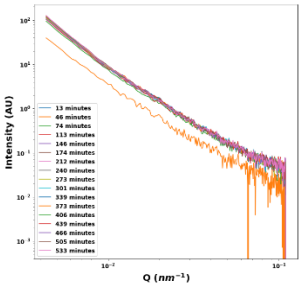	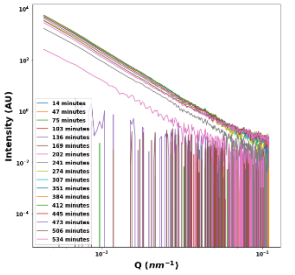
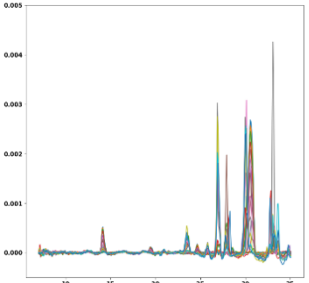	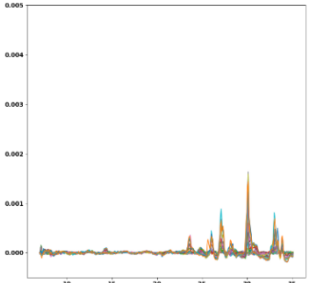	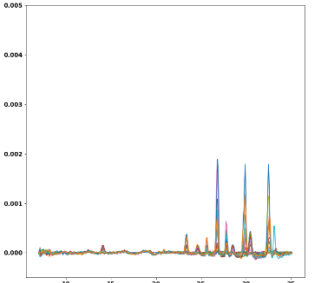	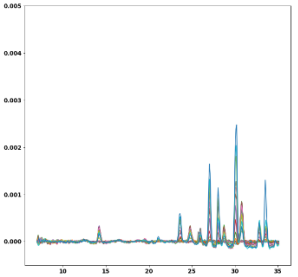	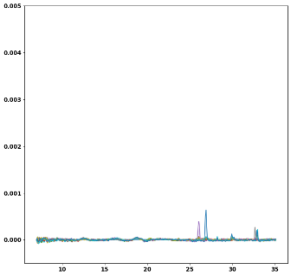	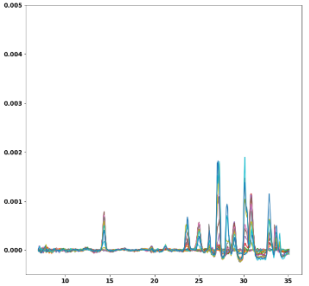
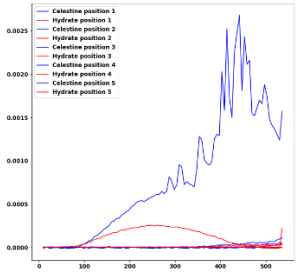	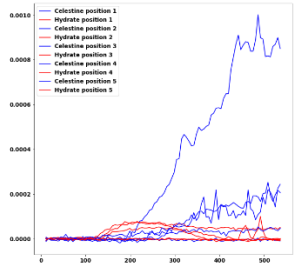	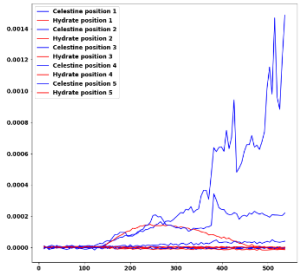	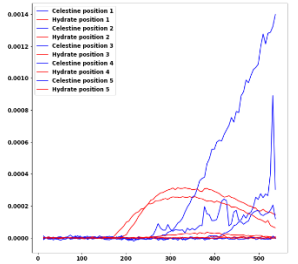	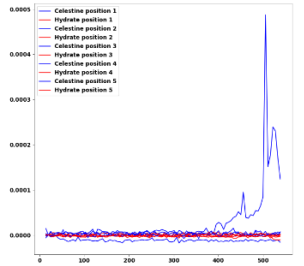	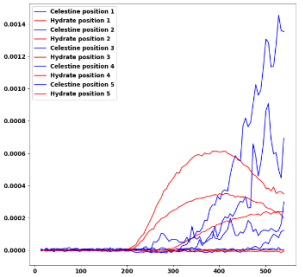

Expt11 (200mM Diffusion)

20% TMOS	15% TMOS	10% TMOS	5%TMOS	10% + Methoxy	10% + Thiol
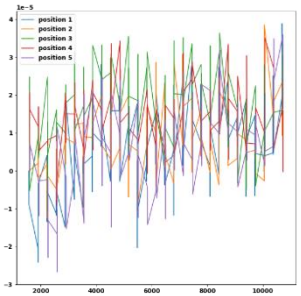	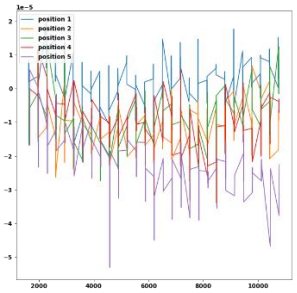	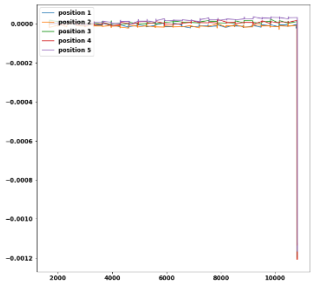	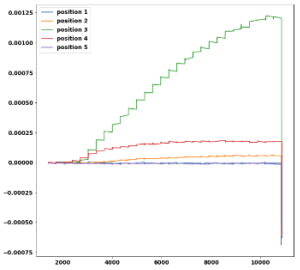	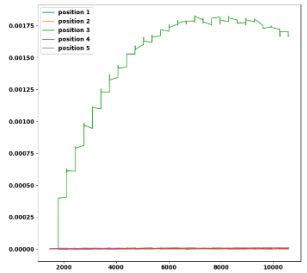	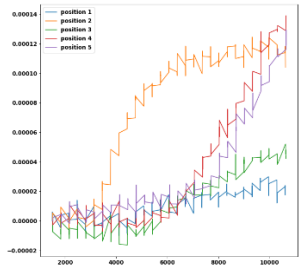
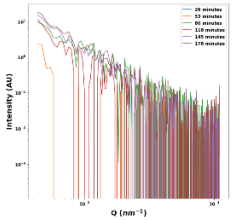	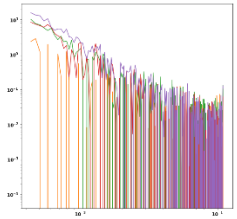	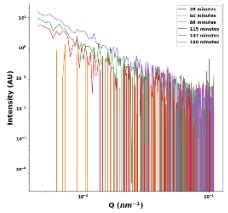	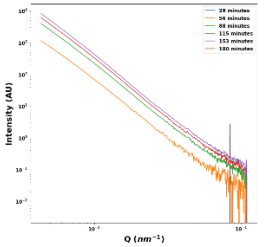	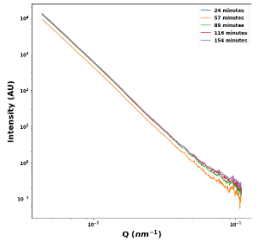	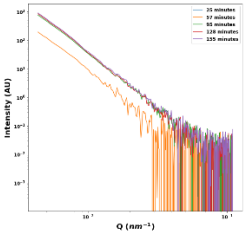
Pos3	Pos3	Pos5			
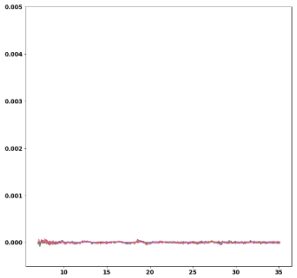	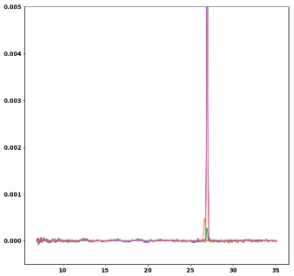	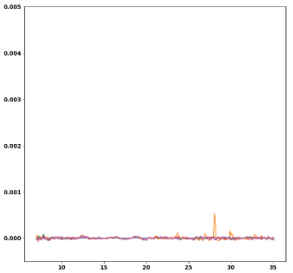	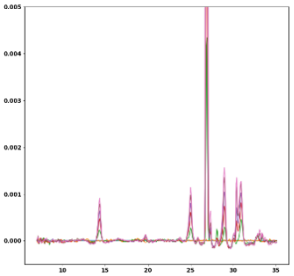	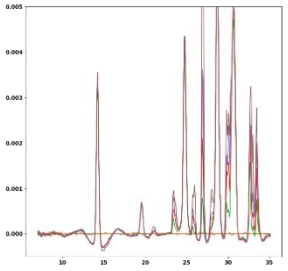	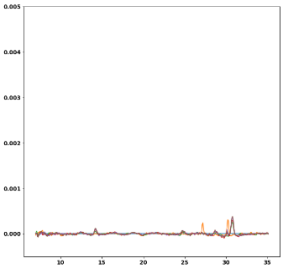
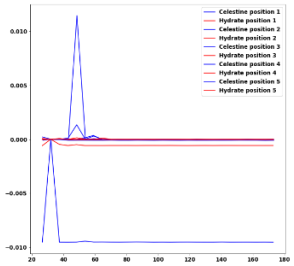	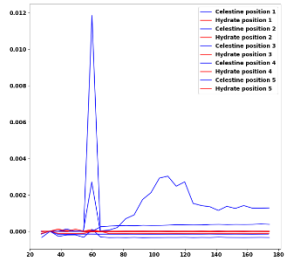	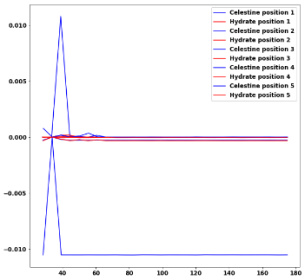	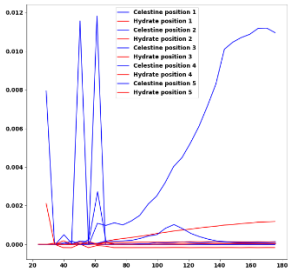	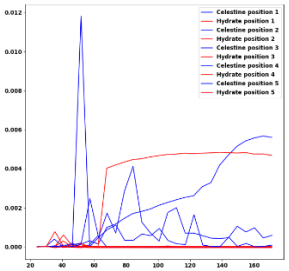	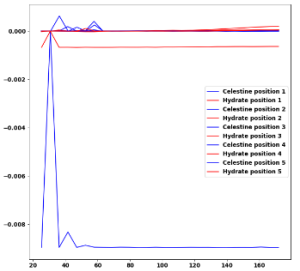

General Summary

In this work, a comprehensive examination of the nucleation of strontium sulfate minerals has been undertaken. Under the framework of both classical nucleation theory (CNT) and contemporary (non-classical) alternatives, a series of experiments under a variety of conditions observe the precipitation of Sr^{2+} and SO_4^{2-} ions from water. These experiments, performed in both bulk and confined conditions, revealed evidence of both classical and multi-step nucleation. Rather than being a contradiction, these results describe a complex landscape of possible nucleation pathways and intermediates.

First, cotitrations of $SrCl_2$ and Na_2SO_4 show a rate dependency on the mechanisms of nucleation. In slow titrations, observations of the turbidity, conductivity, and free-ion concentration reveal that the first species consumed by the nucleation reaction are neutral (i.e. ion pairs or larger), akin to descriptions of multi-step nucleation proposed in non-classical theories. However, at higher rates, the first stages of nucleation are characterized by the consumption of ions as predicted by classical theory.

A model mesoscopic nucleation theory (MeNT) is developed to describe how both nucleation pathways can coexist for a single system. A simple, single-parameter model describing nucleation as a function of the density of Sr^{2+} and SO_4^{2-} in space, considering both thermodynamic and kinetic contributions. It predicts a nucleation pathway resulting from the local increases in ionic concentration, rather than solely relying on collisions, as predicted by CNT. The model demonstrates that local thermodynamic minima are not a prerequisite for observing nucleation precursors. Moreover, it shows that nucleation precursors can be observed if part of the transformation pathway is traversed sufficiently slowly. Thus, a single nucleation pathway can comprehensively describe both the low-titration-rate observations of nucleation intermediates participating in the reaction and the high-titration-rate absence of such species.

Faster nucleation reactions, driven by higher supersaturations, were also shown to influence phase selection during the nucleation reaction. When the concentration at the time of nucleation exceeds ~10 mM, a transient hydrated mineral phase is formed. This threshold is coupled to the critical supersaturations at which the transition from consumption of neutral species to consumption of ions occurred in the cotitration

experiments. This highlights a clear relationship between the nucleation pathway and the resulting mineral phase's nature. Specifically, when the reaction proceeds slowly, showing evidence of precursors (i.e. neutral species), celestine forms. In contrast, when the reaction occurs quickly with the consumption of ions, a transient intermediate hydrate phase is formed.

This hydrated phase is characterized as $SrSO_4*1/2H_2O$ and shown to be an independent species, not a nucleation precursor to celestine. Through a series of *in situ* IR, Raman, and x-ray diffraction experiments, it is shown that the hydrate transforms into celestine via a dissolution-reprecipitation reaction following Ostwald's rule of stages wherein the most soluble phase forms first. This shows that the "rule" is more of a description of a pattern as the hydrated intermediate is not a necessary step in the formation of celestine despite the fact that the system follows Ostwald's rule under the conditions in which it appears.

These reaction pathways are summarized in the figure on the following page. The multi-step nucleation of celestine via neutral species as well as the classical direct nucleation of hemihydrate are depicted with solid arrows representing the reaction steps. MeNT proposes a continuum of states that are represented by a dashed line for the nucleation of celestine. However the exact nature of the relationship between the neutral species observed from the two-step nucleation and the ion-dense clusters propose by MeNT remains an open question, as does the spectra of possibilities for the dissolution-reprecipitation transformation from hemihydrate to celestine – this is represented by a red dotted arrow.

Finally, the effects of confinement on the reaction were tested through a series of counter-diffusion experiments in porous silica gel, observed by the scattering and absorption of x-rays. These observations show the formation of both celestine and the transient hydrate phase in the pores. *In situ* observations provided additional evidence for the differing nucleation pathways of both mineral phases.

Other effects of confinement, such as kinetic modulation driven by surface functionality, were explored during the counter-diffusion experiments. Notably, it was found that in this system, the induction time for nucleation counterintuitively decreased

with lower average pore sizes. However, limitations to the data constrain the conclusions that can be drawn about this or other observed effects. Still, the potential for the experimental system as an effective platform for further studies of the effects of confinement and nucleation as a whole is demonstrated.

Overall, this dissertation provides a comprehensive view and understanding of the nucleation of strontium sulfate – both celestine and its metastable hydrated form – in bulk and confined environments. The experiments offer a roadmap that can be followed for studying other nucleation systems and serve as the launching point for more detailed studies of confinement effects.

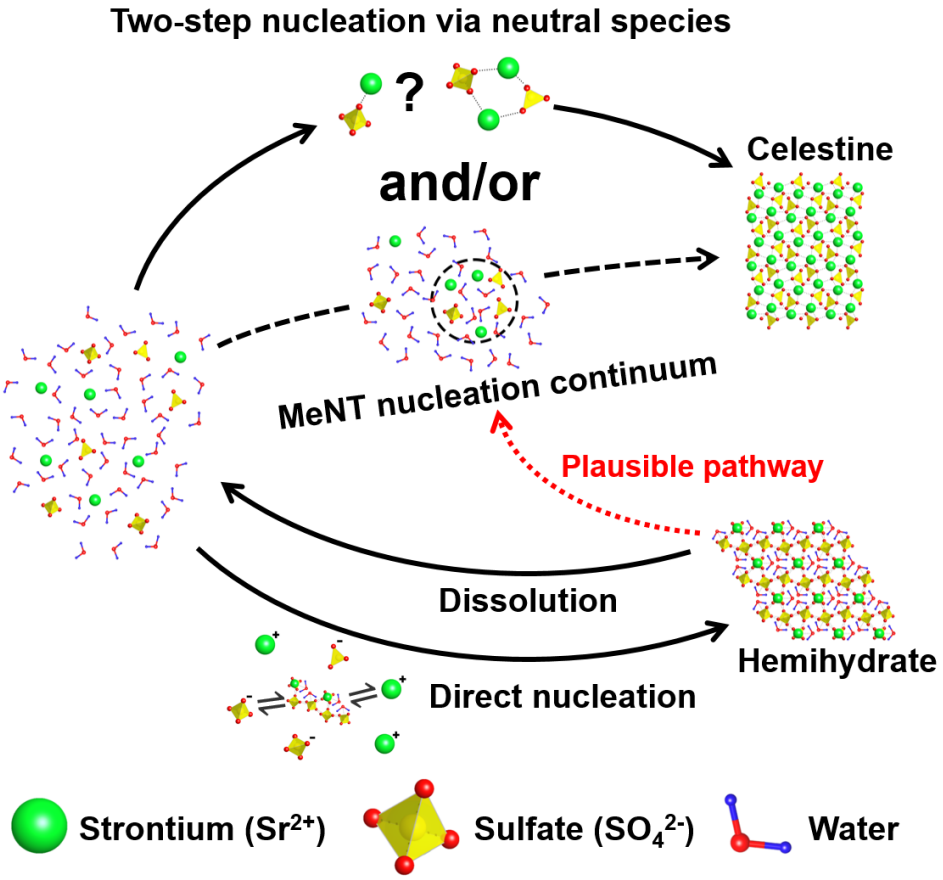

Figure[1–4]*: reaction pathways in the Sr-SO4-H2O system as described in this work. Classical nucleation of a metastable hemihydrate phase and its subsequent dissolution and a separate non-classical nucleation of the anhydrous celestine mineral. A multi-step nucleation pathway that necessitates the consumption of neutral species – i.e. ion-pairs or larger – was found for the precipitation of celestine. The presence of these multiple pathways is well described by a mesoscopic nucleation theory that predicts pre-nucleation clusters characterized by regions of high ion density in solution. Finally, a plausible transformation pathway that could be described by CIDR (coupled interfacial dissolution-reprecipitation) or direct dissolution into clusters, as reported for hematite by Zhu* et al.[5]*, is depicted with a red dotted line.*

Figure notes:

Structures constructed using the VESTA visualization software[1] using data structural data from this work in conjunction with those from sources 2-4, and a proposed transformation mechanism from source 5:

1 K. Momma and F. Izumi, *J. Appl. Crystallogr.*, 2011, **44**, 1272–1276.

2 B. R. W J ames and W. A. W ood, *Proc. R. Soc. London. Ser. A, Contain. Pap. a Math. Phys. Character*, 1925, **109**, 598–620.

3 W. Abriel and R. Nesper, *Zeitschrift fur Krist.*, 1995, **205**, 99–113.

4 S. Takahashi, M. Seki and K. Setoyama, *Bull. Chem. Soc. Jpn.*, 1993, **66**, 2219–2224.

5 G. Zhu, B. A. Legg, M. Sassi, X. Liang, M. Zong, K. M. Rosso and J. J. De Yoreo, *Nat. Commun.*, 2023, **14**, 1–11.

Prospectus and closing thoughts

Expanding the possibilities of co-titrations:

Classical nucleation theory (CNT) was first developed and formulated in the 1930s through expansions of the ideas of Gibbs[1] in the works of chemists like Becker and Doring[2], as well as Volmer and Weber[3]. This theory of a single energy barrier, traversed via random thermal fluctuations in a chaotic system dominated the field for nearly a century, and only in the past 20 years have alternative theories come to light. Recent research proposes alternative mathematical formulations for predicting nucleation like MeNT (discussed in Chapter 1), as well as direct evidence of nucleation intermediates that reveal a nucleation landscape more complex than that proposed by CNT.

The work presented in this thesis, particularly those of chapters 1 & 2, were in large part motivated by the first observations of pre-nucleation complexes – those reported in 2008 by Gebauer, Volkel and Colfen[4] – that were found using titrations of calcium ions into carbonate rich solutions. This use of a constantly evolving system opened new avenues of analysis that have since been exploited to discover new details about nucleation mechanisms, and identify systems where multi-step nucleation pathways play a key role.

Chapter 2 of this thesis serves as a prime example of this phenomenon. Cotitrations of Sr^{2+} and SO_4^{2-} ions into a reactor were meticulously tracked by optical and potentiometric probes – a procedure which revealed the likely presence of a neutral species that participates in the nucleation of celestine, but does not contribute to the activity of Sr^{2+} or to the overall conductivity of the solution. However, despite these findings, no characterization of these elusive species was achieved in this work. The experiments of chapter 3 had the potential to remedy that under the hypothesis that confinement can stabilize transient species, but the complexity of those experiments, was too large to resolve this specific issue. A more targeted experimental approach would likely be more effective in addressing this open question.

For instance, utilizing high-energy scattering from diluted solutions could offer insights into the nature of these transient species, as previously demonstrated in the case

of calcium sulfate. Particularly apparent, motivated by the idea that switching from steady-state systems to titrations allowed for the revelation of pre-nucleation clusters, would be the idea to explore a more diverse range of changing environments. The current body of literature predominantly focuses on two easily attainable dynamics in salt nucleation studies: 1) constant supersaturation and 2) monotonically increasing supersaturation. However, these conditions do not comprehensively represent the diversity found in nature. What would happen in the case of stepwise increasing saturations, dilutions, or decreasing supersaturations? How about oscillating supersaturations or other piecewise supersaturation profiles? Remarkably, all of these conditions can be relatively easily and inexpensively achieved using the equipment described in this work (particularly the Metrohm Titrando), and, to the best of my knowledge, have not been attempted. It is conceivable that by reaching conditions where nucleation intermediates are suggested to appear and subsequently modifying the reaction conditions, these intermediates could be more effectively studied. There is also the possibility of revealing them to be nothing more than measurement anomalies or probe errors. In either case, such outcomes would be valuable for the comprehensive evaluation of nucleation in these systems.

The expansion of the range of supersaturation profiles could also easily pair with an expansion of the library of ions tested. While reports have indicated the presence of nucleation precursors in both calcium[5] and barium sulfate[6], the experiments capturing these effects differ from each other and those in this work in terms of methodologies and conditions tested. It would be prudent to test a variety of cations, and possibly other anions like phosphates, under uniform conditions and protocols to obtain better insights into the effects that different ions have on nucleation processes and to be able to better generalize the results or even come up with predictive criteria for how unexplored systems might behave. As it stands, non-classical nucleation mechanisms are being reported system-by-system, and developing general ideas of what to look for and with which minerals would be a massive step forward.

Analytical and theoretical evaluations of induction time

The possible presence of transient neutral species was not the only insight into the nucleation of strontium sulfate revealed by the cotitrations. As presented in Chapter 1, a strong relationship between the titration rate (by extension, the supersaturation rate) and the induction time for nucleation was found. This result, on its own, is not surprising – achieving high supersaturations would logically lead to fast nucleation processes.

However, the exact nature of this relationship was not explored, despite being found to be nearly perfectly linear on a logarithmic scale. No effort was made to compare this result to what would be expected by CNT, MeNT, or any other mathematical formulation of nucleation kinetics. This is in part due to incomplete data – the conditions under which the induction times of $SrSO_4$ in steady-state solutions and the conditions of the titrations were different in volume, agitation rate, and background ionic environment. The interfacial energies extracted in the supporting information of chapter 2 could theoretically form the basis for such an analysis of CNT in the changing titration system, but still suffer from the differences in agitation rate and non-constant background ionic strength used in the cotitration experiments.

To my knowledge, limited information exists about what happens in a system before nucleation occurs (i.e. during the induction time before nucleation), unless a pre-nucleation cluster exists or significant restrictions, like making a 2D system[7], are enforced. CNT predicts a system that is in a state of random fluctuation, but aside from that, temporally uniform. MeNT describes a pathway between the aqueous and crystalline state with variable kinetics along the route. The statistical kinetic derivations of CNT rely on steady-state environments[8]. If the traditional equations were applied to a constantly changing system, like a titration experiment, the probabilistic nucleation time would need to be calculated differently as what was before an easily handled constant would become a time-dependent parameter. This is in addition to the fact that the classical prediction of induction time is already less precise than actual experimental results. It would be worthwhile to explore whether the predictive probabilistic formulae can be arranged to accurately describe the extremely predictable and repeatable results presented in chapter 1, or if there is a missing variable that requires implementation.

This investigation and the proposed experiments involving complex supersaturation variance during the induction period would be intended to probe the nature of the induction period itself. It is possible to view this period as random thermal fluctuations that lead to the formation and dissolution of clusters such that each non-critical cluster would be expected to return to the disordered state (in the case of minerals, dissolved state). However, it is also possible to view this period as a biased random walk along the nucleation pathway such that a cluster, once formed, may undergo a period of random growing and shrinking (biased towards shrinking until the critical cluster size has been reached) suggesting that a nucleus is most likely to be formed in a location where a cluster has previously been and that the induction period at least partly consists of the time necessary for a cluster to grow to critical size. Effectively, experiments could be conducted to see if supersaturated solutions have a "memory" of their previous states as they become more concentrated or diluted to discern if there are hidden processes occurring during the induction time.

The discussion from chapter three scratches the surface of this question where it was observed that longer induction time reactions likely resulted in the "faster" hemihydrate forming in greater quantities. This raises interesting questions about rate-controlling parameters (confinement and other physico-chemical surroundings, but also possibly additives) being able to influence phase selection during the nucleation reaction via kinetic control alone in non-steady state systems, but also opens the door for confinement and additives to be alternative methods for probing this same question.

ETEM and other unfinished research topics

During the course of this project, an effort was made to explore the hemihydrate to celestine transformation using an Environmental Transmission Electron Microscope (ETEM). These experiments were meant to replicate the conditions under which the *in situ* XRD experiments in chapter 2 were conducted – a reasonably pure sample of hemihydrate was isolated, but this time placed on a TEM grid and exposed to water vapor under the confines of ETEM. The intent of the experiment was to explore how the limited amount of water collected from the vapor phase could be driving the transformation

reaction (i.e. was surface adsorption sufficient? Was water getting trapped between hydrate fibers?), however, during the course of the experiment, it was realized what we might actually have is nanometer-scale volumes of water full of ions dissolved from hemihydrate, with a celestine nucleation reaction that could be triggered on command by the electron beam. Obviously, any reaction carried out and behavior observed under these circumstances would have to consider the possible influence of the electron beam, but could still, in any case, be a useful proxy for direct observation of confined nucleation of celestine.

A couple other ideas that were discussed during the course of this project, and each definitely warrants further exploration, would be the comparison of the cotitration results from Chapters 1 and 2 with other systems, both other sulfates and mineral classes would go a long way towards generalizing (or not) the conclusions of those chapters. A deuterated synthesis of the hemihydrate is more limited in its scope – finding the precise quantity and location of the water molecules in the hemihydrate structure and allowing for a complete structural characterization.

Refining the confinement experiments

In addition to the improvements discussed in Chapter 3 possible for the confined nucleation experiments, it is worth noting how ambitious the experiment series was. While strontium sulfate ultimately proved to be an excellent candidate system for exploring the concepts of multi-step nucleation and Ostwald's rule of stages, it was severely hindered by limited available data. There is little-to-no literature available for strontium on adsorption or diffusion coefficients, and solubility data for hemihydrate is not available, to name some examples. Any proper analysis of the reaction kinetics, as well as fully-developed discussion of the surface effects would require these data as inputs.

The silica hydrogel also proved to have interesting unexplored parameters. As mentioned in chapter 3, characterizing the reaction completeness and residual alcohol would be useful examinations, and feasible with IR or Raman. Additional characterization of the completeness of the gelification reaction and the stability of the gels over time would be of use relatively simple and allow for better experimental control. Additionally, the

surface functionality in terms of functional group density and hydrophilicity could be examined, and the adhesion between the gel and capillaries could be measured and improved.

Finally, to achieve a more in-depth analysis of the nucleation process occurring in a gelled environment it is necessary to characterize the interaction between both Sr^{2+} and SO_4^{2-} with the hydrogel. Hydrogel filled capillaries could be suspended between reservoirs of salt solution and water similar to Fick's original diffusion experiments[9] to obtain experiment-specific diffusion rates. Attempts could be made to characterize the specific adsorption as well, as well as the polarity and hydrophilicity of the functionalized surfaces, although those efforts would be much more challenging. In fact, attempts were made to study these exact adsorption effects for this thesis, but were unfortunately derailed by the COVID-19 pandemic and the associated laboratory closures.

Intermediate experiments were also attempted to find heterogeneous nucleation parameters for $SrSO_4$ on surfaces of different functionalities. These were unfortunately also interrupted by the laboratory closures, but such intermediate experiments, either using functionalized particles to obtain kinetic information, or even functionalized surfaces with more direct structural probes (AFM, x-ray scattering) that nucleation could be observed on could provide valuable insights that shape the discussion of what happens in pores. However, based on the early attempts, it must be cautioned that there would likely be significant work needed to solve experimental issues needed to extract useful data from this type of experiment using strontium sulfate. Particularly, initial results indicated a very low adsorption of strontium that required tight experimental controls to measure adsorption above noise levels, and that there was little to no heterogeneous nucleation of $SrSO_4$ when in the presence of foreign particles with a variety of functionalizations. Additional tests and experiments would be needed even to find a protocol that allows for these evaluation. However, despite the difficulties, future comprehensive studies of confined nucleation would benefit massively from increased information about the surface interaction parameters of Sr^{2+}, SO_4^{2-}, or whatever other ions are being investigated.

The feasibility of a hydrogel-mediated cotitration as a method for studying confined nucleation has been demonstrated, but significantly more work is needed to transform this proof of concept into a diagnostic tool that allows for in-depth characterizations at every step of the precipitation process. The previously proposed titrations would be much simpler, but the depth of data that could be available from fully fleshed out gel diffusions could prove to reveal more details about the nature of nucleation reactions, especially for conditions closer to those found in real life environments.

Practical suggestions for future work

For any continuations regarding bulk kinetic studies (titrations or otherwise) it is recommended to use constant background ion concentrations at every stage of the experiment. This can easily be achieved for this system (and realistically any divalent salt where XCl_2 is mixed with Na_2Y to achieve a supersaturation of the salt XY) by always diluting reactant solutions into NaCl solutions of the same concentration as the solute solution. So in the titration experiments in chapters 1 and 2 where 100mM $SrCl_2$ and Na_2SO_4 were diluted into distilled water, a constant background could have been achieved by diluting into 100mM NaCl instead. This step would save the need for calibrating the ISE against background interference and will reduce the number of variables needed to consider for any analytic modeling.

It was mentioned in passing during the methods section of the chapter 3 that some point after the hydrogels finish reacting, they began to contract in size – sometimes resulting in debonding from the capillary wall, and sometimes in fractures forming inside the gel. These contractions reached extreme levels due to dehydration if gels were stored too long, or left out on the bench, but it was never examined if dehydration was the only cause of this contraction, or if strains could be generated by the increasing number of bonds formed during the gelificaiton reaction as well. Procedures like immersing the forming gels in water to prevent dehydration could be explored – this step could have the added benefit of allowing any residual alcohol to dissolve out of the gel as well. There are also examples in literature where the gels are stabilized in alcohol, or even dried under specific conditions to retain their structure. Any of these processing steps would require a moderate to significant amount of work to refine before the gel consistency could be

assured, but would the resultant certainty in the state of the gel during a counterdiffusion experiment would be very useful for a detailed analysis.

To facilitate the much larger amount of material that would be necessary to complete recipe refinements and other tests on the silica hydrogels, the less-toxic TEOS could be explored as a near 1-for-1 replacement of TMOS. The safety advantage is obvious, but the addition of 4 carbon atoms to precursor molecule would mean that more precursor would be needed to generate the same gels, and solubility limits would mean a higher lower bound on achievable minimum average pore size of this system. It may also be slightly more difficult to remove the ethanol byproduct as compared to methanol due to slower diffusion in water and slower evaporation rates. The safety advantage almost certainly compensates for these minor inconveniences however.

References

1 *Nature*, 1929, **124**, 119–120.

2 R. Becker and W. Döring, *Ann. Phys.*, 1935, **416**, 719–752.

3 M. Volmer and A. Weber, *Zeitschrift für Phys. Chemie*.

4 D. Gebauer, A. Völkel and H. Cölfen, *Science (80-.).*, , DOI:10.1126/science.1164271.

5 A. E. S. Van Driessche, T. M. Stawski and M. Kellermeier, *Chem. Geol.*, 2019, 530, 119274.

6 C. Ruiz-Agudo, J. T. Avaro, D. J. Schupp, D. McDonogh and D. Gebauer, *CrystEngComm*, 2020, **22**, 1310–1313.

7 M. Sleutel, J. Lutsko, A. E. S. Van Driessche, M. A. Durán-Olivencia and D. Maes, *Nat. Commun.*, 2014, **5**, 1–8.

8 M. A. Durán-Olivencia and F. Otálora, *J. Cryst. Growth*, 2013, **380**, 247–255.

9 A. Fick, *Ann. Phys.*, 1855, **170**, 59–86.